Experimental Study on Tollmien-Schlichting Waves over a Sharp-Edged Rectangular Bump

A study on harmonic content and wave growth

Aashish Mathew Eapen

Delft University of Technology

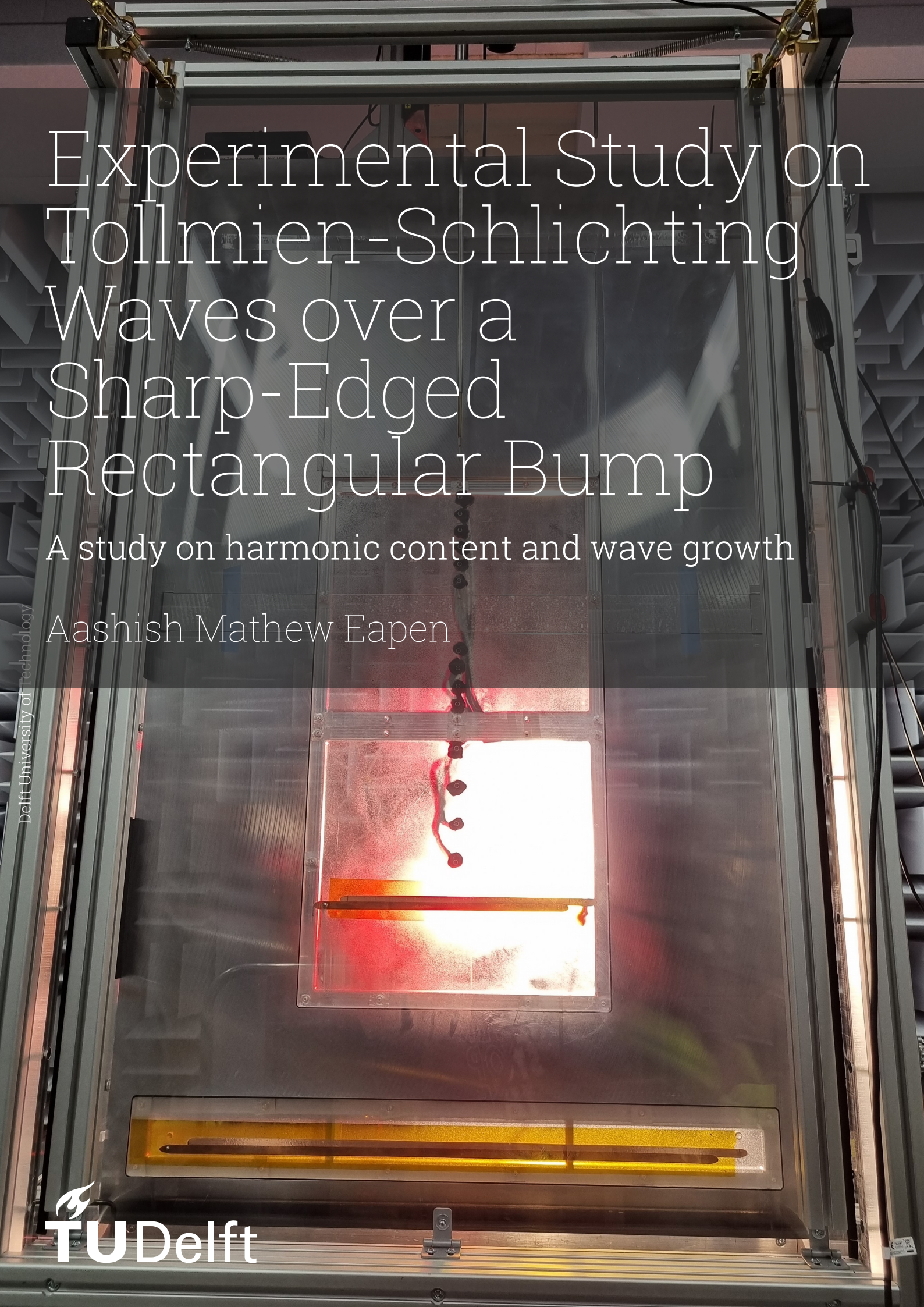

TU Delft

Experimental Study on Tollmien-Schlichting Waves over a Sharp-Edged Rectangular Bump

A study on harmonic content and wave growth

by

Aashish Mathew Eapen

to obtain the degree of Master of Science

at the Delft University of Technology,

to be defended publicly on Thursday, March 26, 2026, at 14:30.

Student number:	6020275	
Project duration:	March 1, 2025 - March 26, 2026	
Thesis committee:	Dr. Ir. WJ Baars,	Chairperson/ External Examiner
	Prof. M. Kotsonis,	Responsible Supervisor
	Dr. Ir. A. F. Ruis-Vidales,	Supervisor
Others:	Ir. M. Radaelli,	Daily Supervisor

TU Delft

Acknowledgments

The fruits: The challenge of this thesis has shown me how easy it is to be frozen in despair when looking ahead at the seemingly insurmountable mountain, while also proving to me what is possible through sustained effort when looking back from the mountain peak. I have learned that completing the journey is not merely a matter of planning with redundancies, but of continual micro-navigation and course correction. Insofar as the fruits of this thesis are the visible produce of a season growing, they exist only on the preconditions of adequate nourishment and support structures.

The leaves: The leaves of a tree help to capture light and atmospheric carbon (elements otherwise dispersed and intangible) and transform them into the nourishment required for the tree to bear fruit. My advisors served as these leaves; without their understanding guidance, I wouldn't have reached this end. I am indebted to Marios, for his rigorous scientific refinement; to Beto, always ready to address the granular technical details; and to Marco, for being my go-to-guy, helping me bridge course work and thesis work.

The branches: I want to thank Emiel for his guidance through the manufacturing process, and Stefan for his help resolving any issues that arose during the experimental campaign. While charting a new course mid-thesis, I leaned heavily on Marinha's advice and past work, which really helped me feel less lost. The mutual support that existed with Sergio really helped this campaign get off the ground. I don't want to fail to mention all the help/inputs from the research group around the lab: Jordi, Theo, Pierre, Babak, Srinivas, Abdoo, as well as all the other PhD candidates and fellow master's students who made this period at the LSL so much more enjoyable.

The trunk: I don't know where I would be without the support system of my batchmates, a.k.a "the Aero support group", and everyone at University Church who were by my side, looking out for me during the ups and downs of this Master's journey. I also want to remember my friends from back home, those who have joined me here in Delft, and those that are still many miles away. I hope that the distances between us get shorter, or the travel gets faster/cheaper, I am now in a position to influence both of those factors.

The roots: Finally, I want to thank my family, Appa, Amma and Checha, who form the basis of my support system. They have always lifted me up, and believed in me more than I often believed in myself; they were always there to provide strength when I felt overwhelmed, preventing me from being swept up in the storm, and securing me to the firm foundation.

The soil: As I continue to move forward in life, I want to keep secure in this firm foundation, and build my life on this rock. I hope that it will continue to be my life's wonder to trace the intricate patterns of a world set in motion and sustained by the Unmoved Mover.

Soli Deo gloria

Aashish Mathew Eapen
Delft, March 2026

Abstract

Surface imperfections on laminar aircraft surfaces, such as panel joints and discontinuities, can strongly modify boundary-layer stability. Sharp-edged rectangular bumps (SERBs) combine two widely studied surface features, the Forward-Facing Step (FFS) and a Backward-Facing Step (BFS), and provide a useful geometry for examining how step-induced mean-flow distortion and separation affect the development of Tollmien-Schlichting (TS) waves. However, previous studies on similar bump shapes have mostly considered a single incoming TS-wave amplitude, leaving the dependence of the SERB-induced boundary-layer response on incoming TS-wave amplitude insufficiently resolved.

To investigate how the boundary-layer response to a SERB depends on the amplitude of an incoming forced TS wave, this work combined numerical stability analysis with experiments performed on an unswept flat plate in the low-turbulence environment of the anechoic wind tunnel (A-tunnel) at TU Delft. Dielectric-Barrier Discharge (DBD) plasma actuators were used to force single-frequency TS-wave disturbances while allowing for easy amplitude variation. Surface microphones and Hot-Wire Anemometry (HWA) measurement systems were used to collect data to analyse the harmonic content of the disturbance, its wall-normal structure at the forcing frequency, and its downstream growth, comparing across the clean flat plate with and without the SERB installed over a range of forcing amplitudes. Independent monitoring of forcing consistency was shown to be important in long-duration plasma-forced experiments, where maintaining a consistent forcing amplitude is required. Simultaneous microphone measurements were necessary to distinguish genuine flow-induced amplification from transient variations in actuator output.

The results show that the influence of the SERB is strongly region-dependent: the forced TS-wave behaves like the clean case upstream of the bump and undergoes local amplification in the regions immediately upstream of the FFS and in the region just downstream of the FFS lip, a reduction in growth rate and stabilisation over the bump, and greater amplification downstream of the BFS. Greater forcing amplitudes are associated with a broader redistribution of spectral energy in the wall-normal direction and an earlier loss of a distinct shear-layer instability signature introduced in the recirculation region behind the BFS. The SERB, therefore, does not behave as a simple amplifier of TS waves, but instead produces a region-dependent response, with local amplification ahead of the FFS, reduced growth over the bump, and stronger re-amplification downstream of the BFS, where the response becomes increasingly sensitive to the amplitude of the incoming disturbance.

Contents

List of Figures

List of Tables

Nomenclature

Abbreviations

Abbreviation	Definition	Unit
APG	Adverse Pressure Gradient	
FPG	Favorable Pressure Gradient	
ZPG	Zero Pressure Gradient	
BL	Boundary Layer	
PBL	Parabolised Boundary Layer	
TS	Tollmien-Schlichting	
BFS	Backward-Facing Step	
FFS	Forward-Facing Step	
SERB	Sharp-Edged Rectangurlar Bump	
DBD	Dielectric Barrier Discharge	
OS	Orr-Sommerfeld	
HWA	Hot-Wire Anemometry	
IR	Infrared Thermography	
PSD	Power Spectral Density	
DFT	Direct Fourier Transform	
FFT	Fast Fourier Transform	
SPL	Sound Pressure Level	[dB]
LE	Leading Edge	
TE	Trailing Edge	
PMMA	Poly (methyl methacrylate)	

Symbols

Symbol	Definition	Unit
(U, V, W)	Velocity components of the base flow	[m/s]
(u, v, w)	Velocity components of the perturbation	[m/s]
U_∞	Freestream Velocity	[m/s]
U_e	Velocity at boundary-layer edge	[m/s]
U_h	Velocity at Step/Bump height	[m/s]
f	Frequency	[Hz]
h	Step/Bump height	[m]
kV_{p-p}	kilovolts peak-to-peak	$[10^3 V]$
ρ	Density	[kg/m^3]
ν	Kinematic Viscosity	[kg/s m]
δ^*	Displacement Thickness	[m/s]
δ_{99}	Boundary Layer Thickness	[m/s]
θ	Momentum Thickness	[m]
τ_w	Wall shear stress	[Pa]
μ	Micro	[-]

Non-dimenstional parameters

Symbol	Definition	Formula
Re_{δ^*}	Reynolds number based on displacement thickness	$\delta^* U_\infty / \nu$
Re_{hh}	Reynolds number based on step/bump height	hU_h/ν
Re_h	Reynolds number based on step/bump height	hU_e/ν
Re_x	Reynolds number based on streamwise location	xU_∞/ν
Re_c	Reynolds number based on chord	cU_∞/ν
C_f	Skin friction coefficient	$\tau_w / 2\rho {U_\infty}^2$
C_p	Pressure coefficient	
N_A	Amplitude-based N-factor	$ln(A/A_0)$
N_E	Energy-based N-factor	$ln(E/E_0)$

1

Introduction

This chapter first outlines the motivation for this study in section 1.1, connecting the broader push for efficiency gains to meet emissions-reduction goals to the study of boundary-layer flow control. In relation to this, the fundamentals of the boundary layers are given in section 1.2 with a specific focus on the Tollmien-Schlichting instability in section 1.3. A background on the geometric features in this study is given in section 1.4, with the resulting research questions and objectives for this thesis laid out in section 1.5.

1.1. Motivation

Commercial aviation is a vital component of the global transportation network, yet it also represents a growing source of anthropogenic climate forcing. Comprehensive assessments by Costantini et al. (2022) show that aviation contributed approximately 3.5% of total human-induced radiative forcing in 2018, underscoring the sector's disproportionate climate impact relative to its economic scale. Broader societal reflections on aviation's environmental footprint further highlight the need for a more sustainable trajectory for air transport (Gössling, 2020). In response, international and European roadmaps, such as ICAO environmental standards and Europe's Flightpath 2050 (Krein & Williams, 2012) set ambitious long-term objectives, including substantial reductions in CO_2 emissions per passenger-kilometre. Achieving these targets requires progress across multiple fronts, with aerodynamic efficiency remaining one of the most direct and impactful levers for lowering energy consumption.

A substantial fraction of aircraft drag arises from viscous skin friction, particularly on large transport wings, nacelles, and empennage surfaces. As emphasised in classical and contemporary surveys (Schrauf, 2005), even modest increases in skin-friction drag translate directly into increased fuel consumption and emissions. This increase is primarily due to the higher wall shear stress associated with turbulent boundary layers, where enhanced mixing leads to steeper velocity gradients at the wall and therefore greater frictional resistance. For this reason, modern aerodynamic design places considerable emphasis on delaying laminar-turbulent transition and preserving favourable boundary-layer behaviour over as much of the lifting surface as practically achievable. However, the ability to retain laminar flow in real operational conditions is highly sensitive to the quality of the aerodynamic surface. Manufacturing tolerances, installation steps, repairs, and in-service contamination all introduce small geometric deviations, such as steps, gaps, bumps, or regions of waviness- that can prematurely trigger boundary-layer transition. Industrial experience repeatedly confirms that these imperfections can erode the performance benefits predicted at the design stage (Hansen, 2010; Wong et al., 2021).

The physical basis for this sensitivity lies in the receptivity of laminar boundary layers to disturbances. On unswept or mildly swept surfaces, transition is dominated by the amplification of Tollmien–Schlichting (TS) waves. Previous research on transition mechanisms (Arnal & Archambaud, 2008; Joslin, 2025) shows that TS waves are particularly sensitive to perturbations in the surface geometry or pressure gradient. Localised imperfections such as steps or shallow bumps (typically with small height relative to the local boundary-layer displacement thickness, $h/\delta^* \lesssim 0.5$), distort the mean veloc-

ity profile and may induce small separation bubbles, both of which enhance boundary-layer instability growth. Even when the flow remains attached, the pressure-gradient modification imposed by the bump can alter the stability characteristics of the boundary layer, leading to increased disturbance amplification. Studies focused specifically on imperfections confirm this sensitivity: surface steps, bumps, or small humps produce measurable increases in TS wave amplification, causing earlier transition relative to clean-surface baselines (Perraud et al., 2004, 2014). These effects persist across a wide range of Reynolds numbers, highlighting the importance of quantifying the interaction between disturbances and geometric imperfections.

Within this context, the present work examines the effect of varying TS wave amplitudes on the flow over a rectangular surface bump mounted on a flat plate. An unswept flat-plate geometry deliberately isolates the two-dimensional transition process, avoiding the additional instabilities caused by crossflow, attachment-line contamination, or three-dimensional wing curvature. By imposing TS waves of known frequency and amplitude and examining their evolution in the presence of a well-defined geometric perturbation, this study investigates how disturbance amplitude and a localised surface imperfection together affect transition onset. This understanding is essential for determining realistic surface tolerance criteria in aerodynamic design and for assessing the operational robustness of laminar-flow performance in the presence of surface defects.

1.2. Boundary Layers

subsection 1.2.1 lays out some fundamental concepts and parameters when talking about boundary layers, and subsection 1.2.2 provides a background on receptivity and the role of disturbances in the initiation of boundary-layer instabilities.

1.2.1. Boundary Layer Fundamentals

Viscosity is the fundamental fluid property responsible for internal friction and momentum diffusion between adjacent layers of fluid. In the presence of a solid surface, viscous effects create a region of strong velocity gradients known as the boundary layer. For a Newtonian fluid, the shear stress acting on a plane parallel to the wall is proportional to the velocity gradient normal to that plane (F. M. White & Majdalani, 2022):

$$\tau = \mu \frac{\partial u}{\partial y}, \tag{1.1}$$

where τ is the shear stress, μ is the dynamic viscosity, and $u(x, y)$ is the streamwise velocity component.

The theoretical foundation of boundary-layer analysis originates from Prandtl's 1904 formulation, which demonstrated that the Navier–Stokes equations simplify considerably within the thin region adjacent to a solid surface at high Reynolds numbers (Schlichting & Gersten, 2017). For steady, two-dimensional flow over a flat plate at zero pressure gradient, the boundary-layer approximations reduce the governing equations to

$$\frac{\partial u}{\partial x} + \frac{\partial v}{\partial y} = 0, \tag{1.2}$$

$$u\frac{\partial u}{\partial x} + v\frac{\partial u}{\partial y} = \nu \frac{\partial^2 u}{\partial y^2}, \tag{1.3}$$

where $\nu = \mu/\rho$ is the kinematic viscosity. For this special case, Blasius (1908) showed that these equations admit a self-similar solution. Introducing the similarity variable

$$\eta = y\sqrt{\frac{U_\infty}{2\nu x}}, \tag{1.4}$$

and the similarity streamfunction

$$\psi(x, y) = \sqrt{2\nu U_\infty x}\, f(\eta), \tag{1.5}$$

leads directly to the relations

$$u = U_\infty f'(\eta), \qquad v = \sqrt{\frac{\nu U_\infty}{2x}}\big[\eta f'(\eta) - f(\eta)\big]. \tag{1.6}$$

Substitution into the momentum equation yields the Blasius ordinary differential equation

$$f''' + \frac{1}{2} f\, f'' = 0, \tag{1.7}$$

subject to

$$f(0) = 0, \qquad f'(0) = 0, \qquad f'(\eta \to \infty) \to 1. \tag{1.8}$$

The resulting velocity profile $u/U_\infty = f'(\eta)$ defines the canonical laminar boundary layer for a zero-pressure-gradient flat plate (Schlichting & Gersten, 2017; F. M. White & Majdalani, 2022). This profile forms the basis for computing boundary-layer thicknesses and integral parameters used later in stability and transition analysis.

The boundary-layer thickness, denoted $\delta_{99}(x)$, is conventionally defined as the distance from the wall at which the streamwise velocity reaches 99% of the freestream velocity,

$$u(y = \delta_{99}) = 0.99\, U_\infty. \tag{1.9}$$

For the Blasius solution, the boundary layer grows downstream according to (Schlichting & Gersten, 2017; F. M. White & Majdalani, 2022)

$$\delta_{99}(x) = 5.0\sqrt{\frac{\nu x}{U_\infty}}, \tag{1.10}$$

so that the local Reynolds number based on x, $Re_x = U_\infty x/\nu$, determines the local thickness. Expressed nondimensionally,

$$\frac{\delta_{99}(x)}{l} = \frac{5}{\sqrt{Re_l}}\sqrt{\frac{x}{l}}, \tag{1.11}$$

which highlights the characteristic $Re_x^{-1/2}$ growth of laminar boundary layers under zero pressure gradient.

Integral boundary-layer parameters

Because the velocity profile inside the boundary layer differs from the outer inviscid flow, the mass flux and momentum flux are reduced. These effects are quantified using integral thickness parameters derived from the velocity profile.

The displacement thickness $\delta^*(x)$ accounts for the reduction in mass flow due to the lower velocities in the boundary layer:

$$\delta^*(x) = \int_0^\infty \left(1 - \frac{u}{U_\infty}\right) \mathrm{d}y = 1.7208\sqrt{\frac{\nu x}{U_\infty}}. \tag{1.12}$$

This quantity measures the apparent outward displacement of the outer flow streamlines (Schlichting & Gersten, 2017).

The momentum thickness $\theta(x)$ quantifies the reduction in momentum flux due to viscous effects:

$$\theta(x) = \int_0^\infty \frac{u}{U_\infty}\left(1 - \frac{u}{U_\infty}\right) \mathrm{d}y = 0.664\sqrt{\frac{\nu x}{U_\infty}}. \tag{1.13}$$

The shape factor

$$H = \frac{\delta^*}{\theta} \approx \frac{1.7208}{0.664} \approx 2.59, \tag{1.14}$$

characterises the "fullness'' of the laminar Blasius profile and provides a useful indicator for incipient separation and stability (Schlichting & Gersten, 2017).

1.2.2. Receptivity and Paths to Transition

In practical flows, boundary-layer transition does not occur in isolation but is triggered by external disturbances such as freestream turbulence, acoustic waves, surface roughness, or wakes from upstream bodies. The process by which these external perturbations are converted into instability modes of the boundary layer (e.g. TS waves, crossflow vortices, or streaks) is known as receptivity. Depending on the disturbance environment and the mean-flow configuration, different transition scenarios may arise, including linear TS wave growth, bypass transition, separation-induced transition, or crossflow-dominated routes (Reshotko, 2008).

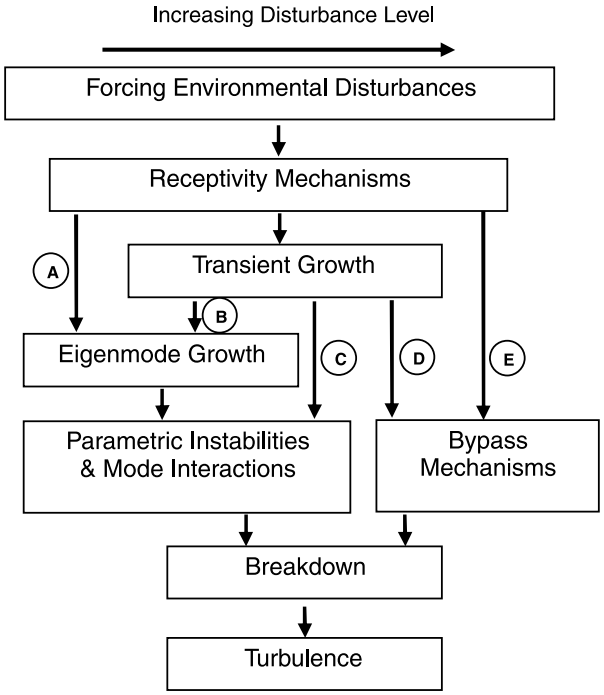

Figure 1.1: Schematic paths to transition for wall-bounded flows, highlighting different instability and breakdown mechanisms (Reshotko, 2008).

In the present work, the focus is on low-disturbance environments where the TS wave-dominated transition is the primary route, and the mean flow can be approximated locally by the Blasius boundary layer derived in the previous subsection.

1.3. Tollmien-Schlichting Waves

For a flat plate under zero pressure gradient, the primary linear instability mechanism of the laminar boundary layer is the TS wave. These disturbances are two-dimensional, viscous, streamwise-travelling waves whose amplitude is concentrated close to the wall and decays exponentially into the freestream. Their spatial structure and amplification behaviour within the Blasius boundary layer are well documented by Mack (1984) and form the basis for stability-based transition prediction in low-disturbance environments.

The theoretical existence of unstable waves in a laminar flat-plate boundary layer was first demonstrated by Tollmien (1929), who showed that the linearised boundary-layer equations admit exponentially amplifying solutions. Schlichting (1950) later refined these calculations and more accurately mapped the

parameter ranges of instability. Direct experimental confirmation was provided by Schubauer and Skramstad (1947), whose low-disturbance wind-tunnel measurements revealed oscillatory disturbances with exponential downstream growth, validating the theoretical predictions and establishing TS waves as the dominant instability mode in quiet-flow flat-plate conditions.

Baines et al. (1996) described a TS wave as the outcome of an interaction between an inviscid vorticity-wave component, which propagates on the mean shear, and a family of viscous modes required to satisfy the no-slip condition. This interaction generates a disturbance Reynolds-stress pattern with the correct phase relationship to extract energy from the mean flow. In terms of the disturbance kinetic-energy budget, amplification is driven by the production term

$$P = -\langle u'v' \rangle \frac{\mathrm{d}U}{\mathrm{d}y}, \tag{1.15}$$

where the correlation $\langle u'v' \rangle$ becomes significant only within the viscous sublayer. As shown in the schematic of Figure 1.2, this near-wall region is where the disturbance-induced tilting of vorticity leads to a non-zero Reynolds stress, enabling energy transfer from the base flow to the disturbance (Bippes, 1999; Boiko et al., 2012).

Because this amplification mechanism depends sensitively on the shape of the near-wall mean-flow profile, TS waves respond strongly to even mild modifications of the boundary layer. Experimental work by Barahona (2022), for example, demonstrates that small geometric features (such as forward-facing steps) can alter the phase and amplitude of the fundamental TS mode and modify the wall-normal structure of the disturbance.

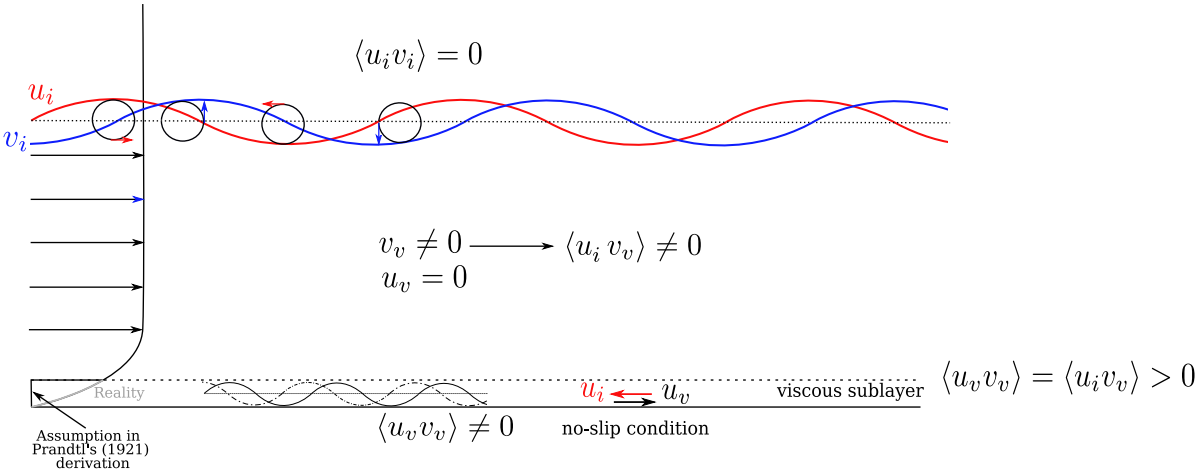

Figure 1.2: Schematic diagram showing the interaction process that cause TS wave growth, from Barahona (2022) inspired by Bippes (1999)

1.4. Sharp-Edged Rectangular Bumps

Surface steps represent canonical two-dimensional roughness elements whose influence on boundary-layer stability has been studied extensively. Forward-Facing Steps (FFS) refer to a local increase in the surface height in the streamwise direction, characterised by right angles at the interface. Backwards-facing steps (BFS) represent a similar geometric discontinuity, but with a local decrease in surface height. Both the BFS and FFS are types of 2D roughness elements which are often observed in commercial aircraft as surface features such as panel joints/discontinuities on the wings, stabilisers, or fuselage.

In this work, the term Sharp-Edged Rectangular Bump (SERB) is used to describe the geometry consisting of an FFS followed by a BFS of equal height. Recently, more studies have focused on the transition performance of more rounded rectangular geometries (Franco Sumariva et al., 2020) to even gaussian humps (Ehrenstein & Gallaire, 2009; Franco Sumariva et al., 2020; Gallaire et al., 2007; Gao et al., 2011; Marquillie & Ehrenstein, 2003; Morais, 2023; Park & Park, 2013; Rius-Vidales et al., 2025;

Westerbeek et al., 2023), and thus the current study specifies the term SERB, following Dos Santos et al. (2025), to distinguish the geometry in this study from these more rounded shapes.

As this geometry is essentially a superposition of a FFS and a BFS, the current understanding of the flow physics around these geometries will be discussed below, in addition to the current literature pertaining to SERBs. This interpretation is formally justified by Crouch and Kosorygin (2020), who show that the destabilisation produced by a rectangular protrusion is approximately the sum of the individual FFS and BFS contributions, so long as the plateau length is sufficiently long relative to the displacement thickness. The bump in this study has an aspect ratio of $L : h = 50{:}1$, matching the canonical configuration used by Crouch and Kosorygin (2020) for "wide protrusions."

Thus, the physical mechanisms identified in the literature (local adverse/favourable pressure gradients, separation bubbles, TS wave scattering, receptivity changes) apply directly to the SERB, giving a natural framework for interpretation: a rectangular protrusion behaving as an FFS-induced destabilisation zone, a plateau with modified boundary-layer thickness, and a BFS-induced strong amplification region.

The following non-dimensional terms are used in relation to bumps/steps

$$\mathrm{Re}_h = \frac{U_e h}{\nu}, \qquad \mathrm{Re}_{hh} = \frac{U_{h,\mathrm{clean}}\, h}{\nu}, \qquad \mathcal{H} = \frac{h}{\delta^*},$$

where U_e is the boundary-layer edge velocity at the step location, δ^* is the local displacement thickness, ν is the kinematic viscosity, and U_h is the streamwise velocity at the wall normal y- location corresponding to the step or bump height, h .

1.4.1. Effect of FFS on TS wave growth

A forward-facing step introduces a brief but sharp region of adverse pressure gradient, which tends to locally amplify incoming TS waves. The presence of an FFS typically induces two distinct regions of flow separation:

The first recirculation region forms immediately upstream of the step due to the locally adverse pressure gradient, producing a short near-wall separation zone. Within this region, the mean velocity profile becomes strongly distorted and locally inflectional, resulting in enhanced shear and increased susceptibility to instability. As a consequence, incoming TS waves experience local amplification while traversing this modified base flow.

The second recirculation region downstream of the step edge on the plateau surface with more complex effects on the oncoming TS wave. As the TS wave passes over the step, it undergoes significant topological distortion; the streamwise perturbation component ($|\hat{u}|$) decays while the wall-normal component ($|\hat{v}|$) amplifies rapidly (Barahona, 2022), effectively transferring energy between components before returning back to the dominant TS mode further downstream for subcritical steps (Edelmann, 2014).

While earlier studies suggested an abrupt jump in transition location once a critical height is reached, Costantini et al. (2022) observed a more gradual upstream movement of the transition front with increasing relative step height h/δ^*, with the relationship between the relative transition location and the non-dimensional step parameters (h/δ^* and Re_h) being largely independent of the Mach number (in the subsonic regime).

In the scaling proposed by Crouch and Kosorygin (2020), the influence of an FFS is captured by a reduction in the N-factor of approximately

$$\Delta N \approx 1.6\, \frac{h}{\delta^*},$$

indicating a proportional but comparatively weak effect when h/δ^* is below 1. However, Hildebrand et al. (2025) found that for $h/\delta^* > 0.17$, the FFS begins to reduce the transition N-factor significantly.

1.4.2. Effect of BFS on TS wave growth

The flow around a Backward-Facing Step (BFS) is characterised by the separation of the boundary layer at the sharp step corner, creating a free shear layer that eventually reattaches to the wall downstream,

enclosing a recirculation region (Armaly et al., 1983). Similarly, the controlled-disturbance experiments of Hasan (1992) showed that even small perturbations introduced upstream of the BFS undergo significant amplification inside this separated region, highlighting the susceptibility of the detached shear layer to upstream perturbations.

Although many classical BFS studies are performed in channel-flow configurations (Armaly et al., 1983; Biswas et al., 2004; Hasan, 1992), the fundamental flow features they describe- like the laminar separation bubble, separated shear layer, and the associated amplification of small disturbances- are driven by the geometry and can therefore be used to draw a qualitative comparison with the current flat-plate SERB case.

The separated shear layer behind the BFS has a pronounced velocity inflection, making it highly receptive to both Kelvin-Helmholtz (KH) instability, with the TS waves experiencing greater growth rates than in an attached laminar boundary layer. This behaviour has been captured in detail by the linear stability analyses of Hildebrand et al. (2020) and Hildebrand et al. (2022), showing that the BFS causes a sharp rise in local growth rates that is well predicted by PSE and HLNSE models. Complementary DNS studies by Teng and Piomelli (2022) show that the separated shear layer above the recirculation bubble acts as a strong convective amplifier, producing substantial transient growth of disturbances entering the bubble.

Hasan (1992) identified two distinct modes of instability in the reattaching shear layer;

- Shear Layer Mode (Kelvin-Helmholtz): This is a high-frequency instability associated with the natural roll-up of the shear layer vortices with a Strouhal number based momentum thickness at separation (θ), $St_\theta = f\theta/U \approx 0.012$
- Step Mode: A lower-frequency instability associated with the flapping of the shear layer and vortex merging, which scales with the step height (h). The Strouhal number for this mode $St_h = fh/U \approx 0.185$

After reattachment, the boundary layer remains thickened, distorted, and carries amplified disturbances generated inside the separation bubble. While the flow can reattach laminarly (Armaly et al., 1983), a combination of TS wave amplification and KH-type instability often pushes the flow toward transition shortly downstream of reattachment, especially when the incoming boundary layer is already unstable, as is the case in the present experiment with forcing.

According to the scaling proposed by Crouch and Kosorygin (2020), the BFS contribution to TS wave amplification can be approximated as

$$\Delta N \approx 4.4 \, \frac{h}{\delta^*},$$

which is typically two to three times larger than the FFS contribution. Given that the BFS in the present experiment is located at $x = 795$ mm, where the boundary layer has already been destabilised by the FFS, the strong amplification expected behind the BFS aligns with the placement of microphones and hot-wire stations downstream of the bump.

While the FFS modifies the disturbance field in its immediate vicinity, these studies consistently show that its overall influence on downstream transition location is relatively modest compared with that of a BFS of the same height (Risius & Costantini, 2025; Wang & Gaster, 2005).

1.4.3. Existing literature on SERBs

While the majority of historical studies focused on isolated FFS and BFS, a growing body of work examines the combined effect of sharp-edged rectangular protrusions.

Crouch and Kosorygin (2020) provided a theoretical framework for such configurations, demonstrating that rectangular bumps behave as a linear superposition of the constituent FFS and BFS effects provided $L/h \gtrsim 40$. This study examines the criticality steps, bumps and gaps, with the aspect ratio for the bumps/gaps kept constant at $L/h = 50$. This was done to make sure that the length of the bump would be approximately 5 times the wavelength of the dominant TS wave frequency at the location of the bump.

Placidi et al. (2020) investigated sharp-edged rectangular bumps of varying heights and introduced the displacement-thickness-based scaling $\frac{h}{\delta^*_B}$, as an appropriate nondimensional parameter for comparing bump-induced effects across different Reynolds numbers. Although the present experiment employs only a single bump height, this scaling was used to ensure that the chosen SERB height lies within the same nondimensional range explored by Placidi et al. (2020), ensuring consistent comparison with prior literature.

Dos Santos et al. (2025) further investigated sharp-edged rectangular bumps in the context of acoustic receptivity, showing how external disturbances such as background acoustic waves are converted into boundary-layer instabilities at the SERB. Their results quantify how the amplitude of the induced instability varies with bump height and acoustic-wave amplitude, enabling estimation of whether this background receptivity effect is negligible compared to the plasma forcing used in the present experiment.

The influence of 2D humps on a 2D laminar boundary layer was conducted using direct numerical simulations (DNS) by Worner et al. (2003) for a small bump ($h/\delta^* = 0.47$, corresponding to a height-based Reynolds number, $Re_h = U_\infty h/\nu = 511$) with streamwise width approximately equal to half of the TS wavelength (reduced frequency, $F = 2\pi f\,\nu/U_\infty^2 \times 10^6 = 49.34$) triggered by a disturbance strip located at $x = 2.78$ (Reynolds number based on displacement thickness, $Re_{\delta^*} = U_\infty \delta^*/\nu = 907$. At the FFS of this small bump, a decrease in the TS wave amplitude was observed, which the author ascribed to boundary layer thinning. At the BFS of the bump, TS wave amplification was observed, which the author ascribed to the separation region formed behind the BFS. Due to the amplification caused by the BFS being higher than the attenuation due to the FFS, the net result is boundary layer destabilisation. On varying the height and width of the bump, the author noted that the width of the bump plays a minor role, while the larger influence on the TS wave amplification caused by the bump height.

1.5. Research questions and objectives

Research Gap: Although the flowfield around Sharp-Edged Rectangular Bumps (SERBs), including the associated FFS and BFS behaviour, have been investigated for different bump heights and aspect ratios, previous work has largely considered only a single, fixed disturbance amplitude. As a result, the dependence of the SERB-induced boundary-layer on the amplitude of the incoming TS wave remains unquantified with respect to harmonic content, relative FFS/BFS influence, and the resulting N-factor increment.

Furthermore, external/operational factors can cause variations in TS-wave amplitude over time when using plasma-actuators for TS-wave excitation. Previous studies, typically using acoustic forcing, vibrating-ribbon forcing, or short-duration plasma-actuated experiments, have not addressed how to ensure amplitude consistency over extended measurements.

To fill this research gap, the research objective of this thesis can be formulated:

To show the effects of a SERB on TS waves of varying amplitudes over a flat plate with and without the SERB, using numerical stability analysis and experimental flow measurement techniques

The research question that arise to fulfil this goal are defined as:
How does the boundary-layer response induced by the SERB depend on the amplitude of the incoming TS wave?

1. How does the harmonic content of the boundary layer upstream, over, and downstream of the SERB change as the amplitude of the incoming TS wave is varied?
2. How does the SERB-induced instability growth in the boundary layer depend on the amplitude of the incoming TS wave?

To accomplish this goal, the rest of this thesis is structured as follows:

Chapter 2 discusses the methodology by which the boundary layer stability for the clean (no SERB), unswept flat plate is first assessed using an in-house Orr-Sommerfeild solver to identify the most unstable TS wave-frequency (at the streamwise location of the FFS of the SERB using N-factor analysis),

which is then forced experimentally using a plasma actuator, with Hot Wire Anemometry (HWA) and microphone data acquisition systems. The methodology for constructing the test section and setting up the wind tunnel test campaign is also detailed in this chapter.

Chapter 3 details the results that can be obtained from the collected data, and their implications.

And finally Chapter 4 is a discussion of the conclusions that can be made based on the results of the work during the course of this thesis, as well as recommendations for further improvement/analysis.

2

Methodology

This chapter describes the methods used to numerically and experimentally address the research questions posed in this study. Section 2.1 details the numerical study that informed the formation of the experimental test matrix. The wind-tunnel facility and test section are described in section 2.2, followed by the bump design and installation in section 2.3, the method of TS-wave excitation in section 2.4, and the insertion plate integrated into the test section in subsection 2.4.2. The measurement techniques used throughout the campaign are presented in section 2.5, followed by the applied corrections in section 2.6 and the data-processing methods in section 2.7.

2.1. Numerical Study and Experimental Test-Matrix

This section describes the numerical study used to characterise the boundary-layer baseflow that was performed prior to the experimental campaign to guide the design of the experiment. The governing stability framework is introduced in subsection 2.1.1, followed by a description of the boundary-layer solver in subsection 2.1.2 and the linear stability solver in subsection 2.1.3. Finally, the resulting stability predictions used to define the experimental forcing conditions and test matrix are discussed in subsection 2.1.4 with the experimental test matrix given in subsection 2.1.5.

2.1.1. Linear Stability Theory

The laminar boundary layer developing over a flat plate at zero pressure gradient is susceptible to the growth of Tollmien–Schlichting (TS) waves beyond a critical Reynolds number. A schematic illustration of the transition process, from laminar flow through linear instability and secondary breakdown to turbulence, is shown in Figure 2.1 (F. M. White & Majdalani, 2022).

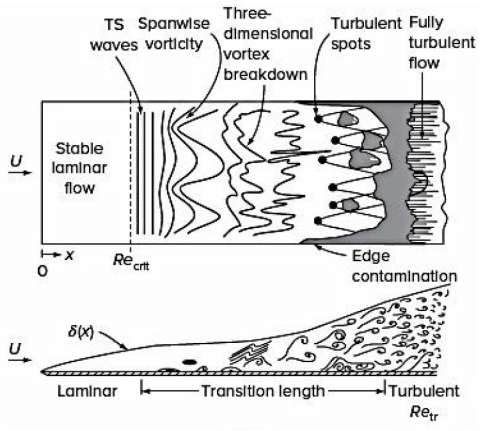

Figure 2.1: Laminar–turbulent boundary-layer transition for a flat plate at zero incidence (F. M. White & Majdalani, 2022).

In the present work, the stability of the numerically computed boundary-layer baseflow was analysed using linear stability theory in a spatial framework. The instantaneous flow field was decomposed as

$$\mathbf{u}(x, y, t) = \mathbf{U}(x, y) + \mathbf{u}'(x, y, t), \tag{2.1}$$

where $\mathbf{U}(x, y)$ denotes the steady baseflow obtained from the boundary-layer solver, and $\mathbf{u}'$ represents infinitesimal disturbances.

Assuming two-dimensional wave-like perturbations of the form

$$\begin{bmatrix} u'(x, y, t) \\ v'(x, y, t) \\ p'(x, y, t) \end{bmatrix} = \begin{bmatrix} \hat{u}(y) \\ \hat{v}(y) \\ \hat{p}(y) \end{bmatrix} e^{i(\alpha x - \omega t)} \tag{2.2}$$

and adopting a spatial formulation in which the forcing frequency ω is real and the streamwise wavenumber $\alpha = \alpha_r + i\alpha_i$ is complex, linearisation of the incompressible Navier–Stokes equations about the baseflow leads to the classical Orr–Sommerfeld eigenvalue problem:

$$\left(D^2 - \alpha^2\right)^2 \hat{v} = i\alpha Re \left[(U - c)\left(D^2 - \alpha^2\right)\hat{v} - U''\hat{v}\right], \tag{2.3}$$

with homogeneous boundary conditions enforcing no-slip at the wall and decay in the free stream. Here $D = \mathrm{d}/\mathrm{d}y$, $c = \omega/\alpha$ is the complex phase speed, and Re is defined using local boundary-layer scaling.

For each streamwise station, the Orr–Sommerfeld problem was solved using the numerically computed baseflow $U(x, y)$, yielding the complex wavenumber $\alpha(x, f)$. Spatial instability corresponds to $\alpha_i < 0$, indicating exponential growth of disturbances in the downstream direction.

Neutral stability and N-factor formulation
Neutral stability occurs where $\alpha_i = 0$, defining the lower and upper branch neutral curves that bound the region of TS-wave amplification. Within this unstable region, the disturbance amplitude evolves as

$$a(x) = a_0 e^{\int_{x_0}^{x} -\alpha_i(x', f)\,\mathrm{d}x'} \tag{2.4}$$

The integrated amplification is conveniently expressed using the logarithmic N-factor,

$$N(x, f) = \int_{x_0}^{x} -\alpha_i(x', f)\,\mathrm{d}x', \tag{2.5}$$

which represents the cumulative exponential growth of TS waves along the boundary layer.

In classical flat-plate experiments under low-disturbance conditions, transition is typically observed when N reaches a critical value $N_{\mathrm{crit}} \approx 9$ (Van Ingen, 2008). This forms the basis of the widely used e^N transition-prediction method.

In the present case, the computed N-factor curves for the 1.35 m flat plate remained below this critical threshold for all investigated frequencies, consistent with the absence of natural transition observed experimentally.

In order to get initial information for the sizing and placement of components for the preliminary design. The boundary layer flow and TS wave stability needed to be understood.

Two coupled, in-house solvers were used for this purpose: a boundary-layer solver to simulate the baseflow and an Orr-Sommerfeld (OS) stability solver that used the calculated baseflow to solve the eigenvalue problem and assess the stability of TS-waves at different frequencies.

The boundary layer solver is run for U_∞=17.4 m/s (corresponding to a chord-based Reynolds number, $Re_c = 1.5 * 10^6$) for the entire length of the flat plate (chord, $c = 1.35$ m).

2.1.2. Boundary Layer Solver

The baseflow was computed using an in-house parabolised boundary-layer (PBL) solver that marches downstream from an initial similarity profile. At the inlet ($x = 0.005$ m), a Falkner–Skan profile with $\beta = 0$ (Blasius solution) was imposed as the inflow condition.

The computational domain extended from $x = 0.005$ to $x = 1.350$ m, discretised using $N_x = 2000$ streamwise points and $N_y = 100$ Chebyshev collocation points in the wall-normal direction. The outer velocity was held constant at $U_e(x) = U_\infty$, consistent with the zero pressure gradient (ZPG) assumption. A grid convergence study confirmed that increasing N_y beyond 100 led to less than 0.2% change in δ_{99} and shape factor H.

After solving, the flow was non-dimensionalised using the local similarity scale $\delta_0 = \sqrt{\nu x/U_\infty}$, allowing the boundary layer to be interpreted in terms of local Reynolds number $Re_x = U_\infty x/\nu$.

Figure 2.2 shows the displacement thickness δ^*, momentum thickness θ, boundary-layer edge δ_{99}, and shape factor $H = \delta^*/\theta$ were computed at every streamwise location.

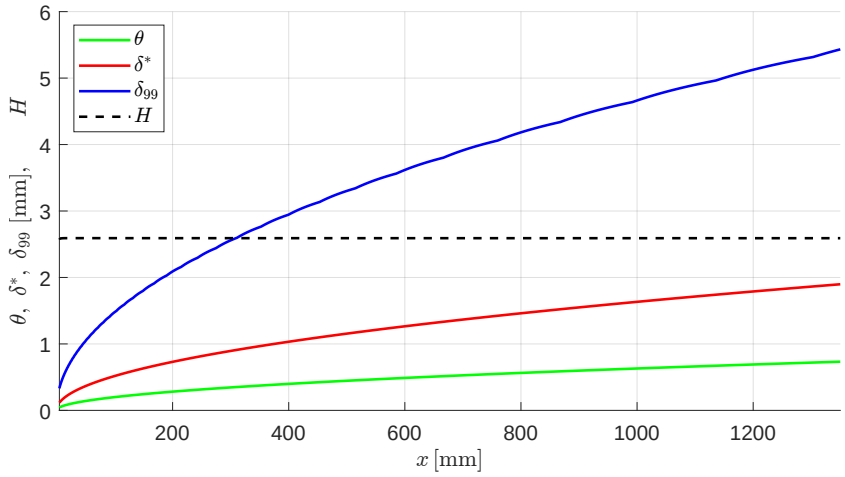

Figure 2.2: Boundary-layer parameters along the flat plate: displacement thickness, δ^*, momentum thickness, θ, boundary-layer thickness, δ_{99}, and shape factor H.

The velocity profiles show excellent agreement with canonical Blasius profiles. The shape factor stabilises near $H \approx 2.59$ across most of the domain, consistent with a ZPG laminar boundary layer. Small oscillations near the trailing edge are attributed to limitations in the edge-detection criterion for δ_{99}.

2.1.3. Linear Stability Theory Solver

The stability analysis was performed using an in-house local Orr-Sommerfeld solver. The solver uses the computed baseflow at each x-station as input and solves a linear eigenvalue problem to determine the temporal stability of the TS waves.

The analysis assumes a parallel baseflow locally at each streamwise location and neglects streamwise growth of disturbances (local linear stability analysis, LLSA). While this assumption omits weak non-parallel effects, it is standard practice for flat plate analysis and provides good estimates of critical frequencies and amplification rates.

The solver was run for a frequency sweep from $f = 50$ to 500 Hz. For each x and f, the most unstable mode was extracted (largest $\alpha_i < 0$). Neutral stability curves were constructed by identifying locations where the imaginary part of the complex wavenumber α_i crosses zero.

N-factor Integration: The spatial amplification of TS waves was quantified using the N-factor method:

$$N(x, f) = \int_{x_{\text{neutral}}}^{x} -\alpha_i(x', f)\, dx'$$

where x_{neutral} is the location of the first neutral point for that frequency. Only the growing part of the wave (i.e., where $N > 0$) is retained. These results were used to identify the most amplified frequencies at given x-locations (e.g., bump, actuator trigger) by predicting spatial growth envelopes for TS waves. This supported the experimental selection of forcing frequency for active control.

Table 2.1 shows some of the input parameters used for the numerical study. The output of the stability solver, including neutral curves and N-factor curves, is presented in subsection 2.1.4.

Parameter	Symbol	Value
Chord length	c	1.35 m
Freestream velocity	U_∞	17.4 m/s
Kinematic viscosity	ν	1.511×10^{-5} m^2/s
Chord Reynolds number	Re_c	1.5×10^6
Streamwise resolution	N_x	2000
Wall-normal resolution	N_y	100
TS wave frequencies analysed	f	50–500 Hz
Chebyshev domain height	$y_{\max}$	$2\delta_{99}(x)$

Table 2.1: Summary of key numerical parameters

2.1.4. Use of Stability Results for Experimental Planning

Frequency selection:

Figure 2.3 shows the plot of the imaginary wavenumber, α_i, from stability calculations obtained using an in-house OS stability solver, with the positive values of this α_i not shown in this figure. The results in a curved region, enclosing a region where α_i is negative, i.e the unstable region, where the TS wave of a certain frequency is growing. A specific frequency is damped (positive α_i) before it enters this unstable region, with the first point where $\alpha_i = 0$ is the lower border/branch of this unstable region, and continues to be amplified until it reaches the second $\alpha_i = 0$ point at the upper branch of the unstable region. This figure shows us that higher frequency TS waves reach the amplification region earlier, but the distance over which these higher frequencies are amplified is less than that of the lower frequencies.

In Figure 2.4, the N-factors of the frequencies from the stability calculation are shown from 50-350 Hz. These are plotted up to an x-location of 1.350 m (the location of the downstream end of the flat plate before the pressure adjustment flap). It is important to note that none of the frequencies considered reached the reference value $N = 9$ within the length of the flat plate. This value is included only as a representative benchmark from transition literature for relatively low-disturbance external flows, rather than as a calibrated critical threshold for the present experimental facility. The actual critical N-factor may differ depending on the disturbance environment, receptivity, and tunnel-specific conditions. Since no transition was observed within the measurement domain, a critical N-factor could not be determined for the present case. Nevertheless, the fact that the computed N-factors remain below this commonly used benchmark is consistent with the Infrared Thermography (IRT) measurements, which indicated no transition over the full flat-plate length (more details on the setup and use of IRT are given in subsection 2.5.6). It should also be noted that the e^N method is a linear prediction tool and does not account for nonlinear disturbance interactions or other flow phenomena that may develop in the boundary layer and influence the eventual onset of transition.

An ideal location for forcing a specific frequency is at its neutral point (corresponding to the lower branch of the unstable region in Figure 2.3, or equivalently the first $N = 0$ location for that frequency in Figure 2.4), or further downstream within the amplification region, where the slope of the N-factor curves is positive, i.e. $dN/dX > 0$.This amplification region lies between the lower and upper branches of the stability diagram in Figure 2.3, and corresponds to the region between $N = 0$ and the maximum

of the N-factor curve for a specific frequency, as seen in Figure 2.4. This is because TS disturbances are linearly damped upstream of the neutral point, such that any forcing applied before this neutral point would be attenuated before entering the amplifying regime.

This was not possible with the current test section (based on the location of insertion plates); and so, the plasma actuator was placed at a streamwise location of 0.380 m indicated by the vertical dashed black line in Figure 2.4. This location was also chosen based on previous experiments that used the same experimental setup for TS wave studies (Garcia Villasol, 2025). Though this location is ahead of the neutral point, most frequencies are still growing/ being amplified, allowing for the triggered frequency to grow downstream.

The most amplified frequency (largest dN/dx) at this trigger location was found to be 251.4 Hz, with an N factor of 1.081 at the trigger location, reaching a global peak of N = 2.470 at x = 0.6411 m. This frequency would be an ideal choice for the trigger frequency, with the location where it peaks being the ideal location for the bump. However, this bump location would coincide with a crossbar element on the flat plate setup, limiting the viability of fixing microphones to monitor the amplitude of the triggered frequency just ahead of the SERB's FFS. Similar reasoning was used by Garcia Villasol (2025) to select the control actuator location using the same flat plate setup. Based on these operational constraints, and setup configurations from previous studies, the location of the SERB FFS was fixed at x= 0.74m, marked by a vertical dashed line in Figure 2.3.

In Figure 2.4, the envelope of the maximum N-factors at each x location is marked in black. The maximum N factor at the location of the SERB leading edge, 0.74 m, is 3.08 (yellow circle in Figure 2.4) for a frequency of 206 Hz (orchre yellow curve in Figure 2.4, and horizontal dashed line in Figure 2.3). This frequency was used as an initial guess when determining the trigger frequency in situ for the experimental campaign. During the experimental campaign, the microphone just in front of the FFS of the SERB (Mic 8) was monitored. Multiple frequencies around 206 Hz were then triggered (frequency sweep between 175 Hz and 225 Hz) to see which frequency showed the largest amplitude increase in the FFT readout of this mic, before and after triggering (trigger voltage and Reynolds number maintained constant during the frequency sweep). The 210 Hz frequency was found to be the most amplified at this location, and was therefore maintained as the trigger frequency for the entire experiment.

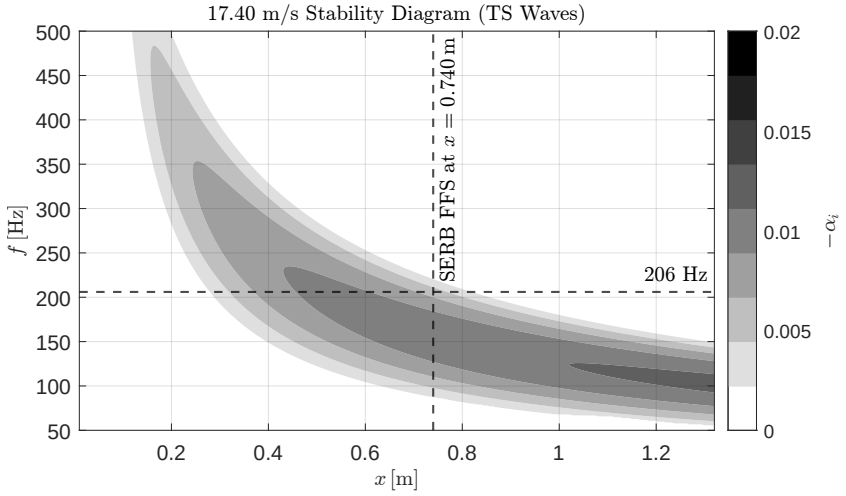

Figure 2.3: Stability diagram from the OS solver at a $U_\infty = 17.40$ m/s ($Re_c = 1.5 \times 10^6$), for flat plate chord length, c =1.35 m.

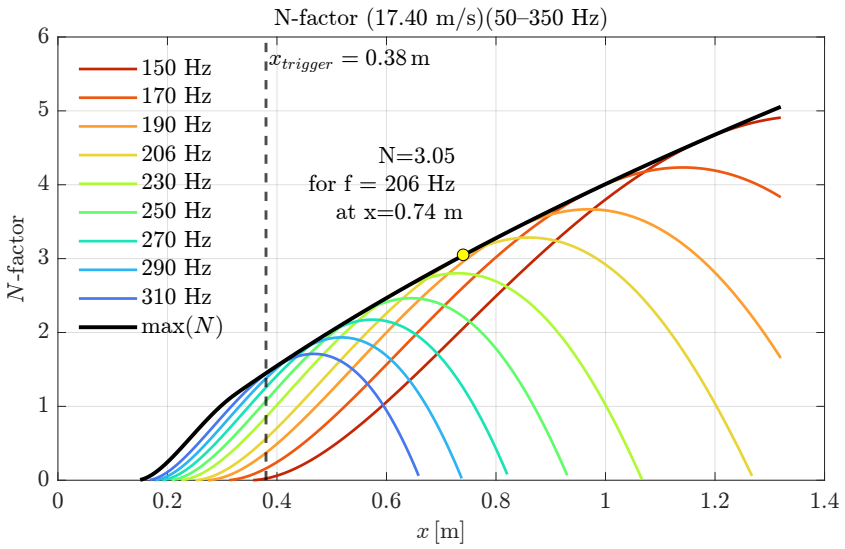

Figure 2.4: N factor curves from the OS solver for $U_\infty = 17.40$ m/s calculated for a frequency range of f=50 Hz to 350 Hz.

Amplitude selection:
To investigate the influence of the TS wave amplitude on the flow over the SERB, the amplitude of the forced TS wave was modulated by varying the peak-to-peak voltage supplied to the plasma actuator. An amplitude sweep between 5 $kV_{p\text{-}p}$ (kilovolts peak-to-peak) and 15 $kV_{p\text{-}p}$ was first performed to characterise the actuator response. During this sweep, the spectral amplitude of the microphone signals was monitored in the frequency domain, with particular attention given to the most upstream microphone (Mic 1), the one located immediately upstream of the FFS (Mic 8), and the most downstream one (Mic 14).

Trigger case	**Forcing level**	**Voltage range (kV_{p-p})**
T0	No forcing	0
T1	Low forcing	8–9
T2	Medium forcing	9–10
T3	High forcing	10–11

Table 2.2: Voltage range for each forcing level/plasma actuator trigger case

Three forcing levels were then selected such that the amplitude at microphone 1 remained approximately constant across cases, ensuring a comparable upstream disturbance level, and the amplitude at microphone 8 showed a clear, measurable difference between forcing levels. The lowest forcing level produced laminar flow at microphone 14, characterised by distinct tonal peaks and no broadband increase in spectral energy; while the highest forcing level resulted in intermittency at microphone 14, with sporadic broadband fluctuations in the time signal, indicating transition onset. These forcing levels, or trigger cases as they will be referred to going forward, are shown in Table 2.2, with T0 being assigned to the case with no forcing, i.e plasma actuator off.

2.1.5. Test-Matrix

Re	Geom case	No. of HWA measurement x locations	Trigger
1.5×10^6	G0 (clean)	15	T0
		15	T1
		15	T2
		15	T3
	G1 (bump)	15	T0
		15	T1
		15	T2
		15	T3

Table 2.3: Experimental Test Matrix

2.2. Wind tunnel and test section

This section describes the experimental facility in subsection 2.2.1, followed by a description of the flat-plate test section and its integration with the tunnel in subsection 2.2.2.

2.2.1. A-tunnel

The A-tunnel (Anechoic tunnel) is a state-of-the-art, open-jet, closed-circuit, vertical wind-tunnel located at the Low Speed Laboratory (LSL) at the Delft University of Technology, used for aeroacoustics research, as well as laminar-turbulent transition and active flow control studies. Starting from the bottom in Figure 2.5(a), (1) is the settling chamber with acoustic and thermal insulation on the walls preventing acoustic reflections in the range of 150 Hz to 20 kHz. At the top of this room, a rounded inlet with a 2:1 ratio ellipse- (2), holds the entire 3D printed contraction, with the inlet lip, flow straighteners, anti-turbulence screens and eventually the final converging nozzle, which leads to (3) the anechoic plenum of the tunnel where the outlet nozzle, test section and measurement equipment are housed. Finally (4) houses an acoustic foam block that directs the flow onto the recirculation channels, along with splitter silencers made of acoustic absorbing foam block (L in Figure 2.5(b)). The flow is accelerated through the tunnel by 2 engines with centrifugal fans (M in Figure 2.5(b)), with an expected blade passing frequency at maximum rotational speed of 500 Hz approximately, which is imperceptible at the test section according to Merino-Martínez et al. (2020).

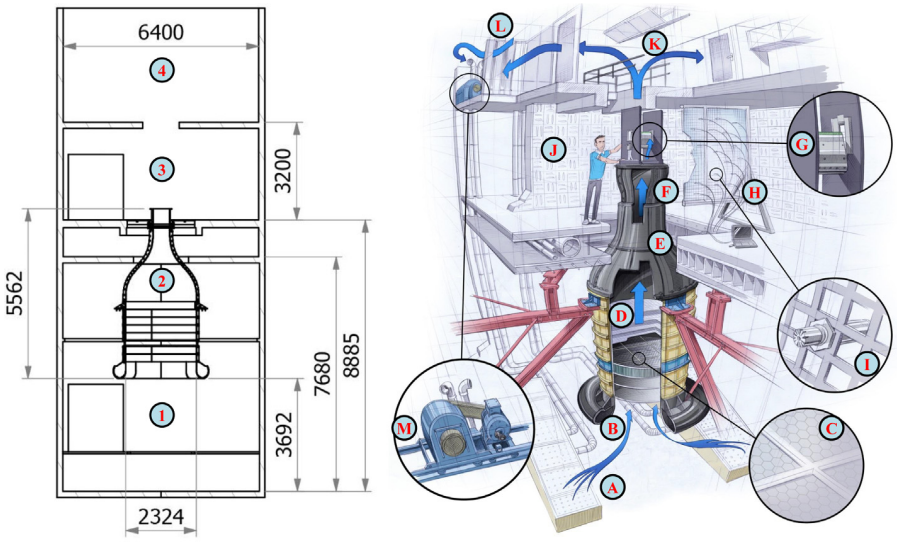

(a) (b)

Figure 2.5: (a) Side view of the A-tunnel facility (dimensions are in mm). (b) Artist impression of the A-tunnel facility (illustration by Stephan Timmers) from Merino-Martínez et al. (2020).

Figure 2.6a shows a picture of the outlet of the contraction that opens up into the anechoic plenum of the A-tunnel, with a contraction ratio of 15:1. An additional outlet nozzle (Delft 25 × 100) is fixed to the contraction outlet as shown in Figure 2.6b with the geometrical dimensions of the inner contour given in Table 2.4. The contraction ratio of this nozzle is given in Table 2.4 with reference to the contraction inlet (B in Figure 2.5(b)).

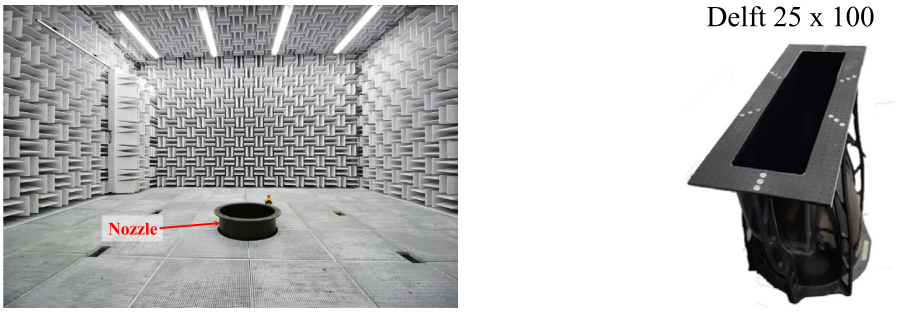

(a) **(b)**

Figure 2.6: (a) Picture of the anechoic plenum of the A-tunnel. (b) Nozzle used for current test from Merino-Martínez et al. (2020)

Name	Dimensions [m]	Height [m]	Contraction ratio	V_{max} [m/s]
Delft 25 × 100	0.25 × 1	1	17:1	40

Table 2.4: Geometry and characteristics of the nozzle used for these tests and its exit plane from Merino-Martínez et al. (2020).

The free-stream velocity was fixed at $U_\infty = 17.4\ \mathrm{m\,s^{-1}}$ to obtain a chord-based Reynolds number, $Re_c = U_\infty c/\nu_0 = 1.5 \times 10^6$ based on the flat-plate chord (measured from leading edge to trailing edge, excluding the adjustment flap), $c = 1.350\ m$. Ambient temperature and barometric pressure were monitored using a PT100 resistance temperature detector (RTD) and an NPA-201 pressure sensor, respectively. These measurements enabled continuous evaluation of the kinematic viscosity and ensured that the chord-based Reynolds number was maintained within ±1% over the course of the measurement day, despite variations in ambient conditions.

2.2.2. Test section

The test section consists of a flat plate, secured to an aluminium extrusion frame, enclosed with Poly (methyl methacrylate) (PMMA) walls as seen in Figure 2.7. This section will describe the configuration of the test section used, the flat plate, and some of the instrumentation on this test section.

1. Mechanical Integration with Wind Tunnel

The test section is secured to the tunnel by means of vertical supports from the floor of the plenum chamber and aligned vertically above the outlet nozzle (Figure 2.6b) through adjustment of the item beams.

The test section width is slightly narrower than the nozzle width to bleed the boundary layer from the side walls using elliptical leading-edge splitters. The upper and lower walls of the nozzle are aligned with those of the test section, with the interface between the two sealed using aluminium tape during wind-on conditions. The flow behind the flat plate is diverted away from the nozzle outlet to the plenum chamber by means of a splitter that extends the entire width of the test section (seen in Figure 2.7b) to minimise interference with the sensors and cables present on this side.

A door on the front side of the test section (visible in Figure 2.7a) allows access in order to change the HW probe, add/remove the bump, clean the plasma actuator, etc. The inclination of this door can be altered by two adjustment cranks at the top of the test section frame (seen in Figure 2.7a). This allows

adjustment of the cross-sectional area of the test section to maintain a zero pressure gradient at the chosen U_∞, even in the presence of boundary-layer growth on the flat plate and the test-section walls.

(a) **(b)**

Figure 2.7: (a) Front view of the test section mounted on the wind-tunnel nozzle. (b) Rear view of the test section

2. Flat-Plate Design
The flat plate made out of milled aluminium, with a length of 1.35 m from leading edge (LE) to trailing edge (TE), not including the trailing edge flap, which can be angled to adjust the stagnation point and LE pressure distribution.

The nose geometry of this flat plate test section was a modified Modified Super Ellipse (MSE) with an AR of 6 (Barahona, 2022). According to Lin et al. (1992), this geometry pushes the suction peak to the leading edge and reduces the adverse pressure gradient in the leading edge, allowing for less of a curvature discontinuity between the elliptical nose and the flat plate, and faster development to the Blasius BL solution.

Since the flat plate is mounted vertically over the outlet nozzle the coordinate system considered is as follows: the streamwise direction is considered to be x (x= 0 at the LE of the MSE nose, and positive in the direction of the TE of the flat plate); the plate normal direction is considered to be the y (y= 0 at the wall, positive away from the wall); and z is the spanwise direction of the plate (z= 0 at the midplane of the flat plate).

3. Insertion-Plate System and Surface Continuity
The flat-plate test section contains three slots designed to accommodate insertion plates. Any slots not used for securing test hardware were occupied by flat-milled aluminium insertion plates. The insertion plates were secured in the slots using an assembly of bolts, washers, and disc springs to allow for height adjustment. Flushness with the surrounding flat-plate surface was tested using a gauge block, where the insertion plate was said to be flush with the surrounding flat plate when the gauge block straddling both of these surfaces showed no noticeable rocking. Finally, the small gaps between the insertion plates and the slot edges were filled with plasticine to create a continuous, smooth surface.

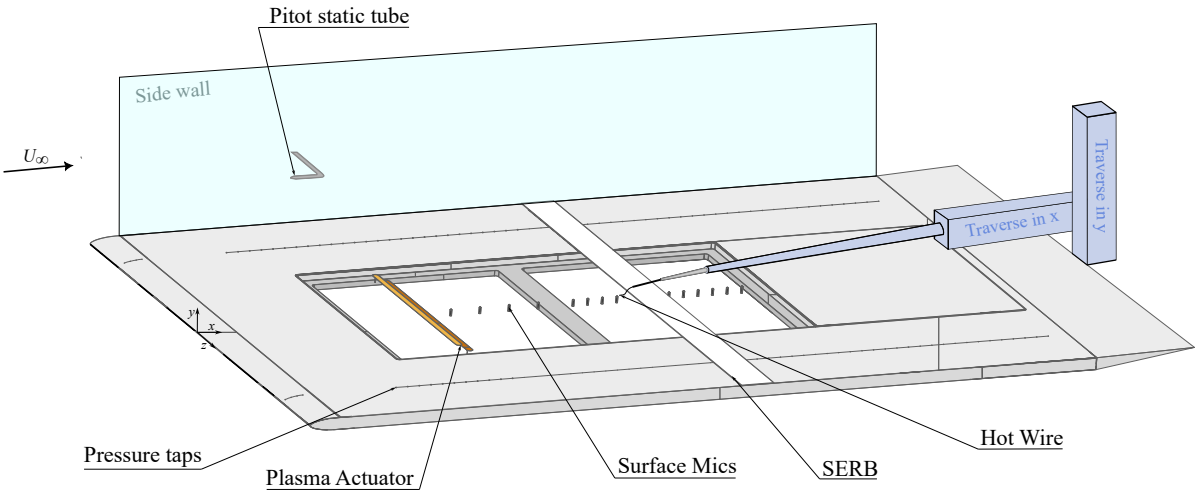

Figure 2.8: Diagram of experimental set-up consisting of the unswept flat plate with plasma actuator insertion plate, and SERB mounted, as well as the various flow measurement techniques used

4. Instrumentation Layout and Measurement Access
A two-degree-of-freedom (DoF) Zaber traverse system with a step resolution of 1 μm was used to move the HW in the streamwise and plate-normal directions (one traverse system for each degree of freedom). This traverse assembly was fixed to the top of the test section, on the item beam on the rear side of the flat plate (out of the flow). The sting carrying the HW probe was then fixed to this traverse assembly. The prongs of the single-component hot-wire probe were aligned using a laser level to ensure that the prong tips lay at the same streamwise location, thereby orienting the sensing wire correctly perpendicular to the freestream direction.

A pitot-static tube, fixed near the front of the test section and aligned in the streamwise direction, was used to monitor the dynamic pressure in the freestream. The readings from this pitot were used for hot-wire calibration as well as to maintain a constant Reynolds number throughout the test campaign. The 2 DoF traverse was fixed at the midplane of the plate did not allow for spanwise movement to the exact location of the pitot tube. Therefore, placing the hot wire at the same plate-normal height as the pitot tube, at the forwardmost streamwise position achievable by the traverse and sting, was deemed sufficient for calibration due to the zero pressure gradient and spanwise invariance over the flat plate.

2.3. Bump Setup

This section details the design and criticality assessment of the sharp-edged rectangular bump (SERB) used in the present study in subsection 2.3.1, followed by its construction and installation in subsection 2.3.2.

2.3.1. Bump Criticality

The criticality of the bump was mainly assessed based on the dimensions of the FFS of the SERB. The location of the FFS was considered to be the streamwise location where the excitation frequency was most amplified, as detailed in subsection 2.1.4. This also allowed for the in situ-determination of trigger frequency, also detailed in subsection 2.1.4, that was done using the surface-mounted mics shown in Figure 2.8. Conventionally, the BFS is chosen for this purpose as it has been shown to be more critical than the FFS. However, given the previously stated practical reasons, and the fact that the goal of this thesis is not to assess transition advancement/delay of the SERB, the criticality of the FFS will be assessed to determine the SERB height.

A summary of the relative step height (h/δ^*) vs step height-based Reynolds number ($Re_h = Uh/\nu$) examined in previous studies on TS-FFS interaction, under flow conditions comparable to the present work, namely, zero external pressure gradient and low Mach number (M$<$ 0.3), is shown in Figure 2.9 (Barahona, 2022). The shaded areas denote regions of the parameter space for which BL tripping at the step is reported.

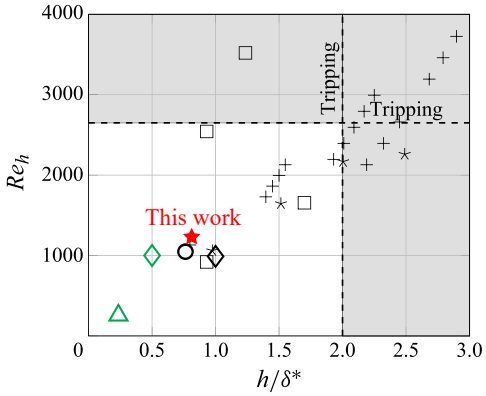

Figure 2.9: FFS configurations from previous works studying TS-FFS interaction, adapted from Barahona et al. (2025). Experimental works: Wang and Gaster (2005) (+), Perraud and Séraudie (2000) (∗), Barahona et al. (2025) (○), and present work (★). Numerical works: Edelmann (2014) (□), Teng (2023) (◇) and Worner et al. (2003) (△). Green symbols (e.g. ◇) represent step configurations for which transition delay or stabilisation has been identified under specific TS wave conditions.

In order for the FFS to be subcritical (transition not occurring at the FFS), the height had to be chosen to maintain the h/δ^* value within certain ranges of Re_h and h/δ^* as seen in Figure 2.9.

2.3.2. Bump construction and installation

The bump was laser-cut from 1 mm-thick PMMA and secured to the flat plate model using approximately 0.1 mm-thick double-sided tape, resulting in a cumulative height of 1.1 mm as an initial estimate for the preliminary design phase.

Based on initial calculations using the boundary layer solver (section 2.1), the boundary layer displacement thickness at the location of the FFS of the bump, x= 740 mm, would be 1.38 mm for the clean flat plate. With a step height of 1.1 mm, the resulting h/δ^* value for this bump is 0.7971. For the chosen U_∞= 17.4 m/s for a bump of this height, Re_h = 1220. According to Figure 2.9, would mean that the FFS of this bump would be firmly subcritical, within the regime where FFS-induced TS wave amplification is measurable but not dominant. This is close to the smallest step height tested by Wang and Gaster (2005), resulting in a $\Delta Re_{x_{tr}}$ ≈3.3% (Barahona et al., 2025).

As seen in subsection 1.4.3, Crouch and Kosorygin (2020) used an aspect ratio of $L : h = 50$, which is replicated in the present experiment to ensure that the streamwise bump length, L, is relatively large compared to the local boundary layer displacement thickness, and the effect FFS and BFS on the incoming TS wave can be analysed somewhat independantly. This results in a streamwise bump length of L= 55 mm, using the initial bump height estimate of h = 1.1 mm. The breadth of the bump spans the full width of the flat plate, as shown in Figure 2.8.

The position of the SERB was initially marked during the manufacturing of the insertion plate to ensure correct streamwise placement of the bump. Additionally, to accurately situate the bump when placing it on the flat plate, a laser level was used to confirm the horizontal installation of the bump, i.e on spanwise variation of x location of bump leading edge. As previously mentioned, the bump was fixed in place using double-sided tape, with additional aluminium tape at the ends of the span, as seen in Figure 2.7a to secure it during wind tunnel operation.

The height of the bump was characterised by using a laser scanner, as shown in Figure 2.10. Given the large streamwise length of the bump, L, the scanning was performed in 3 separate traverse sweeps to cover the FFS, upper surface and BFS of the SERB. Since the insertion plate and bump were made of PMMA, thin masking tape was applied to the locations where the bump was being measured to provide an opaque surface for the use of the laser scanner. Although this affects the scanned output in terms of surface smoothness, the characterisation of the height difference between the insertion plate and the bump is relatively unaffected.

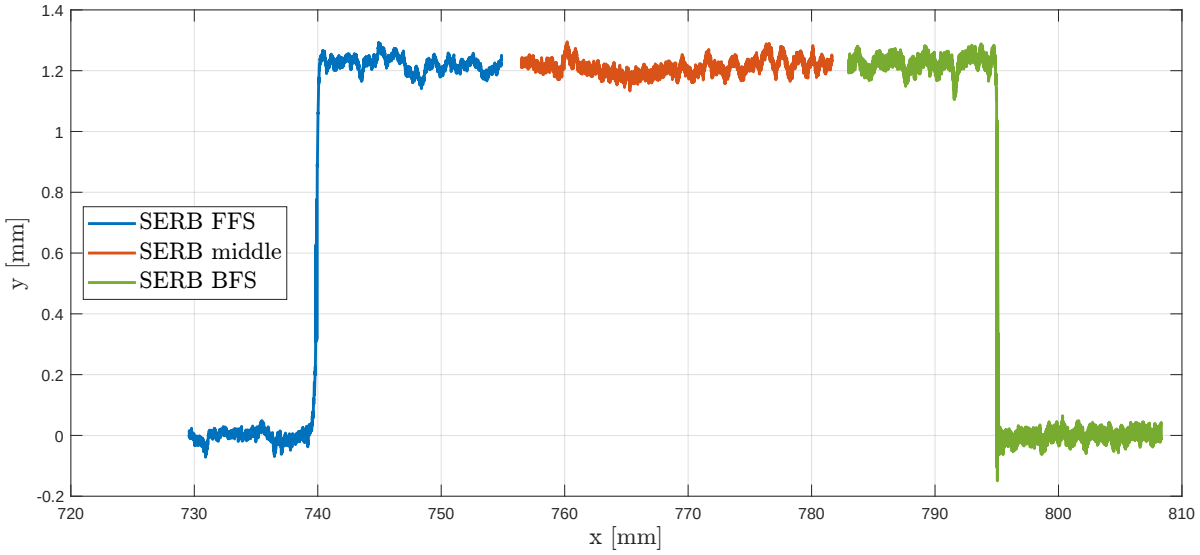

Figure 2.10: Laser scan of the FFS, middle and BFS of the SERB at the midplane

The profiles shown in Figure 2.10 are corrected to account for the inclination of the traverse system and remove outliers caused by light reflections at the surface discontinuities. First, the largest positive or negative value of Δy was found to indicate the streamwise location of the FFS and BFS. Since the surface upstream and downstream of the SERB were on the same plane, the global slope was found to be

$$m_{\text{glob}} = \tfrac{1}{2}(m_{upstream} + m_{downstream}).$$

This inclination is removed from every profile via

$$y_{\text{corr}}(x) = y(x) - m_{\text{glob}}\, x.$$

Ensuring that the surfaces remained mutually parallel. Then the outliers were removed by separating the surfaces before the FFS, over bump and after the FFS, and finding the median, y_{med} for each surface, only keeping the points that satisfy

$$y_{\text{corr}}(x) < y_{\text{med}} - \Delta y$$

where Δy is a small tolerance to separate unphysical measurements. Figure 2.10 shows the height of the bump to be ≈ 1.2 mm ($h/\delta^* = 0.869$). This differs from the initial assumption of a 1.1 mm ($h/\delta^* = 0.797$) bump height for the initial calculations, but this change is not significant for the present study, as this new h/δ^* value still places this bump within the subcritical range as discussed in subsection 2.3.1, meaning that no transition is expected at the FFS of the SERB.

2.4. DBD Plasma excitation of TS waves

This section provides background on the working principle of DBD plasma actuators. The mechanism by which the actuator excites TS waves is discussed in subsection 2.4.1, followed by the construction of the insertion plate used to integrate the plasma actuator and surface microphones into the flat-plate test section in subsection 2.4.2.

A dielectric barrier discharge (DBD) plasma actuator consists of two asymmetric electrodes separated by a thin dielectric layer and embedded flush with the aerodynamic surface (Moreau, 2007), as seen in Figure 2.11a. When an alternating high voltage is applied, a non-thermal surface discharge forms on the dielectric, producing a thin region of weakly ionised gas above the wall (Corke et al., 2010), shown in Figure 2.11b. The charged species generated in this plasma layer experience acceleration under the applied electric field and transfer momentum to the neutral air through collisions, resulting in a tangential body force localised close to the wall (Benard & Moreau, 2014). Because this mechanism does not rely on moving components or geometric protrusions, DBD actuators are well-suited for aerodynamic applications where minimal intrusion into the boundary layer is required (Moreau, 2007).

Extensive characterisation studies have shown that the induced forcing depends on applied voltage, actuation frequency, electrode shape and gap, and dielectric properties (Forte et al., 2007). Measurements of power consumption, discharge capacitance and light emission have further clarified how electrical input relates to plasma formation and actuator efficiency (Kriegseis et al., 2011). The coupling between discharge behaviour and flow response has also been documented through simultaneous electrical and aerodynamic measurements, enabling improved interpretation of actuator performance (Benard & Moreau, 2014). A detailed overview of diagnostics used to quantify the discharge characteristics and the induced near-wall body force is provided in Kotsonis (2015). Finally, recent reviews summarise the state of the art in DBD-based boundary-layer flow control and outline pathways toward practical applications in aeronautics (Kriegseis et al., 2016).

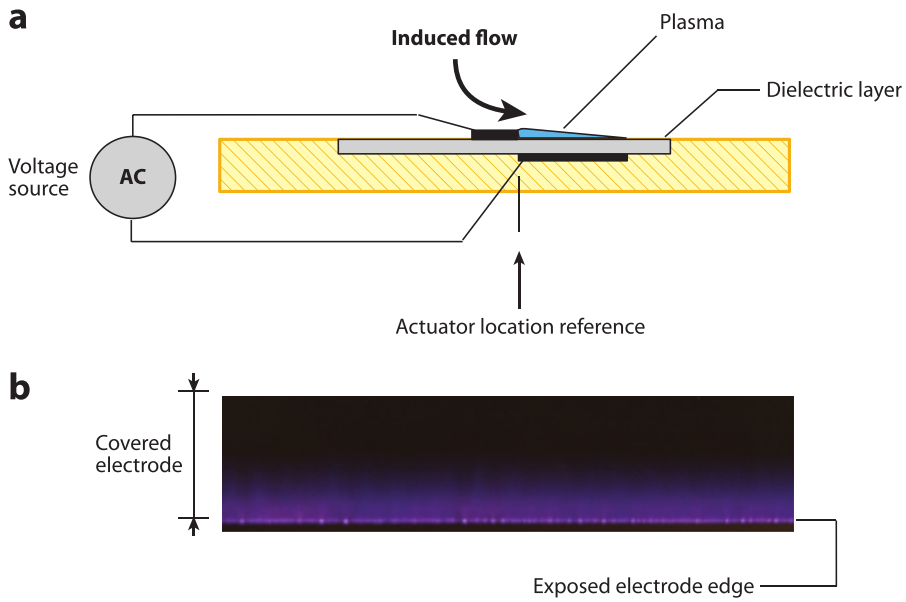

Figure 2.11: (a) Schematic drawing of a single DBD plasma actuator and (b) Ionised air over the covered electrode of a DBD plasma actuator during actuation. Reproduced from Corke et al. (2010)

2.4.1. Generation of Tollmien-Schlichting Waves

Time-periodic forcing applied near the wall interacts directly with the instability modes of a laminar boundary layer, making DBD actuators effective tools for exciting TS waves (Duchmann et al., 2010). Because the actuator's body force is confined to the region where TS waves exhibit maximum amplitude, even small-amplitude periodic forcing can generate a measurable instability wave that propagates downstream (Kotsonis et al., 2010). The frequency content of the disturbance is determined almost entirely by the applied voltage signal, enabling the actuator to produce controlled disturbances with prescribed temporal characteristics (Corke et al., 2010).

Experiments have demonstrated that DBD actuators can be used to either amplify or attenuate TS waves, depending on the phase relation and amplitude of the applied forcing relative to the incoming instability wave packet (Kotsonis et al., 2015). By driving the actuator with a sinusoidal voltage at a frequency within the unstable TS band, a nearly monochromatic disturbance can be imposed on the boundary layer (Duchmann et al., 2010). Adjusting the peak-to-peak voltage modifies the disturbance amplitude, enabling systematic investigation of finite-amplitude effects and comparison with linear-stability predictions (Kotsonis et al., 2010).

In the present study, TS waves were generated using a single surface DBD actuator driven by a sinusoidal waveform at a fixed frequency selected based on the expected TS amplification curve (Figure 2.4). Three forcing levels were implemented by varying only the peak-to-peak voltage, producing disturbances of identical frequency but different amplitudes. This approach follows established experimental methodologies for controlled TS wave excitation using surface DBD actuation. (Duchmann et al., 2010; Kotsonis et al., 2010, 2015).

2.4.2. Insertion plate construction

The insertion plate consisted of 2 PMMA plates layers on top of one another:
The first was a rectangular base plate with dimensions 719 mm x 399 mm with a height of 8 mm. M4 holes were tapped along the periphery to secure it to the flat plate test section. Fourteen ø6.1 mm microphone cavities were drilled into this base plate along the centerline of the plate as seen in Figure 2.12. Holes were also made in this base plate to accommodate the connection pins for the plasma actuator. The ends of the ground electrode for the plasma actuator were rounded off to prevent charge accumulation resulting from sharp edges, and then attached to this base plate, ensuring no air bubbles were trapped on application that would ionise to plasma during operation. Kapton tape was placed over this ground electrode to ensure no air would be trapped next to it.

The top plate had a height of 1 mm with the same length and breadth as the base plate, and was bonded to the base plate using a spray-on adhesive. The high voltage electrode, which would be exposed to the flow, was then fabricated and attached to the surface of this top plate, staggered from the ground electrode, as seen in Figure 2.12, with the same application precautions as the ground electrode were taken to prevent charge accumulation. ø1.2 mm connection pins, also rounded off for the same reason, were then soldered onto these electrodes.

Once this insertion plate was secured to the flat plate, these electrodes would be located 25 mm from the edge of the slot edge of the flat plate test section; a sufficient offset to reduce the likelihood of arcing from these pins to the surrounding aluminium flat plate during operation.

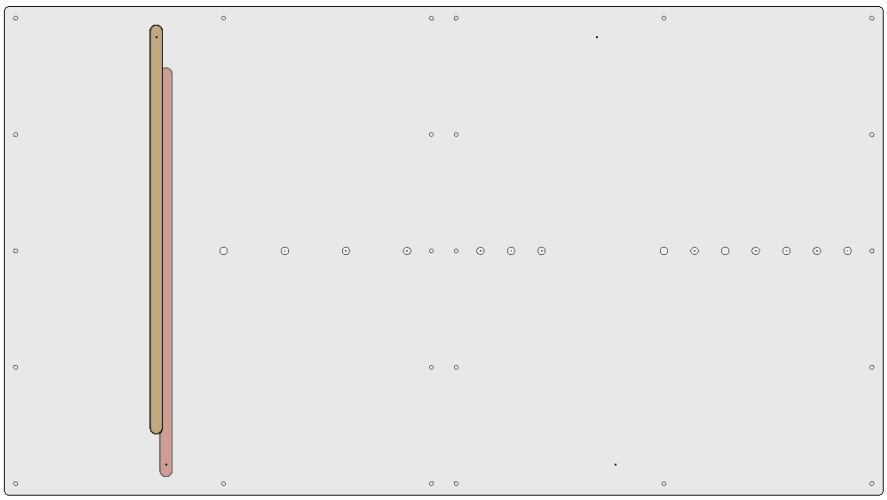

Figure 2.12: CAD model of the insertion plate with DBD plasma actuator, mounting holes and mic cavities

These two layers were then cleaned with ethanol and bonded using a spray adhesive with the connection pins from the top plate guided through the holes on the base plate to ensure alignment between the two layers.

Once these two layers were bonded, ø0.4 mm pressure tap holes were drilled into the top plate, aligned with the microphone cavities on the base plate. Mics were then placed into these cavities with the diaphragm up to the surface of the top plate, and aligned with the pressure tap holes. The microphone's leads (Drain, Source, Ground) were wired to shielded 3.5 mm jack cables, which were then connected to a data acquisition box, allowing the microphone signals to be recorded digitally. The rear volumes of the microphone cavities were sealed using Plasticine to eliminate acoustic leakage. The effectiveness of the sealing was assessed by directing pressurised air toward the sealed regions and observing the corresponding microphone output, with the absence of measurable signal variation taken as confirmation of adequate sealing.

The microphone signal cables were electrically shielded and physically routed away from the high-voltage supply lines feeding the plasma actuator (red cable in Figure 2.7b) in order to reduce electromagnetic interference and prevent contamination of the acoustic measurements by electrically induced noise.

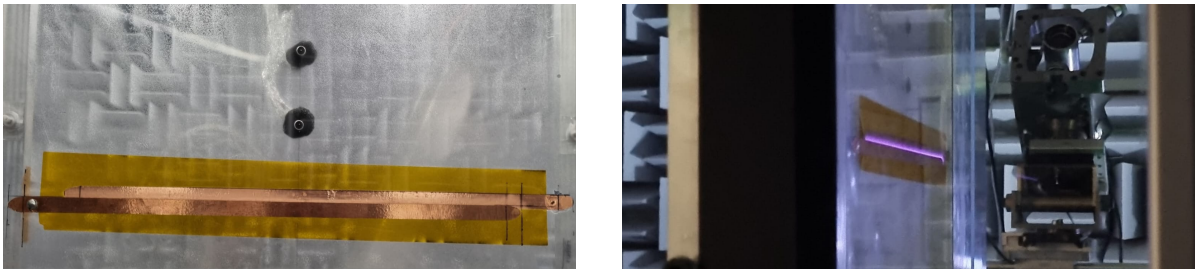

(a) (b)

Figure 2.13: (a) Electrodes of the plasma actuator, with initial microphones visible. (b) Uniform blue plasma created when the plasma actuator is active.

2.5. Flow Measurement Techniques

This section describes the measurement techniques used to characterise the boundary-layer flow and the disturbance field generated during the experiments. The operating principle and implementation of hot-wire anemometry used to resolve the boundary-layer velocity field are presented in subsection 2.5.1, followed by a description of the surface microphones used to monitor pressure fluctuations in subsection 2.5.2. The spatial arrangement of the microphones and hot-wire measurement locations is then detailed in subsection 2.5.3. Additional instrumentation used to monitor the freestream conditions and pressure environment of the test section is described in subsection 2.5.4 and subsection 2.5.5. Finally, the use of infrared thermography as a qualitative method for monitoring boundary-layer transition is discussed in subsection 2.5.6.

2.5.1. Hot Wire Anemometry

Hot-wire anemometry (HWA) is a measurement technique used to resolve fluid velocity with very high temporal and spatial resolution by exploiting the dependence of convective heat transfer on flow speed. The method is based on monitoring the rate of heat loss from a thin electrically heated wire when it is placed in a moving fluid. As the local velocity increases, convective cooling of the wire intensifies, altering its temperature and electrical resistance. By measuring the electrical response required to compensate for this heat loss, the local flow velocity can be inferred (Bruun, 1995; Tropea et al., 2007).

Constant Temperature Hot-Wire Anemometry:
In the present study, the hot wire was operated in constant-temperature anemometry (CTA) mode. In a CTA system, the wire forms one arm of a Wheatstone bridge and is maintained at an approximately constant temperature by a high-bandwidth electronic feedback circuit. Any change in convective heat loss caused by a velocity fluctuation leads to a change in wire resistance, which unbalances the bridge. The feedback amplifier responds by adjusting the bridge voltage such that the wire resistance—and hence its temperature—is restored to its prescribed operating value. The instantaneous bridge voltage required to maintain this thermal equilibrium constitutes the CTA output signal and provides a measure of the local flow velocity (Bruun, 1995; Tropea et al., 2007).

The relationship between the CTA output voltage and the flow velocity is commonly described using King's law, an empirical expression obtained from the steady heat balance of the wire,

$$E^2 = A + BU^n, \tag{2.6}$$

where E is the bridge voltage, U is the local flow velocity, and A, B, and n are calibration constants. The exponent n typically lies between 0.45 and 0.55 for air flows, reflecting the velocity dependence of convective heat transfer from a slender cylinder (Bruun, 1995). As emphasised by Bearman (1984), King's law should be regarded as a practical calibration model rather than a fundamental physical law, and its validity must be established through careful calibration over the velocity range of interest.

A major advantage of CTA operation is its excellent frequency response. Because the wire temperature is actively regulated, the effective thermal time constant of the sensor is significantly reduced compared with constant-current operation, allowing the system to resolve small-amplitude, high-frequency velocity fluctuations. The achievable bandwidth depends on the wire diameter, wire length, operating overheat

ratio, and the tuning of the feedback electronics, but is generally sufficient for resolving the narrowband disturbances associated with TS waves in laminar boundary layers (Bruun, 1995; Tropea et al., 2007). This makes CTA particularly suitable for the present investigation, where the objective is to measure periodic instability waves rather than broadband turbulent fluctuations.

Accurate use of CTA requires careful velocity calibration of the hot-wire probe. Calibration is performed by exposing the wire to a series of known reference velocities, typically obtained from a low-turbulence calibration jet or a uniform free-stream region of the wind tunnel, and recording the corresponding bridge voltage. The resulting voltage–velocity relationship is then fitted using King's law or an equivalent empirical model. Bruun (1995) stresses that calibration should be carried out under flow conditions as close as possible to those encountered during the experiment, particularly with respect to ambient temperature and pressure, in order to minimise systematic errors. Furthermore, repeated calibrations before and after the measurements are recommended to detect wire contamination or drift in operating conditions, which can otherwise lead to bias errors in the inferred velocity (Bearman, 1984).

In the present experiments, a single-sensor hot-wire probe was used. A fundamental limitation of single-component HWA is that it measures only the magnitude of the velocity component normal to the wire, without directional information. In a nominally two-dimensional laminar boundary layer, this measurement is dominated by the streamwise velocity component, with only a small contribution from the wall-normal component. However, because flow reversal cannot be detected unambiguously with a single wire, regions of reversed flow—such as recirculation zones downstream of geometric discontinuities—cannot be identified directly from the mean velocity signal. In such cases, frequency-domain information and changes in spectral content are commonly used to infer the presence of reversed or separated flow, consistent with standard hot-wire practice (Bruun, 1995; Tropea et al., 2007).

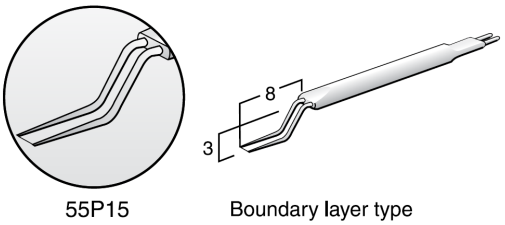

Figure 2.14: Dantec 55P15 probe

HWA measurements were performed using a Dantec Dynamics 55P15 single-sensor miniature boundary-layer probe (Figure 2.14). The sensing element consists of a platinum-plated tungsten wire of diameter $5\,\mu$m and length 1.25 mm, spanning the distance between a pair of offset support prongs, allowing the sensing element to be positioned close to the wall while keeping the probe body outside the boundary layer, thereby reducing flow disturbance and conductive heat losses to the support structure. This probe was mounted such that the sensing wire was oriented parallel to the spanwise (z) direction to measure the velocity in the (x, y) plane of the boundary layer consisting of a streamwise velocity component U_x, with a small contribution from the wall-normal component U_y for this 2-D flow.

The probe was connected to a TSI IFA300 constant-temperature anemometry (CTA) system.

At each measurement location, the hot-wire anemometer signal was sampled at a frequency of $f_s =$ 51.2 kHz over a period of $t = 3$ seconds .This resulted in

$$N = f_s \times t = 51{,}200 \times 3 = 153{,}600 \tag{2.7}$$

samples per height. The corresponding time resolution between samples was

$$\Delta t = \frac{1}{f_s} \approx 19.5\ \mu\text{s}, \tag{2.8}$$

which is orders of magnitude smaller than the characteristic time scales of the imposed TS waves (frequencies of $\mathcal{O}(10^2)$ Hz), and therefore more than sufficient to resolve their temporal evolution. The

sampling frequency sets the Nyquist limit at

$$f_N = \frac{f_s}{2} = 25.6 \text{ kHz}, \tag{2.9}$$

ensuring that all relevant fluctuation frequencies in the present boundary-layer flow, including the fundamental forcing tone and its higher harmonics, lie well below the aliasing limit. This sampling strategy provided adequate bandwidth for subsequent spectral analysis and digital filtering (Oppenheim & Schafer, 2014; Schlichting & Gersten, 2017).

Using the full set of 153,600 samples at each position allowed for statistically converged estimates of the mean velocity, RMS fluctuations. These statistics were used consistently across all measurement stations using identical acquisition parameters, ensuring comparability of the hot-wire data between cases.

2.5.2. Microphones

The microphones that were embedded in the surface were the 6 mm diameter POM-2739L-HD3-LW100-R, which is an omnidirectional microphone

2.5.3. Mics and HW measurement locations

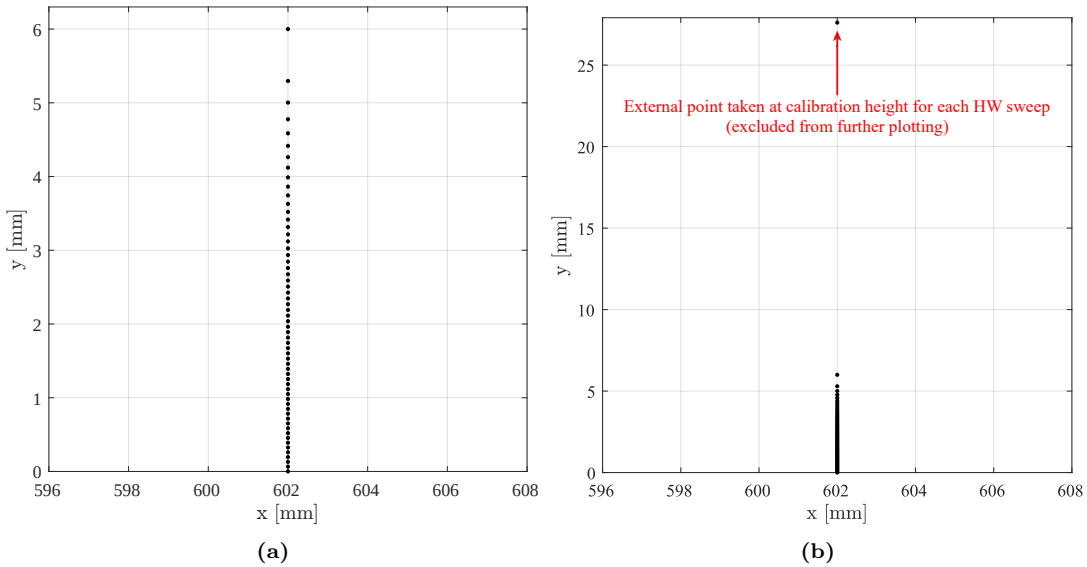

Figure 2.15: (a)Arcsine spacing of HW measurement points from the wall, (b) Addition of the extra point at calibration height.

60 measurement points were taken for the boundary layer sweep starting from the wall to 6 mm above the wall in the plate-normal direction. Initially, log spacing the points in the HW sweep was planned, but this resulted in a clustering of points near the wall (60 pts within 6 mm), requiring finer spatial resolution (below 1 μm) than was possible with the traverse system. Thus, arcsine spacing was used instead, as shown in Figure 2.15a. One additional point in the freestream at the calibration height, as seen in Figure 2.15b, was taken after these 60 points for each BL sweep. This was done to correlate velocities at each sweep location to the calibration height. However, going forward, the outermost point is excluded from further plotting routines.

It was important to capture BL information further upstream, away from the influence of the FFS of the bump, and so, the first sweep, P1, was placed at 602 mm as shown in Figure 2.16. More importantly for this research, the HW sweeps needed to capture boundary layer information before the FFS of the bump, over the bump, and after the BFS of the bump and thus 14 more sweep locations were placed to cover these positions with equally spaced sweeps from P2 at 700 mm to P15 at 830 mm, in steps of 10 mm. The BL sweeps over the bump retained the same distribution of points, but now offset by the

bump height as seen in Figure 2.16b. The HW station, P6, was chosen to be exactly over the location of the FFS at 740 mm. Thus, a 1 mm offset was given to this point (741 mm) for the clean case (shown in Figure 2.16a), so that the sweep at that point for the bump would be at the same x location. However, this P6 sweep location had to be further offset by 1 mm (placing it at 742mm) for the bump case (shown in Figure 2.16b), to make sure that the prongs of the HW did not extend past the top edge of the FFS of the bump.

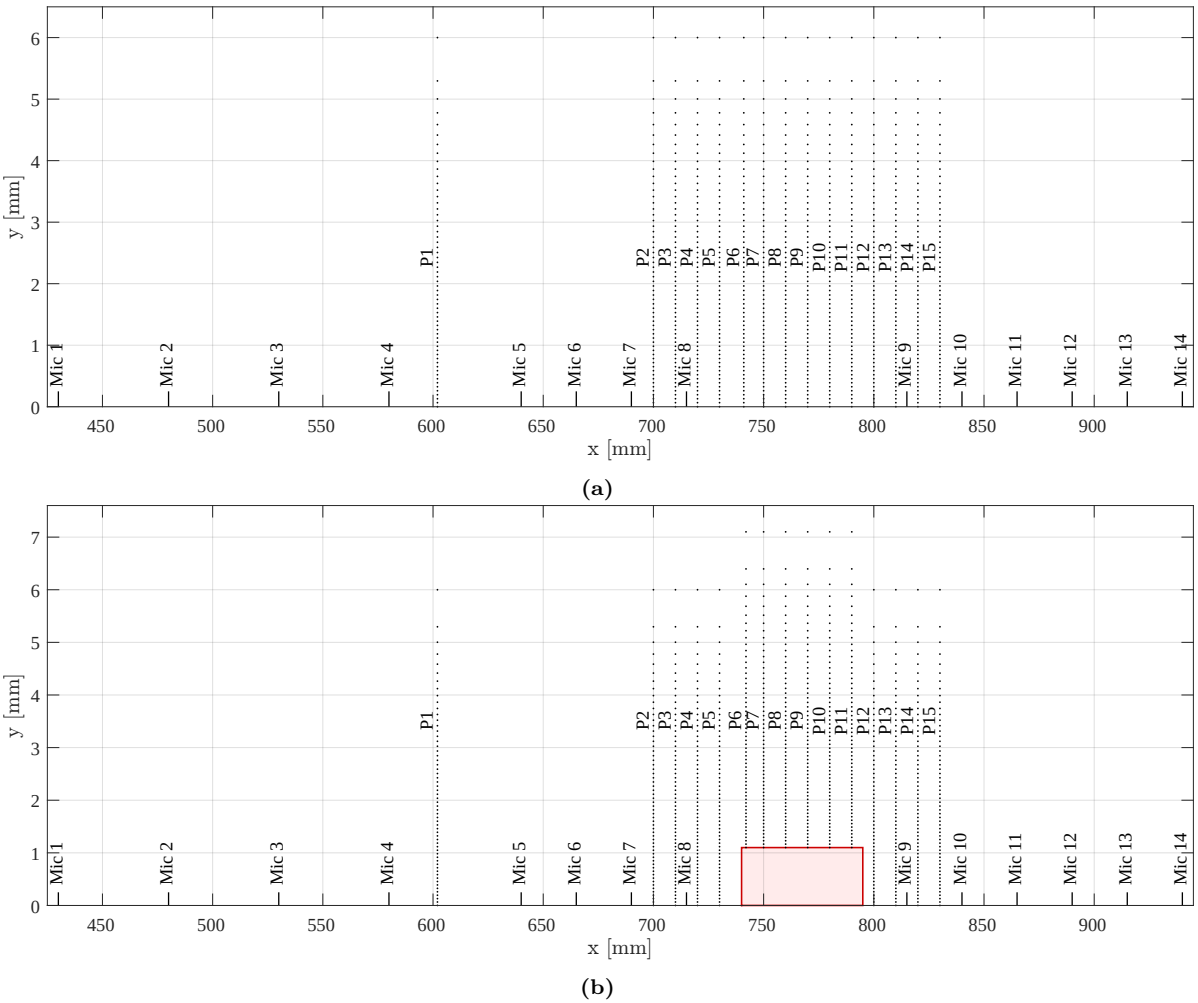

(a)

(b)

Figure 2.16: Mic, and HW sweep locations for the (a) clean (G0) case, and (b) bump (G1) case .

Microphones		**Hot-wire**	
Label	x **[mm]**	**Label**	x **[mm]**
Mic 1	430	P1	602
Mic 2	480	P2	700
Mic 3	530	P3	710
Mic 4	580	P4	720
Mic 5	640	P5	730
Mic 6	665	P6	741 (G0), 742 (G1)
Mic 7	690	P7	750
Mic 8	715	P8	760
Mic 9	815	P9	770
Mic 10	840	P10	780
Mic 11	865	P11	790
Mic 12	890	P12	800
Mic 13	915	P13	810
Mic 14	940	P14	820
		P15	830

Table 2.5: Streamwise locations of microphones and hot-wire (HW) sweep stations.

The x locations for all the HW sweeps, as well as the mic locations, are given in Table 2.5. The positioning of the mics and boundary layer sweep locations was done based on constrainsts of the setup, while still being evenly spaced to capture wave growth upstream and downstream of the bump, especially covering regions where hot wire data wasn't present. These mics were used for monitoring athe mplitude and frequency of the surface pressure fluctuations of the TS wave triggered by the plasma actuator. Since the plasma actuator was placed at a streamwise location of 380mm, 4 mics were equally spaced between the actuator and the first structural crossbar element of the test section. Then, after this crossbar, 4 mics were spaced evenly up to the FFS of the bump. Five more mics were then placed downstream of the BFS, up to the end of the insertion plate. As the insertion plate was not removed (bump secured on top of the insertion plate), the position of these mics, seen in Figure 2.16, remained unchanged throughout the experiment.

2.5.4. Freestream Pitot tube

Freestream velocity was captured using a pitot-static tube located on the side of the wind tunnel wall in the free stream. Pitot static tubes measure the dynamic pressure at the probe by measuring the difference between the total pressure and the static pressure at the location of the pitot tube. From the dynamic pressure, the freestream velocity is measured as

$$U_\infty = \sqrt{\frac{2\left(p_0 - p_\infty\right)}{\rho}}, \tag{2.10}$$

where p_0 is the total pressure and p_∞ is the static pressure at the pitot tube.

2.5.5. Static pressure measurement

Surface pressure measurements along the flat plate were collected through surface pressure taps, which consist of small orifices perpendicular to, and flush with the wall, routed through a cavity on the rear side of the test section and connected to an external pressure transducer to be monitored on the A-tunnel computer. This arrangement allows for the measurement of the static pressure at the wall without significantly disturbing the external flow.

124 surface pressure taps (62 on either side of the flat plate as seen in Figure 2.7, with 57 pressure taps on the flat plate and 5 on the MSE nose) at a distance of 110 mm from the lateral walls. This allows for the detection of streamwise pressure gradients. These pressure taps are also staggered in the x direction, between the left and right sides of the plate, to allow for spanwise pressure comparison and provide greater streamwise fidelity.

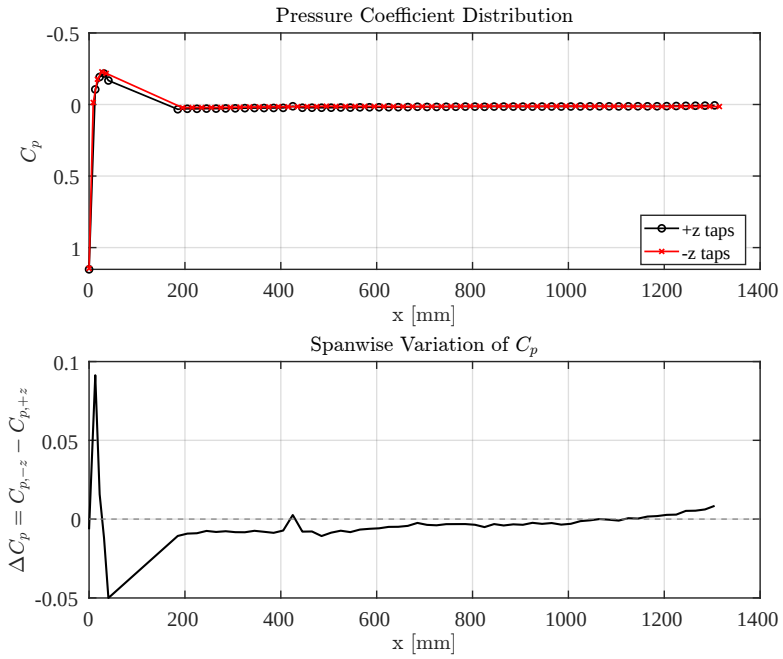

Figure 2.17: Pressure variation across the clean flat plate test section at $U_\infty = 17.4$ m/s, based on surface pressure taps

Figure 2.17 shows that there is little variation over the streamwise extent of the flat-plate region downstream of the nose, indicating nearly constant external pressure. The pressure coefficient was defined as

$$C_p = \frac{p - p_\infty}{\frac{1}{2}\rho_\infty U_\infty^2}, \tag{2.11}$$

where p is the measured static pressure at the pressure tap, p_∞ the freestream static pressure at the pitot tube, ρ_∞ the freestream density measured in the tunnel, and U_∞ the freestream velocity. To quantify the streamwise pressure gradient, the acceleration parameter

$$K = \frac{\nu}{U_e^2}\frac{\mathrm{d}U_e}{\mathrm{d}x} \tag{2.12}$$

was evaluated, where ν is the kinematic viscosity,and edge velocity is found from Bernoulli's equation (incompressible flow) using $U_e = U_\infty\sqrt{1 - C_p}$.

Exluding the data from the pressure taps over the elliptical nose of the flat plate, the mean acceleration parameter was found to be $K = 8.3 \times 10^{-9}$, which is well below the commonly accepted threshold for significant pressure-gradient effects ($K = 1 \times 10^{-8}$ from Schultz and Flack (2007)), confirming that the boundary layer develops under near ZPG conditions.

2.5.6. Infrared Thermography

Infrared thermography (IRT) is a non-intrusive technique commonly used to visualise boundary-layer transition by detecting changes in surface temperature. When the surface is heated, a laminar boundary layer transports heat away from the wall primarily through molecular diffusion, as the flow in this region is characterised by low wall shear and minimal wall-normal mixing. This limited transport leads to a relatively shallow temperature gradient at the wall, so the surface retains more of the imposed heat and appears warmer in an infrared image. In contrast, a turbulent boundary layer exhibits much higher wall shear and contains fluctuations and eddies that promote vigorous wall-normal exchange of momentum and thermal energy. This enhanced mixing steepens the near-wall temperature gradient and generates a substantially larger convective heat flux, causing the surface to cool more rapidly under the same heating conditions. The abrupt increase in both wall shear stress and heat-transfer coefficient as the flow transitions from laminar to turbulent produces a distinct temperature contrast, enabling the transition location to be clearly visualised using infrared thermography.

In the present experiment, IRT was employed solely as a qualitative diagnostic to monitor for transition over the flat plate. The plate was heated from the rear using halogen lamps, and an infrared camera mounted above the test section captured the entire flow-exposed surface within its field of view. Because the aim of this study was not to measure transition location with high precision, no quantitative processing (such as geometric dewarping or image-based heat-flux estimation) was required, and no structural modifications—such as cutting optical ports into the Perspex walls—were necessary.

Using this qualitative IRT method, a wedge-shaped turbulent wake was observed behind a solder puddle on the upper electrode of the plasma actuator. This feature indicated premature local transition and was eliminated by reshaping the solder puddle until the wedge pattern disappeared. IRT also confirmed that, for the selected Reynolds number ($Re = 1.5 \times 10^6$), the SERB did not trigger full transition for any of the forcing cases. Although some intermittency was visible near the last microphone at the highest forcing amplitude, the boundary layer remained largely laminar over the length of the insertion plate for all trigger conditions.

2.6. Corrections

This section describes the corrections applied to the raw measurement signals prior to spectral analysis and interpretation. Plasma-induced electromagnetic interference (EMI) arising from the high-voltage actuation system was removed using a wind-off reference subtraction method, described in subsection 2.6.1. The calibration procedure used to convert microphone voltage signals to acoustic pressure is presented in subsection 2.6.2. Finally, the correction applied to determine the physical wall location in the hot-wire boundary-layer measurements is described in subsection 2.6.3.

2.6.1. Plasma-Induced Electromagnetic Interference Subtraction

AC DBD plasma actuators produce periodic voltage and discharge-current signals at the actuation frequency and its harmonics (Benard & Moreau, 2014; Corke et al., 2010; Forte et al., 2007). This behaviour is inherent to the operation of surface DBD plasma actuators and is associated with the repeated processes of charge deposition, dielectric relaxation, and filamentary discharge (Moreau, 2007).

The high driving voltages and voltage slew rates can lead to electromagnetic coupling with nearby measurement electronics, including CTA systems. This coupling introduces narrowband spectral peaks at integer multiples of the forcing frequency, which are electrical artefacts rather than flow-induced fluctuations.

Background electromagnetic interference (EMI) was also observed during the experimental campaign, most prominently in the microphone measurements. This is illustrated in Figure 2.18, which shows the power spectral density (PSD) of the microphone signals under wind-off conditions with the plasma actuator switched off and on. This figure shows the spectral peaks at 50 Hz and its harmonics (in increments of 100 Hz). These peaks likely originate from power grid interference (mains frequency = 50 Hz).

In addition, a narrowband peak is observed when the plasma actuator is active (plasma triggered at 290 Hz in Figure 2.18b), indicating either electromagnetic coupling or acoustic transmission of the actuator signal to the microphones. Since these features are present under wind-off conditions, they are not associated with boundary-layer disturbances and are treated as non-aerodynamic artefacts in the subsequent analysis.

To remove plasma-induced EMI, a wind-off reference template was constructed for both the hot-wire and microphone channels. For each sensor, wind-off recordings acquired with the plasma actuator ON and OFF were subtracted to obtain an EMI template $E(f)$ containing only plasma actuator-related spectral components. During wind-on measurements, the measured PSD was corrected by subtracting this wind-off reference spectrum associated with plasma actuation. The subtraction was applied only in narrow frequency bands centred on the triggered frequency and its harmonics, thus removing the actuator-induced spectral component while preserving the broadband flow-induced content. Since the reference spectrum was obtained under wind-off conditions, the resulting corrected spectra represent the aerodynamic response of the boundary layer without contamination from plasma-related electromagnetic interference.

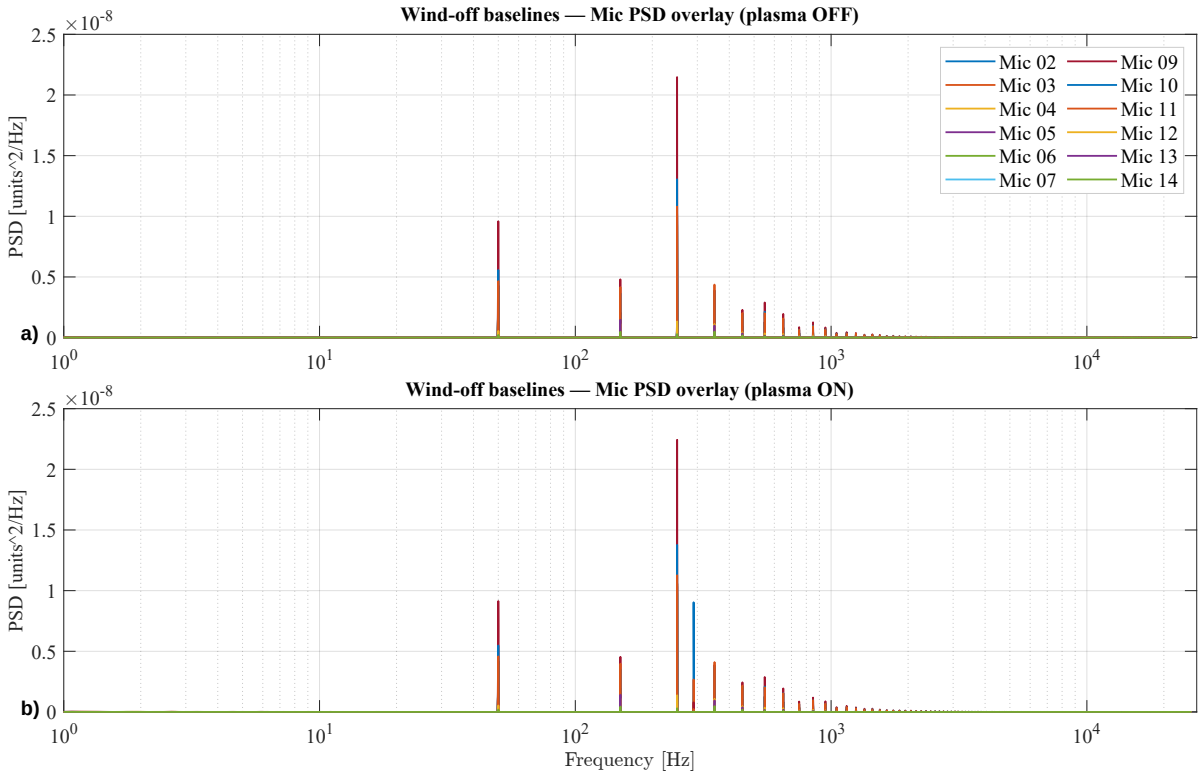

Figure 2.18: Baseline microphone measurements:(a) Wind-off, plasma actuator-off, (b) Wind-off, plasma actuator-on.

The subtraction was applied in the PSD domain using Welch-averaged spectra (Welch, 1967), rather than on individual Fourier amplitudes. This choice reflects standard practice in spectral analysis, where corrections are applied to statistically converged spectral estimates (Bendat & Piersol, 2010; Oppenheim & Schafer, 2014). After subtraction, the microphone PSDs were converted to sound pressure level (SPL) using the calibrated microphone sensitivities, while hot-wire spectra were retained in velocity-squared units. The corrected spectra were subsequently used for all modal, harmonic-content, and TS wave growth analyses.

2.6.2. Microphones calibration

The surface-pressure microphones were calibrated using a GRAS 42AA pistonphone, which generates a prescribed single-tone sound pressure level at a nominal frequency. For each microphone channel, the pistonphone was placed directly over the corresponding pressure tap using the supplied nozzle adapter, which acoustically isolated the microphone during calibration and ensured a repeatable calibration cavity.

The pistonphone provides a reference sound pressure level of $L_{\mathrm{cal}} = 114.01$ dB re 20 μPa at a nominal frequency of $f_{\mathrm{cal}} = 250$ Hz. The standard reference pressure is $p_0 = 20$ μPa and the corresponding reference RMS pressure amplitude is

$$p_{\mathrm{cal,rms}} = p_0\, 10^{L_{\mathrm{cal}}/20}. \tag{2.13}$$

For each microphone, a calibration time series $v(t)$ (in volts) was recorded while the pistonphone tone was applied. The voltage RMS associated with the calibration tone was obtained using a narrowband RMS estimate around f_{cal} (within a bandwidth of $\pm\Delta f$, with $\Delta f = 3$ Hz). Using the one-sided voltage power spectral density $S_{vv}(f)$, the narrowband voltage RMS was computed as

$$v_{\mathrm{cal,rms}} = \left(\int_{f_{\mathrm{cal}}-\Delta f}^{f_{\mathrm{cal}}+\Delta f} S_{vv}(f)\, \mathrm{d}f \right)^{1/2}. \tag{2.14}$$

The microphone sensitivity (for each channel) was then defined as

$$K = \frac{v_{\mathrm{cal,rms}}}{p_{\mathrm{cal,rms}}} \quad [\mathrm{V/Pa}], \tag{2.15}$$

which was was subsequently used to convert measured microphone voltages to acoustic pressure. In the frequency domain, the voltage spectrum at the pistonphone calibration frequency f_{cal} was extracted, and the corresponding pressure spectrum was obtained using

$$S_{pp}(f) = \frac{S_{vv}(f)}{K^2}, \tag{2.16}$$

where $S_{vv}(f)$ and $S_{pp}(f)$ denote the voltage and pressure power spectral densities, respectively.

The sound pressure level was then computed from the pressure spectrum using

$$L_p = 10 \log_{10} \left(\frac{p_{\mathrm{rms}}^2}{p_0^2} \right), \tag{2.17}$$

where $p_0 = 20$ μPa is the reference pressure.

2.6.3. HW wall correction using velocity profiles

For each streamwise (x) hot-wire measurement location, the wall was first located using a Taylor–Hubson micro-alignment telescope. Once visual confirmation was obtained by ensuring that the prongs of the hot-wire probe were in contact with the surface, the probe was withdrawn and subsequently advanced in small increments towards the wall until the measured velocity reached approximately $0.1\,U/U_e$. This provided a repeatable reference point for the onset of the near-wall region, from which the subsequent wall-finding correction based on the hot-wire velocity profile was applied.

In the raw hot-wire measurements, the mean velocity profile typically exhibits a shallow near-wall "tail", where the measured velocity remains artificially elevated instead of tending smoothly toward zero, as seen in the black line in Figure 2.19 for values close to y=0 mm. This behaviour arises from the combined influence of natural convection and, more significantly, thermal conduction from the heated wire to the surface when the probe is positioned close to the wall. As the wire approaches the solid boundary, part of its heat is conducted into the plate rather than being convected solely by the flow, reducing the wire's sensitivity to low velocities. The CTA feedback circuit therefore responds as if the local flow speed were higher than it truly is, yielding a non-zero apparent velocity even when the physical fluid velocity is very small. This effect renders the last few measurement points unreliable and prevents direct identification of the no-slip point from the raw signal, necessitating a post-processing correction to accurately locate the wall.

Because the clean flat-plate flow corresponds to a zero-pressure-gradient (ZPG) boundary layer, the streamwise pressure gradient satisfies $\partial p/\partial x = 0$, which implies $\partial^2 U/\partial y^2|_{y=0} = 0$ from the laminar boundary-layer equations. Consequently, the near-wall velocity variation is locally linear, making a linear least-squares fit appropriate for determining the wall position (Schlichting & Gersten, 2017; E. B. White & Ergin, 2004).

A fit window was then defined from a lower bound at the location of the near-wall maximum of the velocity curvature $|\partial^2 U/\partial y^2|$ (spike in the purple line in Figure 2.19), to an upper bound at the point where $U/U_e = 0.40$ (marked by the blue dashed line in Figure 2.19). This interval consistently captured the region of the profile where the velocity variation remained approximately linear while excluding points affected by conduction and natural convection near the wall. A straight line was fitted to this window, and its intercept with $U = 0$ was taken as the wall position. All raw wall-normal coordinates were corrected according to

$$y_{\mathrm{corr}} = y_{\mathrm{raw}} - y_{\mathrm{wall}}, \tag{2.18}$$

Ensuring that $y_{\mathrm{corr}} = 0$ coincides with the physical wall so that the profile satisfies the no-slip condition.

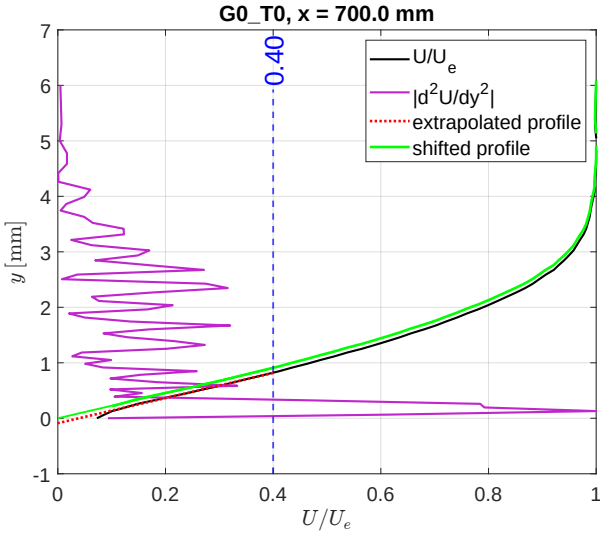

Figure 2.19: Height correction for the HW boundary layer profile for the x=700 mm station of the clean (G0), untriggered (T0) case

The wall-shift correction was applied only to the clean flat-plate configuration (G0) as the near-wall velocity profiles exhibit a monotonic laminar boundary-layer structure, with a locally linear behaviour in the viscous sublayer that permits the above method of wall extrapolation.

On the other hand, the SERB configuration (G1) is influenced by local geometric perturbations, leading to modified pressure gradients and altered near-wall shear distributions. At several streamwise stations, the velocity profiles exhibit pronounced curvature and, in some cases, non-monotonic behaviour in the near-wall region. Under such conditions, the above linear extrapolation towards the wall is not well-defined and may lead to biased wall-position estimates. Previous studies (Barahona, 2022) have addressed this difficulty by using reference DNS solutions to refine wall-location estimates in the presence of geometric perturbations. Since the current study did not include a reference solution for the present SERB geometry, no wall-shift correction was applied to the G1 configuration, thereby avoiding the introduction of additional modelling assumptions.

2.7. Data Processing

This section describes the signal-processing methods used to analyse the time-resolved hot-wire and microphone measurements. Fast Fourier Transform (FFT) are first introduced in subsection 2.7.1, followed by the estimation of power spectral densities using Welch's method in subsection 2.7.2.

2.7.1. Fast Fourier Transforms

The Discrete Fourier Transform (DFT) provides a mapping from the time domain to the frequency domain by projecting a sampled signal onto a set of orthogonal complex exponentials. For a discrete signal $x[n]$ of length N, the DFT is defined as

$$X[k] = \sum_{n=0}^{N-1} x[n]\, e^{-i2\pi kn/N}, \tag{2.19}$$

which decomposes the signal into its constituent frequency components. For laminar boundary-layer experiments, this decomposition enables identification of disturbance modes, such as TS waves, and any harmonics or subharmonics introduced by external forcing (e.g. plasma actuation).

Direct computation of the DFT requires $\mathcal{O}(N^2)$ operations, which becomes prohibitively expensive for long measurement records. The Fast Fourier Transform (FFT), (Cooley & Tukey, 1965), reduces this cost to $\mathcal{O}(N \log N)$ by exploiting symmetries in the DFT kernel. The FFT is therefore the standard numerical tool for spectral analysis in experimental fluid mechanics (Tropea et al., 2007). In the present study, FFTs were applied to all hot-wire and microphone signals as an initial diagnostic step to reveal

dominant disturbance frequencies, the fundamental plasma forcing tone, and higher-order harmonics prior to statistically converged PSD estimation.

2.7.2. Power Spectral Density Using Welch's Method

While FFTs allow inspection of the instantaneous frequency content, quantitative assessment of disturbance energy across frequencies requires a statistical estimator of the Power Spectral Density (PSD). The PSD describes how the variance of a stationary signal is distributed over frequency and is defined as the Fourier transform of the autocorrelation function (Bendat & Piersol, 2010). In laminar boundary-layer stability experiments, PSD estimates are particularly useful for extracting the amplitudes of TS waves, forced disturbances, and harmonic content associated with periodic excitation.

Welch's method (Welch, 1967) improves the statistical convergence of PSD estimates by dividing the signal into overlapping segments, applying a window function to reduce spectral leakage, computing FFTs of each windowed segment, and averaging the resulting periodograms. This process reduces estimator variance while maintaining a usable level of frequency resolution. For a segment length M and sampling frequency f_s, the corresponding frequency-bin width is

$$\Delta f = \frac{f_s}{M}, \tag{2.20}$$

which sets the narrowband resolution of the PSD and must be chosen with regard to the expected TS wave frequency band and the plasma forcing frequency.

Welch-averaged PSDs were used for all hot-wire and microphone measurements in this study. The method provides statistically converged estimates of the disturbance energy at the fundamental forcing tone, its harmonics, and the natural TS wave frequencies. Because PSD estimates are linear in the underlying second-order statistics, the PSD domain also provides a robust basis for removal of plasma-induced electromagnetic interference via template subtraction. The resulting PSD distributions allow precise tracking of disturbance amplification and modal development throughout the laminar boundary layer.

3

Results

This chapter presents the results obtained from the experimental measurements for both the clean flat-plate case (G0) and the SERB case (G1), with the aim of addressing the research questions stated in section 1.5. In particular, the chapter examines how the boundary-layer response to the SERB depends on the amplitude of the incoming forced TS wave, with emphasis on harmonic content (section 3.1), wall-normal disturbance structure (section 3.2), and downstream disturbance growth (section 3.3).

3.1. Harmonic Content

This section will examine the frequency content of the hot-wire measurements at each streamwise station for both the clean plate in subsection 3.1.1 and SERB cases in subsection 3.1.2. By analysing the FFT spectra across the wall-normal hot-wire sweeps, the evolution of the forced fundamental, its harmonics, and any additional spectral features can be compared as a function of streamwise location and forcing amplitude.

At each streamwise x station, a one-sided FFT amplitude spectrum is computed from the velocity time series at each discrete wall-normal height, y, of the HW boundary-layer sweep, resulting in an amplitude matrix $A(f, y; x)$ which is plotted as a spectrogram for each y of the boundary-layer profile on the y axis, and the entire frequency range up to the Nyquist frequency (25.6 kHz), shown on a log scale on the x axis. Because spectral amplitudes span a large dynamic range, the spectrograms are typically displayed in decibels via

$$Z(y, f; x) = 20 \log_{10}\big(A(f, y; x) + \varepsilon\big), \tag{3.1}$$

where ε is a small constant that prevents log(0); this conversion is for visualisation only and does not alter the underlying linear amplitudes. These spectrograms are presented below, comparing across different trigger cases, for the x stations of the HW measurements.

3.1.1. Clean case

In the clean case, the fundamental trigger frequency of 210 Hz appears as a narrow peak, highlighted using a lightened bar in the figures below. The 4 tiles refer to the 4 plasma trigger cases, with T0 = no triggering and T1 to T3 going from lowest to highest amplitude.

Figure 3.1, is the measurement taken at the most upstream HW boundary-layer sweep (refer Figure 2.15). In this figure and the following figures, low-frequency peaks (below ≈75 Hz) are assumed to be wind-tunnel/structural vibrations during wind-on conditions, as they exist for a low frequency range (≈ 10 to 60 Hz). These peaks are unlikely to be the influence of background EMI or plasma EMI as these were removed using the wind-off baselines, as detailed in section 2.6.

Figure 3.2 shows the row-normalised spectrogram for the T3 case at $x = 602$ mm (like in Figure 3.1), where the FFT amplitude at each wall-normal position is normalised by its local maximum. This representation highlights narrow-band tones that would otherwise be less visible against the broadband background. The imposed excitation appears as a sharp line at the trigger frequency $f_c = 210$ Hz.

In addition, discrete low-frequency peaks are observed at ≈ 20 Hz, with accompanying components at ≈ 10 Hz and ≈ 40 Hz, and a weaker contribution near ≈ 5 Hz. Rough estimates of the coupled bending dynamics of the traverse stepper motor assembly (approximated as a rectangular-section cantilever) and the attached hot-wire sting (approximated as a cylindrical-section cantilever), using representative steel properties and the measured cantilever dimensions, place the first bending mode in the $\mathcal{O}(10)$ Hz range, i.e. in the same ballpark as these peaks. The repeated appearance of this peak set therefore supports a structural interpretation, with the ≈ 20 Hz tone taken as the fundamental vibration, the ≈ 40 Hz peak as its first harmonic, and the ≈ 10 Hz and ≈ 5 Hz components interpreted as subharmonics. On this basis, the low-frequency tones in Figure 3.2 are attributed to vibration of the traverse/sting assembly rather than boundary-layer instability dynamics.

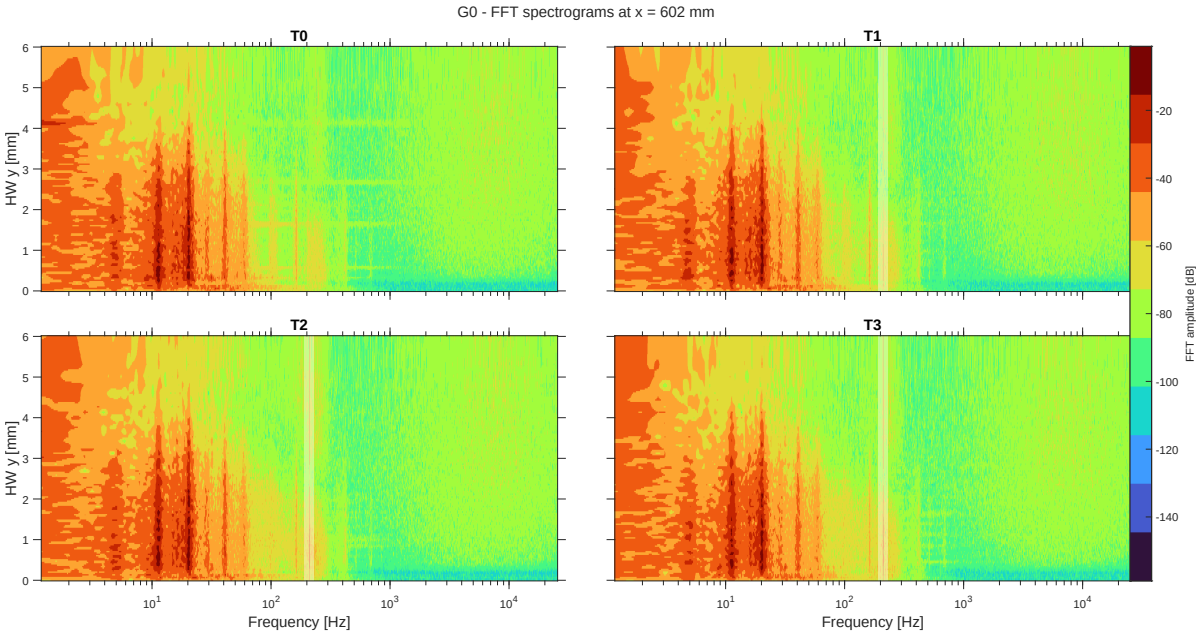

Figure 3.1: FFT spectrogram at streamwise station $x = 602$ mm for the clean case, G0.

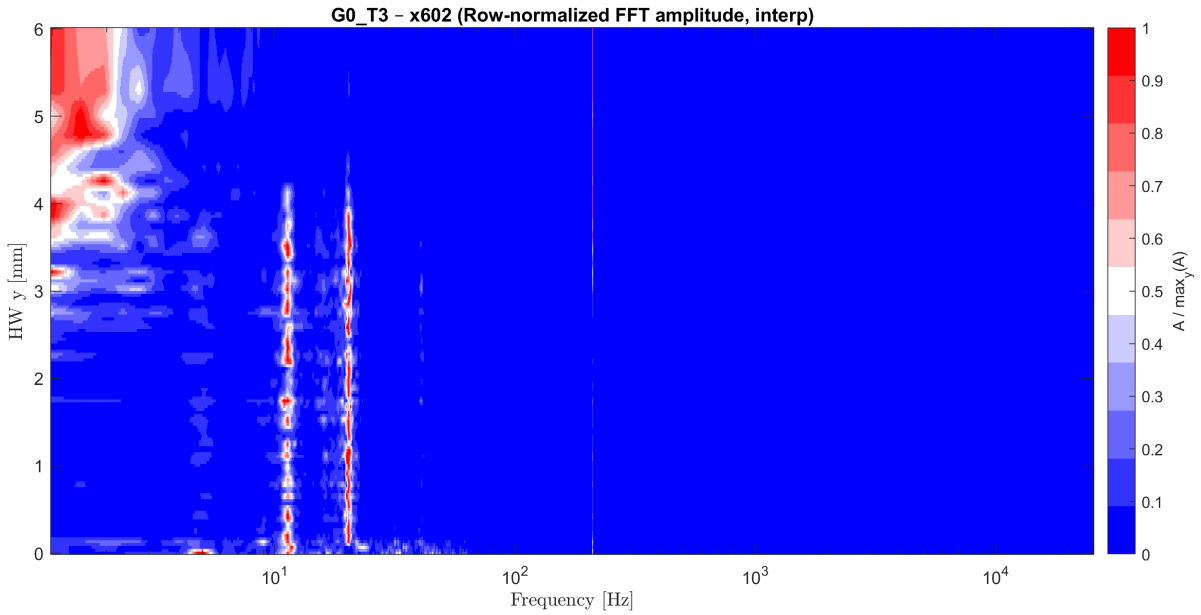

Figure 3.2: Normalised FFT amplitude at streamwise station $x = 602$ mm for the clean case, G0, Highest forcing amplitude, T3

Figure 3.3 is the measurement taken at the HW sweep location in the clean case corresponding to the FFS of the bump. The fundamental of the trigger frequency (f_c =210 Hz) peaks around this $x = 741$ mm station. In addition, spectral peaks at the harmonics $2f_c$ (420 Hz) and $3f_c$ (630 Hz) are also observed. These higher harmonics are also perceptible at downstream stations, as seen in Figure 3.4 at the $x = 820$ mm station, but do not exhibit systematic downstream growth. This suggests that the dominant instability dynamics at these stations are captured by the forced fundamental, with these harmonics introduced by the forcing rather than as evidence of distinct, growing higher-frequency TS modes.

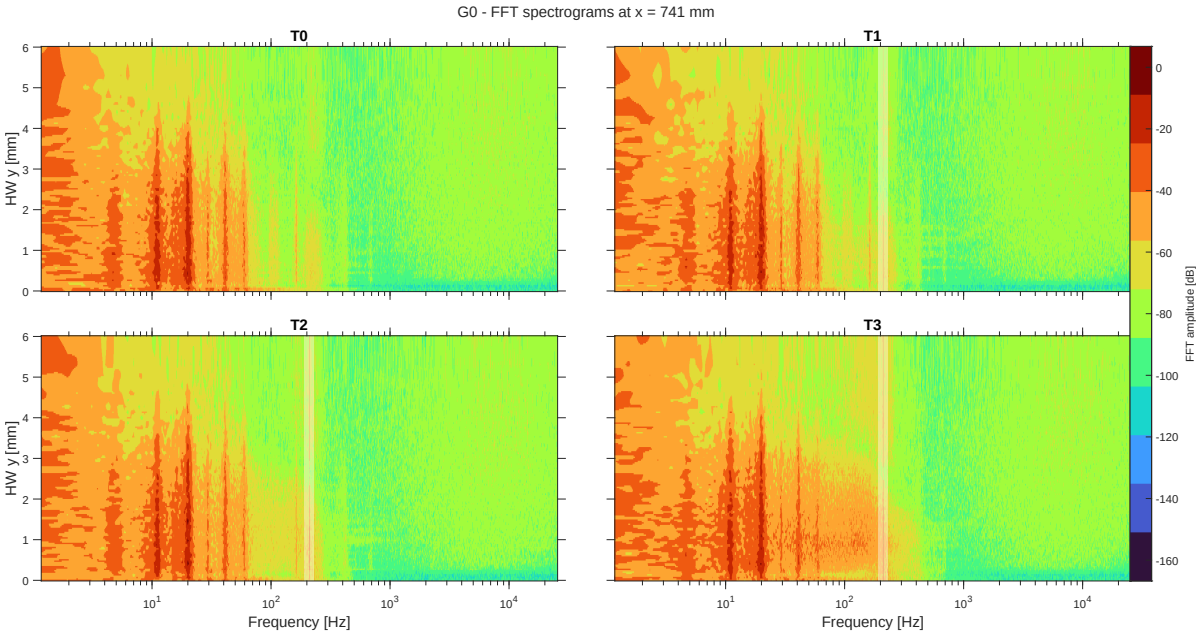

Figure 3.3: FFT spectrogram at streamwise station $x = 741$ mm for the clean case.

The low-frequency peaks in Figure 3.1, Figure 3.3, and Figure 3.4 form a narrow-band set centred around ≈ 20 Hz, with accompanying subharmonic/harmonic content at ≈ 10 Hz and ≈ 40 Hz, and a weaker component near ≈ 5 Hz. These tones are present for all trigger conditions and appear with comparable intensity at each of these x stations, suggesting a repeatable, structural (instrumentation-induced) origin, rather than a flow-instability feature. The peaks are most clearly observed within the boundary layer ($y \approx \delta_{99} \simeq 4$ mm at these stations, according to Figure 2.2). This wall-normal localisation is consistent with probe/support vibration: a small motion of the hot-wire produces an apparent velocity fluctuation that scales with the local mean shear, $u' \sim \eta(t)\,\partial U/\partial y$, so the response becomes weak in the freestream where $\partial U/\partial y \to 0$. Hence, these tones appear strongest inside the boundary layer because the mean shear is largest there, so any probe motion produces a larger apparent u', whereas in the freestream the same motion has little effect.

Additionally, when comparing the triggered cases between these figures at different streamwise stations, a general increase in the amplitude of the lower frequencies can be perceived, visualised as a spreading region of warmer colours, most clearly seen for the T3 case when moving from Figure 3.1 at $x = 602$ mm, to Figure 3.3 at $x = 741$ mm, and then Figure 3.4 at $x = 820$ mm. This general increase in the amplitude of the lower frequencies might be attributed to a spreading of energy between these frequencies when moving in the downstream direction, with the higher trigger cases having stronger actuator forcing and seeing greater mixing. This trigger amplitude-based mixing will become even more relevant in the following section.

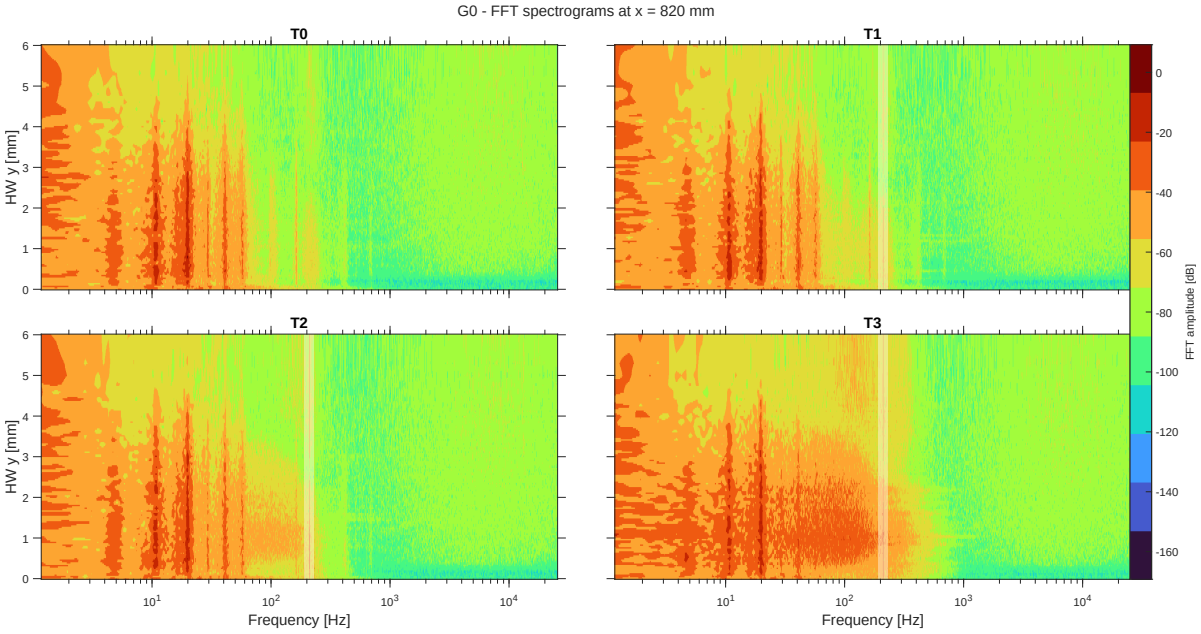

Figure 3.4: FFT spectrogram at streamwise station $x = 820$ for the clean case.

3.1.2. Bump Case

Figure 3.5, located at x= 700 mm (40 mm ahead of the SERB), shows that the x-stations far ahead of the FFS for the SERB case are spectrally similar to the clean case, with the previously noted low frequency peaks attributed to structural vibrations still being present, and the amplitude peaks due to the increased forcing amplitude from T0 to T3 are also observable. The supposed spreading of energy between frequencies that increases with greater forcing amplitude is also seen in Figure 3.5; most evident in the highest forcing case, T3.

The spectra in Figure 3.5 do, however, differ from the clean case in that there is a slight upward shift in wall-normal concentration of high energy, consistent with the mild boundary-layer thickening induced by the adverse pressure gradient approaching the FFS.

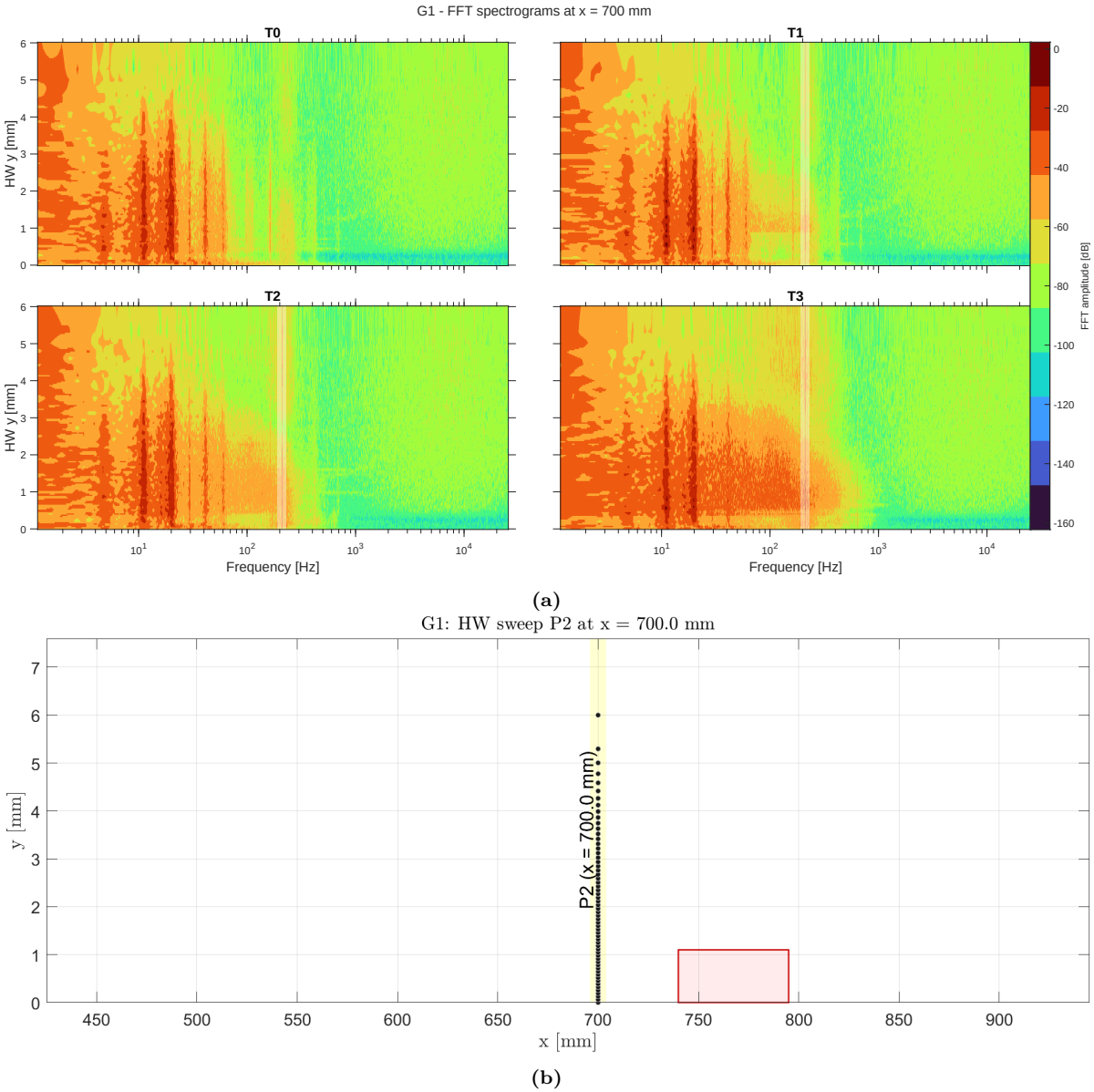

Figure 3.5: (a) FFT spectrogram at streamwise station $x = 700$ for the bump case. (b) HW sweep location for $x = 700$.

In the vicinity immediately upstream of the FFS, the boundary layer experiences a rapidly increasing adverse pressure gradient that generates the first near-wall recirculation region discussed in subsec-

tion 1.4.2. This produces a strong local enhancement of wall-normal shear, which is known to amplify TS modes in a purely modal manner (Barahona et al., 2025).

The spectrogram at x= 730 mm (10 mm ahead of the FF) in Figure 3.6 reflects this behaviour. All triggered cases exhibit a clear increase in the amplitude of the forced TS mode at $f_c = 210$ Hz (highlighted), consistent with the expectation that the APG-induced shear layer strengthens the modal growth rate of the incoming TS wave. A corresponding increase in the clarity and amplitude of the harmonics is also visible: the $3f_c$ harmonic strengthens for all forcing levels, and the $3f_c$ harmonic becomes distinct for T2 and T3.

Importantly, the high-frequency broadband content remains unchanged relative to upstream stations. The absence of broadband growth indicates that the recirculation region has not induced any inflectional instability or secondary instability, and that the amplification observed here corresponds strictly to the linear, modal growth expected for TS waves in adverse-pressure-gradient conditions. This behaviour matches the upstream evolution reported in Barahona et al. (2025), where the TS mode thickens and strengthens as the flow approaches the step.

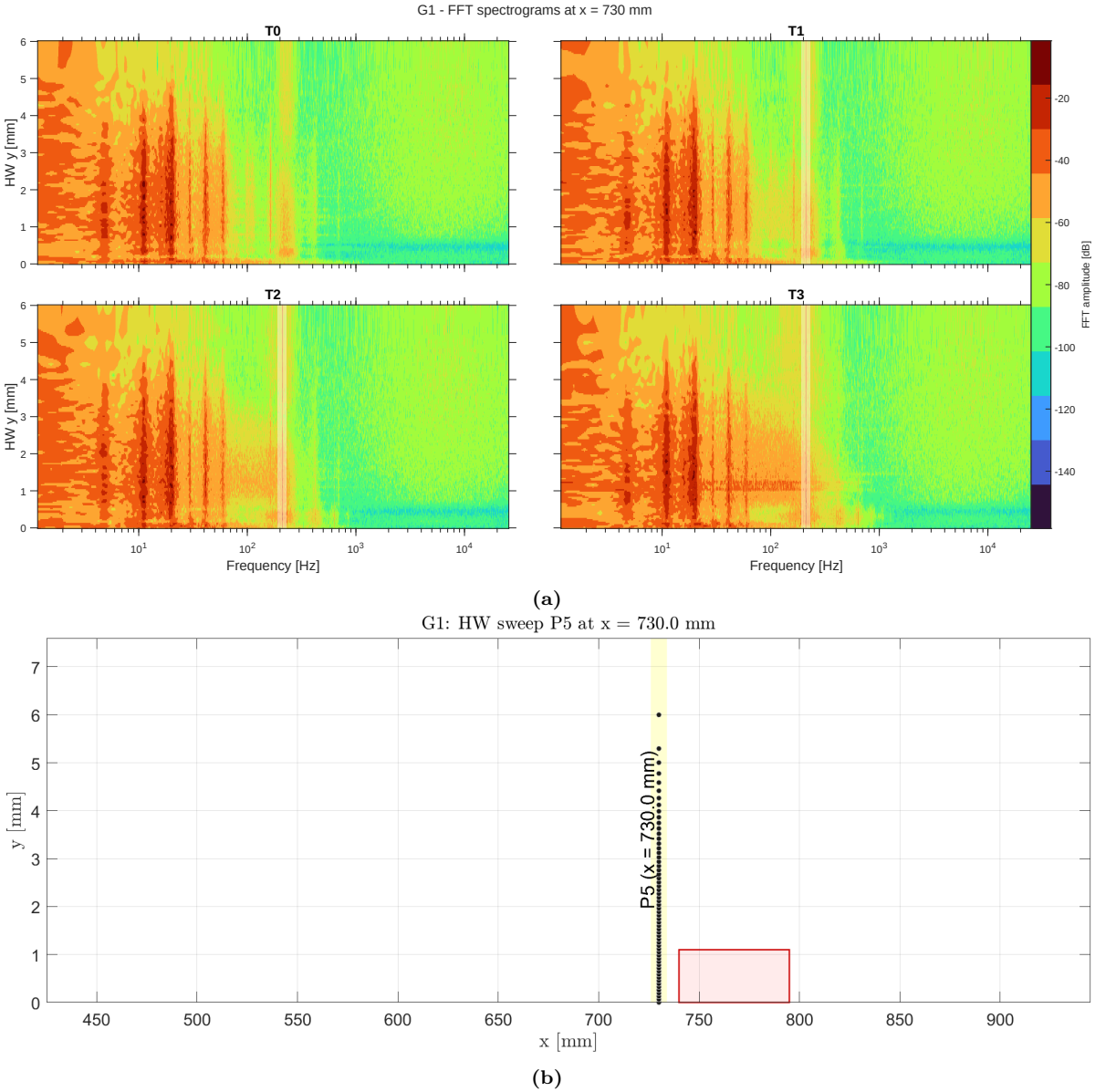

Figure 3.6: (a) FFT spectrogram at streamwise station $x = 730$ for the bump case. (b) HW sweep location for $x = 730$.

Figure 3.7, at x=742 mm (just after the FFS at x= 740 mm), shows the first HW x-station downstream of the FFS, over the bump, with the white section representing the region of the bump. This location sits at the onset of the second recirculation region that forms over the raised bump surface. While the spectrogram in Figure 3.7 does not yet show broadband growth, it indicates the laminar nature of this post-step region. This station sits at the start of the plateau region of the SERB, after the FFS, where stabilisation of the TS mode occurs, as noted by Barahona et al., 2025. These effects are more clearly observed in the TS mode shapes, which will be explored in section 3.2.

In Figure 3.7, the measured low frequency amplitude peaks, attributed to structural vibrations, are also observed to be displaced by the bump height, previously up to $y \approx$4 mm in the previous x-station, but now up to $y \approx$5 mm. The shift arises simply because the local wall-normal coordinate, y, is referenced to the displaced bump surface, which is elevated by approximately 1.1 mm relative to the flat plate. When viewed in absolute physical height above the wind-tunnel floor, the low-frequency signature remains unchanged. Therefore, the vibration peaks should not be interpreted as responding to flow features

over the bump, but as a sensor-level artefact.

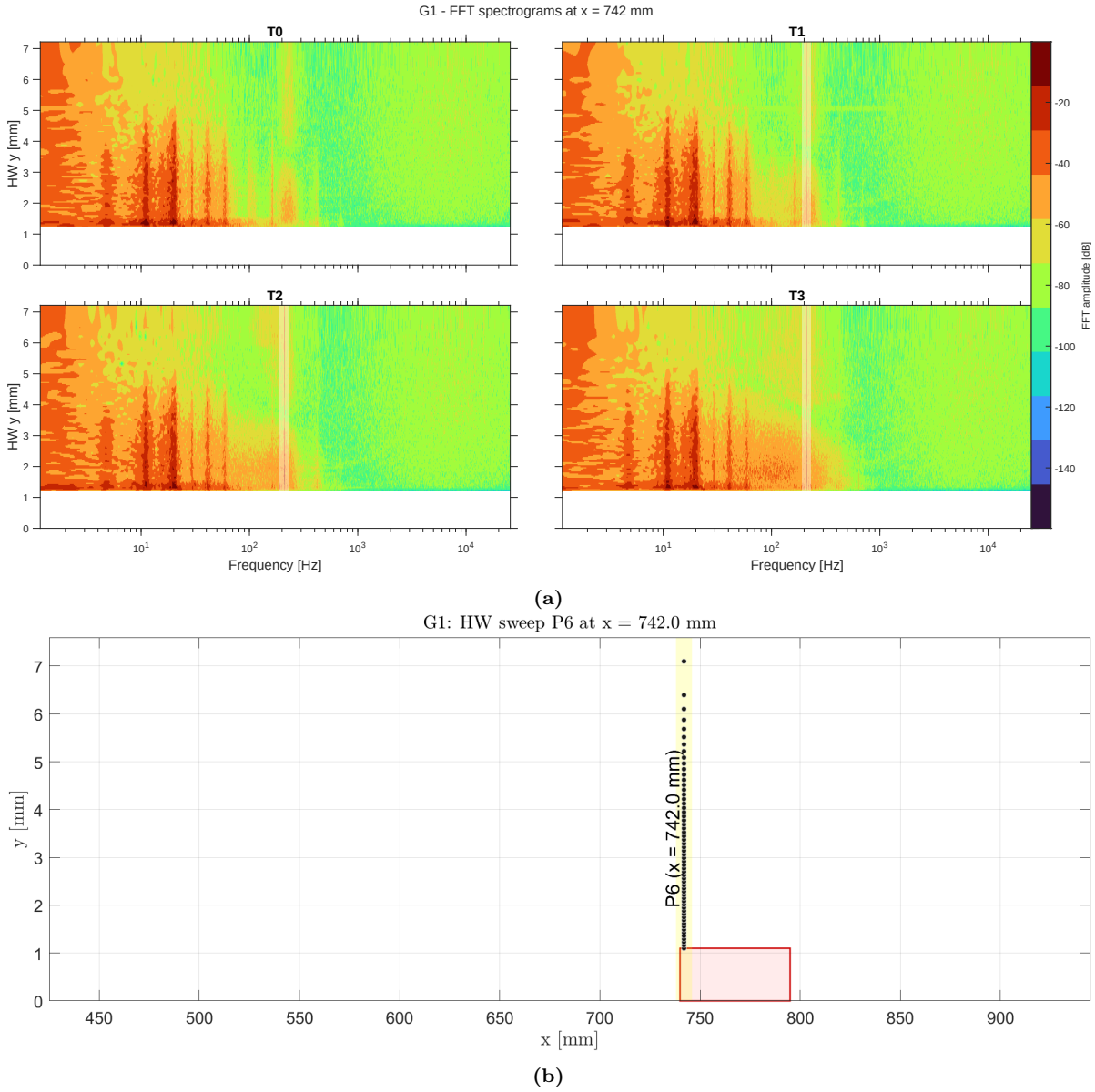

Figure 3.7: (a) FFT spectrogram at streamwise station $x = 742$ for the bump case. (b) HW sweep location for $x = 742$.

As discussed in subsection 1.4.2, the region immediately downstream of the BFS experiences a sudden expansion, imposing an adverse pressure gradient on the near-wall flow and causing separation at the BFS lip, and forming a recirculation bubble bounded by a separated shear layer. The following profiles, from Figure 3.8 at $x = 800mm$ to Figure 3.11 at $x = 830mm$, were measured downstream of the BFS (BFS at $x = 795mm$). Within this region, the mean velocity profile becomes strongly inflectional, creating a receptive environment for Kelvin–Helmholtz(KH)-type shear-layer instability and rapid disturbance amplification, with the most intense fluctuation activity typically concentrated in the shear layer and near reattachment (Armaly et al., 1983; Hasan, 1992; Teng & Piomelli, 2022).

The FFT spectrograms for Figure 3.8 (and Figure 3.9a) show a distinct band of reduced low-frequency amplitude around $y \approx 1.2$ mm. This height is consistent with the approximate location of the separated shear layer that forms above the recirculation region downstream of the BFS. The shear-layer core may

appear as a local minimum in low-frequency spectral energy when the dominant low-frequency content is not shear-layer-originated (Hasan, 1992). Therefore, the presence of a distinct low-frequency "notch" at a nearly fixed y provides qualitative evidence of a separation shear layer.

Figure 3.8 shows a horseshoe-shaped contour greater than 1 kHz, centred at $y \approx 1$ mm. This feature corresponds to the natural frequency band of the KH–type instability supported by the separated shear layer. The recirculation zone beneath the shear layer contains comparatively weak high-frequency fluctuations, while the outer flow above the shear layer attenuates these motions, yielding a closed contour in the (y, f) plane (Teng & Piomelli, 2022; Wang & Gaster, 2005). As the forcing increases (from T1 to T3). The loss of clarity in these clearly identifiable narrow-band structures indicates the previously noted "smearing" effect of the higher forcing levels and might be an indicator of transition to turbulence.

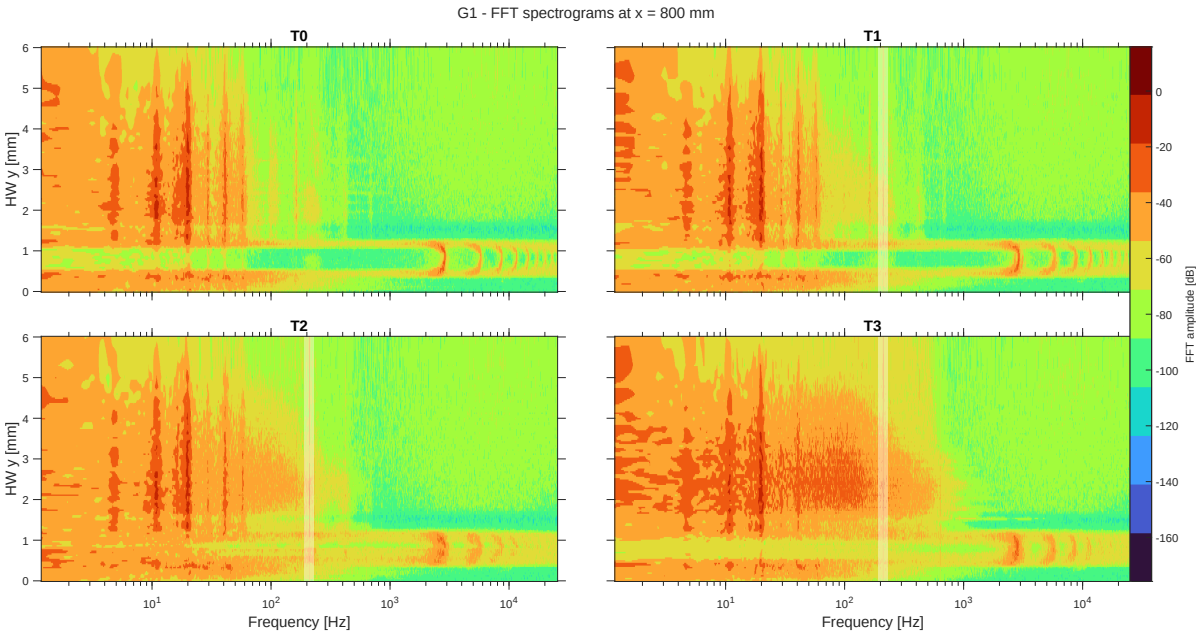

(a)

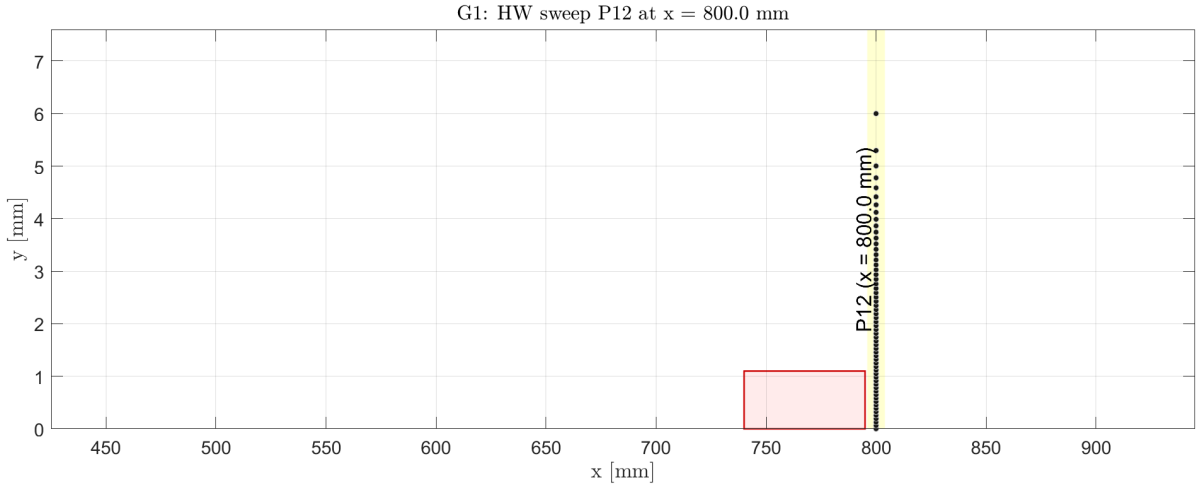

(b)

Figure 3.8: (a) FFT spectrogram at streamwise station $x = 800$ for the bump case. (b) HW sweep location for $x = 800$.

In Figure 3.9a, the high-frequency horseshoe-looking contour associated with the separated shear layer remains clearly identifiable for the unforced case (T0). While the T1 amplitude still shows remnants

of the shear layer instability, the addition of forcing seems to cause energy mixing in the y direction, and the "horseshoe" appearance for this instability disappears. For the higher forcing amplitudes, T2 is clearly seen in the T3 case in Figure 3.9a, and there seems to be a broadband amplitude rise across the entire BL sweep, consistent with breakdown and the onset of turbulent fluctuations in the separated shear-layer/reattachment region.

This could indicate that the combined effect of the KH instability and the higher TS amplitude (forced) becomes too great, eventually leading to the broad band amplitude increase seen for T3 at this $x = 810mm$ station.

This behaviour is consistent with the dynamics of a reattaching shear layer downstream of a BFS. As demonstrated in the DNS of Teng and Piomelli (2022), the inflectional shear layer experiences rapid growth of the KH instability and strong nonlinear interaction with incoming TS waves, causing loss of coherent narrow-band structure, and a progressive increase in broadband fluctuation energy.

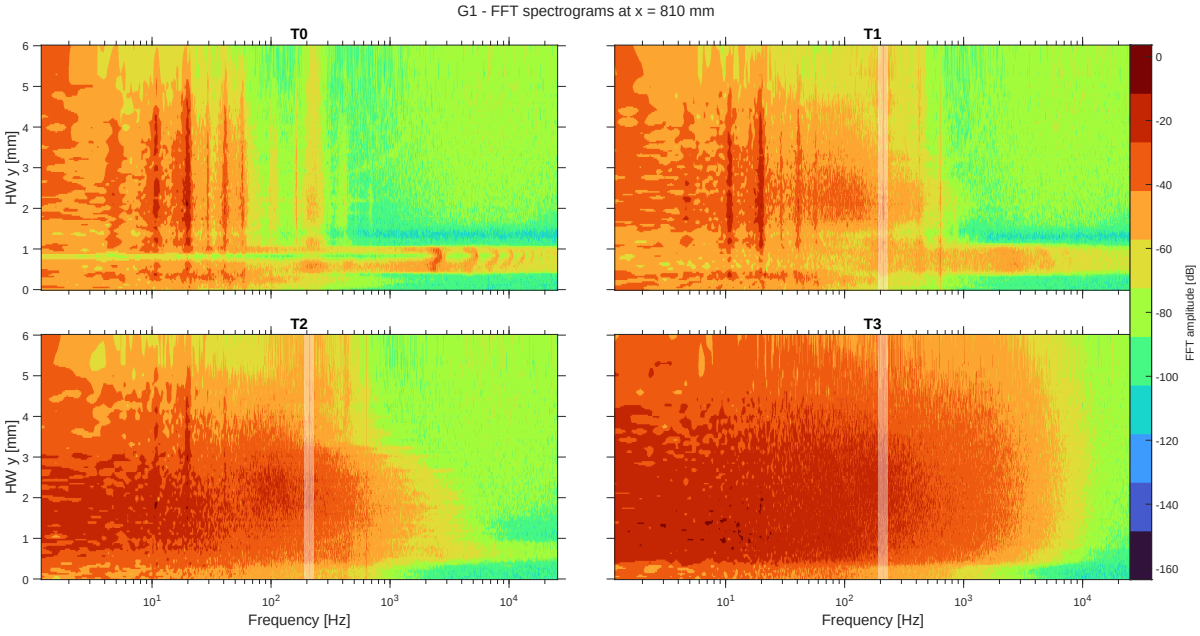

(a)

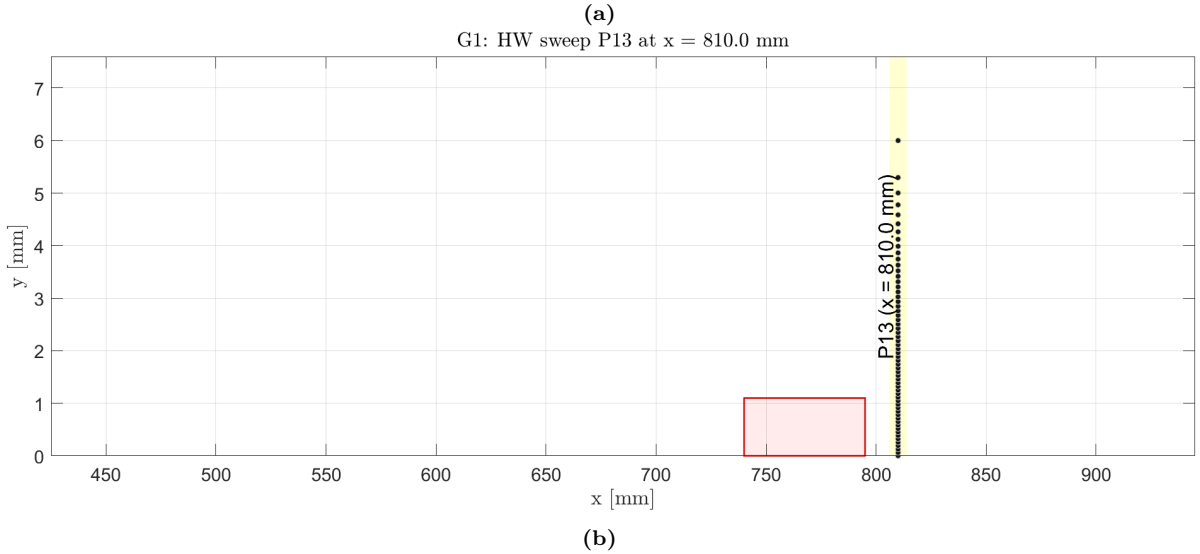

(b)

Figure 3.9: (a) FFT spectrogram at streamwise station $x = 810$ for the bump case. (b) HW sweep location for $x = 810$.

Figure 3.10 at x =820 mm suggests a reduction in broadband high-frequency energy relative to the previous station, particularly when compared with the strongly broadband character observed at x =810 mm for the higher forcing levels. This change should not be interpreted as definitive "relaminarisation", but rather, it is consistent with the intrinsically unsteady and intermittent character of reattaching shear layers, which can exhibit low-frequency flapping at the reattachment region (Hasan, 1992).

Since the hot-wire profiles at consecutive streamwise stations were acquired at different times, the probes may have sampled different separation-bubble dynamics, namely the reattachment burst at 810 mm and a calmer phase at 820 mm. This would mean that there would have had to have been some sustained phenomena at the x= 810 mm station for it to still be present after averaging over the sampling time. This is a limitation of the chosen measurement time of 3 seconds that was chosen to captiure the TS wave dynamics at the triggered 210 Hz frequency, being unable to resolve these low frequency dynamics of the recirculation Zone behind the BFS.

One can also notice from Figure 3.10 that the highest forcing amplitude case, T3, has diminished high-frequency KH signature below $y \approx 1$, which is still present in the lower amplitude cases, which would suggest some stabilising effect in the highest amplitude case.

All the triggered cases, however, still have the forced TS wave frequency (210 Hz) and its harmonics present in the spectrograms, now somewhat strengthened, indicated by the increased intensity of the triggered fundamental, f_c, and its higher harmonics ($2f_c$, $3f_c$, …), most prominently for T3. The appearance of these harmonics is consistent with nonlinear distortion of the disturbance field in the separated shear-layer/reattachment region, similar to the behaviour also reported by Hasan (1992).

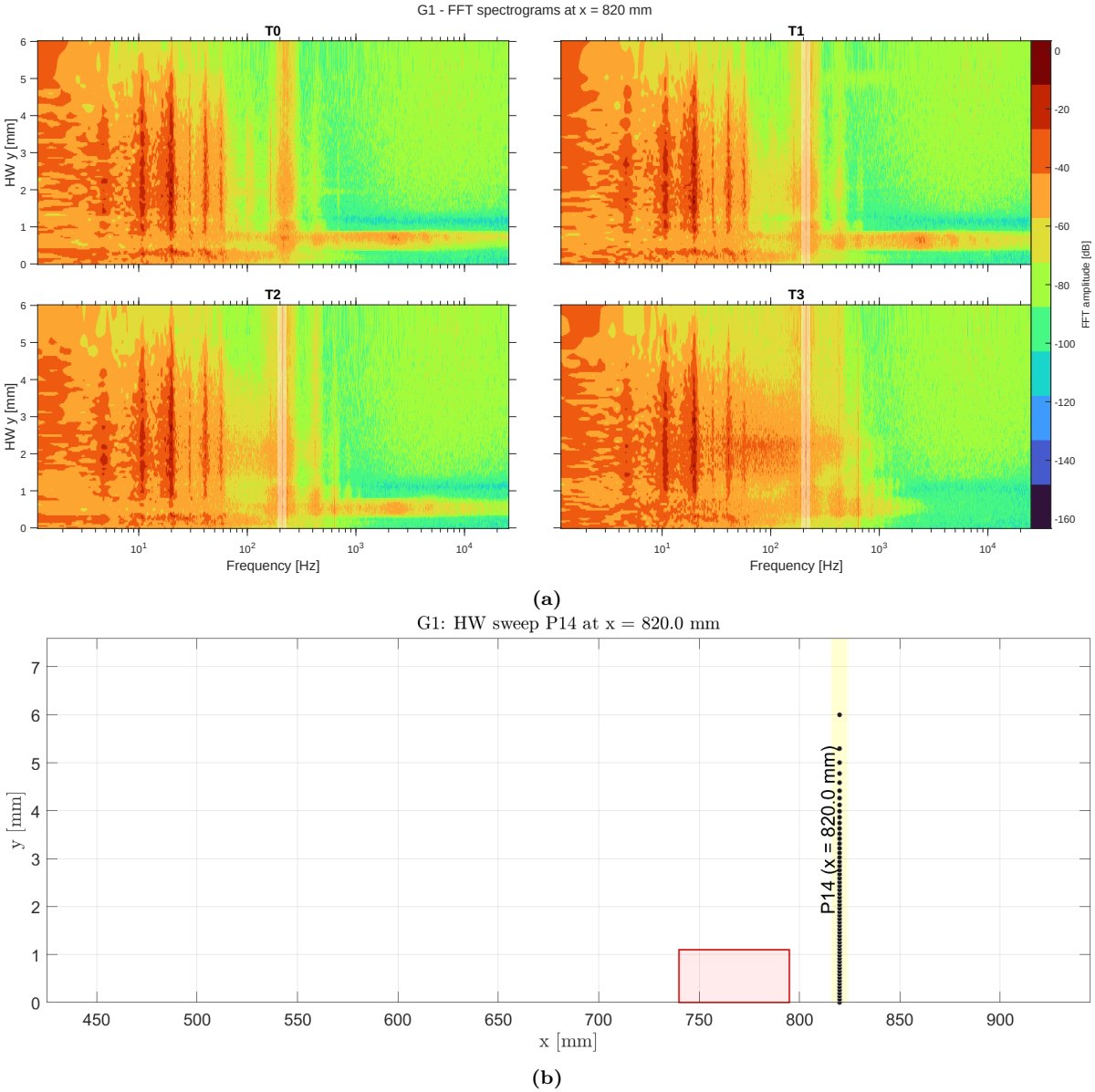

Figure 3.10: (a) FFT spectrogram at streamwise station $x = 820$ for the bump case. (b) HW sweep location for $x = 820$.

In the final HW x-station shown in Figure 3.11, the high-frequency KH signature has disappeared for all forced cases (T1–T3) that now only show a clean set of dark bands corresponding to the forced TS wave and its harmonics, indicating that the imposed TS-wave forcing remains coherent at this downstream location even though the shear-layer-related signature is no longer distinct. By contrast, the unforced case (T0) still exhibits an elevated high-frequency band consistent with continued KH-type activity.

This behaviour indicates an earlier collapse of the KH-supporting separated shear layer when the incoming disturbance amplitude is increased.

DNS data from Teng and Piomelli (2022) shows that larger incoming disturbances drive more violent shear-layer roll-up, earlier vortex merging, and rapid loss of the inflectional shear-layer structure. Since KH instabilities require a thin, strongly inflectional high-shear layer, the nonlinear distortion introduced by higher-amplitude TS forcing destroys the conditions necessary for KH amplification. As a result, the KH-type high-frequency fluctuations vanish further downstream, and the remaining disturbance field is dominated by the wall-attached TS wave, consistent with the spectrograms at $x = 830mm$. In the

unforced case, T0, the shear layer is not greatly disturbed, and thus the KH-type activity persists at $x = 830mm$.

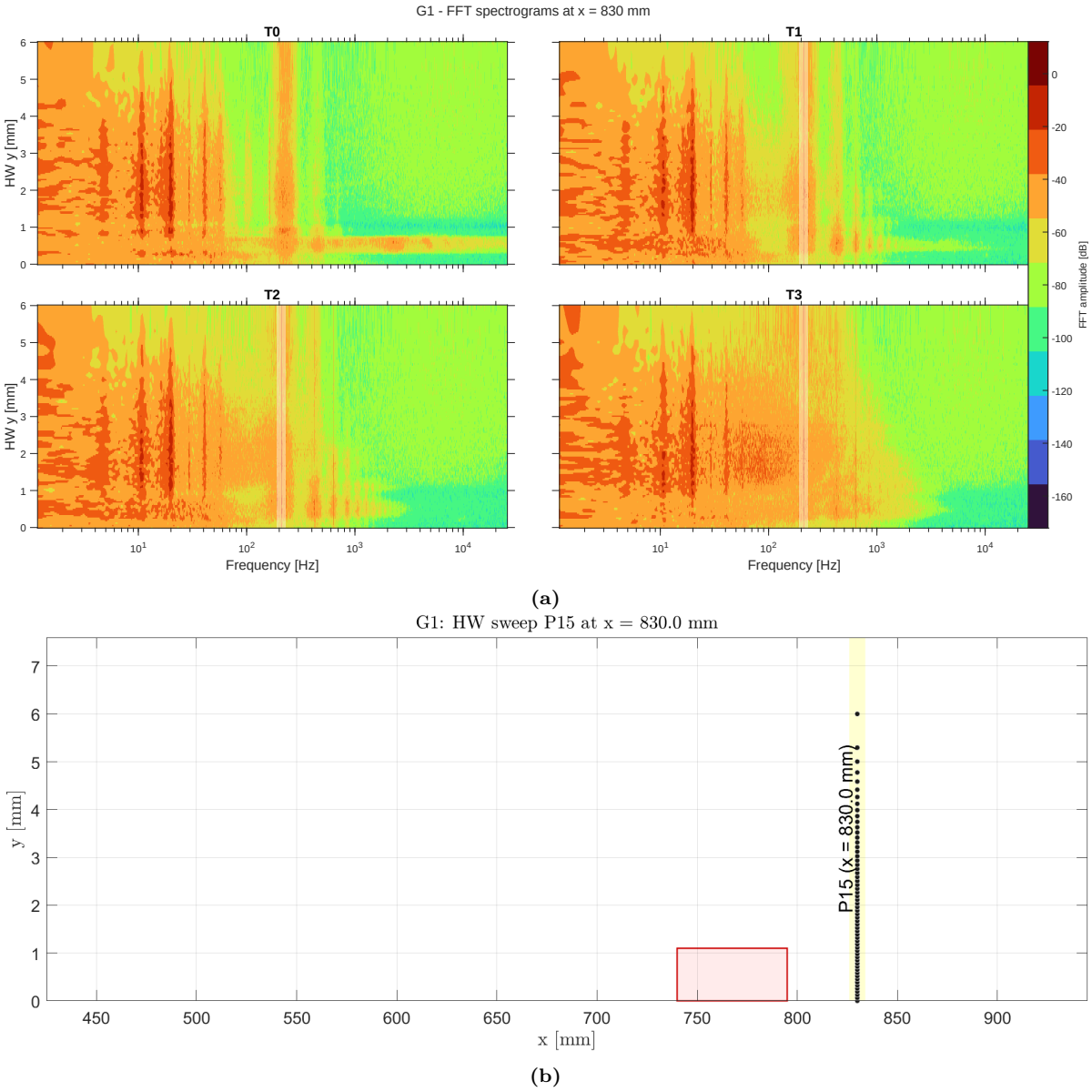

Figure 3.11: (a) FFT spectrogram at streamwise station $x = 830$ for the bump case. (b) HW sweep location for $x = 830$.

3.2. TS wave modeshape comparison

This section compares the wall-normal structure of the forced TS disturbance by extracting the velocity-fluctuation amplitude at the forcing frequency directly from the FFT spectra shown in section 3.1. The magnitude at the forcing frequency is read for each traverse height y from the corresponding FFT spectrum by selecting the discrete frequency bin closest to $f_c = 210$ Hz (e.g. the vertical marker in the spectrograms of section 3.1); repeating this across all measured y yields a wall-normal amplitude profile $|\hat{u}(y, f_c)|$. For each streamwise station, the profile is normalised by its local maximum, $\max_y |\hat{u}(y, f_c)|$, to compare the differences in wall-normal modeshape can be compared independently of absolute amplitude. In an attached Blasius-type boundary layer, the TS mode shape exhibits the characteristic double-lobed amplitude distribution, which is expected to be clearly present in the clean case (Fig-

ure 3.12) and in the bump case (Figure 3.13) upstream of the forward-facing step, and to persist over attached portions of the bump upstream of the backward-facing step.

3.2.1. Clean Case

In Figure 3.12, T1 to T3 denote increasing forcing amplitudes (see Table 2.2). Across most streamwise stations the extracted TS mode-shape proxies exhibit a clear two-lobed structure, with an inner lobe near the wall and an outer lobe at larger y, consistent with the expected TS-wave eigenfunction behaviour in an attached Blasius-type boundary layer. A weak downstream shift of the inter-lobe minimum towards larger y is observed, consistent with a gradual rescaling of the wall-normal structure as the boundary layer thickens downstream.

A dependence on forcing is also evident in the wall-normal amplitude distribution. Most clearly seen in the stations $x \approx 750$ to 770 mm, increasing the forcing level (T1→T3) reduces the relative prominence of the outer lobe while strengthening the inner lobe. The observed reduction of the outer-to-inner lobe ratio is associated with a greater contribution of the disturbance within the high-shear region near the wall, which adds greater energy near the wall.

Although the DBD plasma actuator produces a body-force field that is strongly localised close to the wall in the actuation region, the present mode-shape measurements are obtained approximately 0.37 m downstream of the actuator location ($x = 0.38$ m), i.e. several TS wavelengths downstream. The observed strengthening of the near-wall lobe with increasing forcing is therefore interpreted primarily as a forcing-dependent modification of the downstream f_c disturbance field, rather than as a direct imprint of the near-wall body-force distribution at the actuator.

3.2.2. Bump Case

Since a single-wire probe is sensitive to the resultant in-plane velocity and cannot separate (u, v) components, the interpretation in terms of a TS mode shape is most reliable in regions where the boundary layer is attached and $V \ll U$; close to the step edges and within separated/reattaching regions, the extracted profiles can be interpreted as the wall-normal structure of the 210 Hz frequency.

Upstream of the FFS ($x \leq 730$ mm), the normalised profiles retain the canonical double-lobed structure observed in the clean case, indicating that the forced disturbance at f_c remains TS-like and the boundary layer remains attached in this region, with the differences between T1 to T3 mostly in subtle changes relative prominence of the inner and outer lobes. A weak near-wall peak is observed at $x = 730$ mm, close to the upstream face of the SERB's FFS. Barahona et al. (2025) reports that a forward-facing step can generate an additional near-wall maximum in the TS-wave shape function in the immediate step vicinity, and interprets this feature using her DNS results as a step-induced secondary perturbation structure produced at the step edge and superimposed on the incoming TS wave.

Across the bump surface between the FFS and BFS (740 mm $\leq x \leq$ 795 mm), the f_c mode-shape profiles remain predominantly two-lobed but exhibit increased shape variability as compared to upstream stations. Immediately downstream of the FFS (at $x = 742$ mm station), the inner (near-wall) lobe appears sharper and the inter-lobe minimum occurs at a smaller wall-normal height y, indicating a local reshaping of the f_c response in the near-step region. Similar near-step modifications of TS mode-shape profiles have been reported downstream of forward-facing steps (Barahona et al., 2025). Immediately downstream of the FFS (at $x = 742$ mm), the inner (near-wall) lobe appears sharper and the inter-lobe minimum occurs at a smaller wall-normal height y, indicating a local reshaping of the f_c response in the near-step region. Similar near-step modifications of TS mode-shape profiles have been reported downstream of forward-facing steps (Barahona et al., 2025). Moving downstream towards the BFS, the inter-lobe minimum becomes progressively less pronounced and shifts to larger y, while the near-wall lobe broadens, suggesting a gradual recovery of the wall-normal structure away from the abrupt FFS-induced distortion. This evolution is qualitatively consistent with the stabilisation region reported downstream of the FFS, where the perturbation field relaxes, and TS-wave growth is temporarily reduced before subsequent downstream re-destabilisation (Barahona et al., 2025), also seen in section 3.3 below.

Downstream of the BFS ($x \geq 795$ mm), the extracted f_c profiles are consistent with the presence of a separated shear layer and reattachment dynamics behind the BFS, where the hot-wire signal can contain

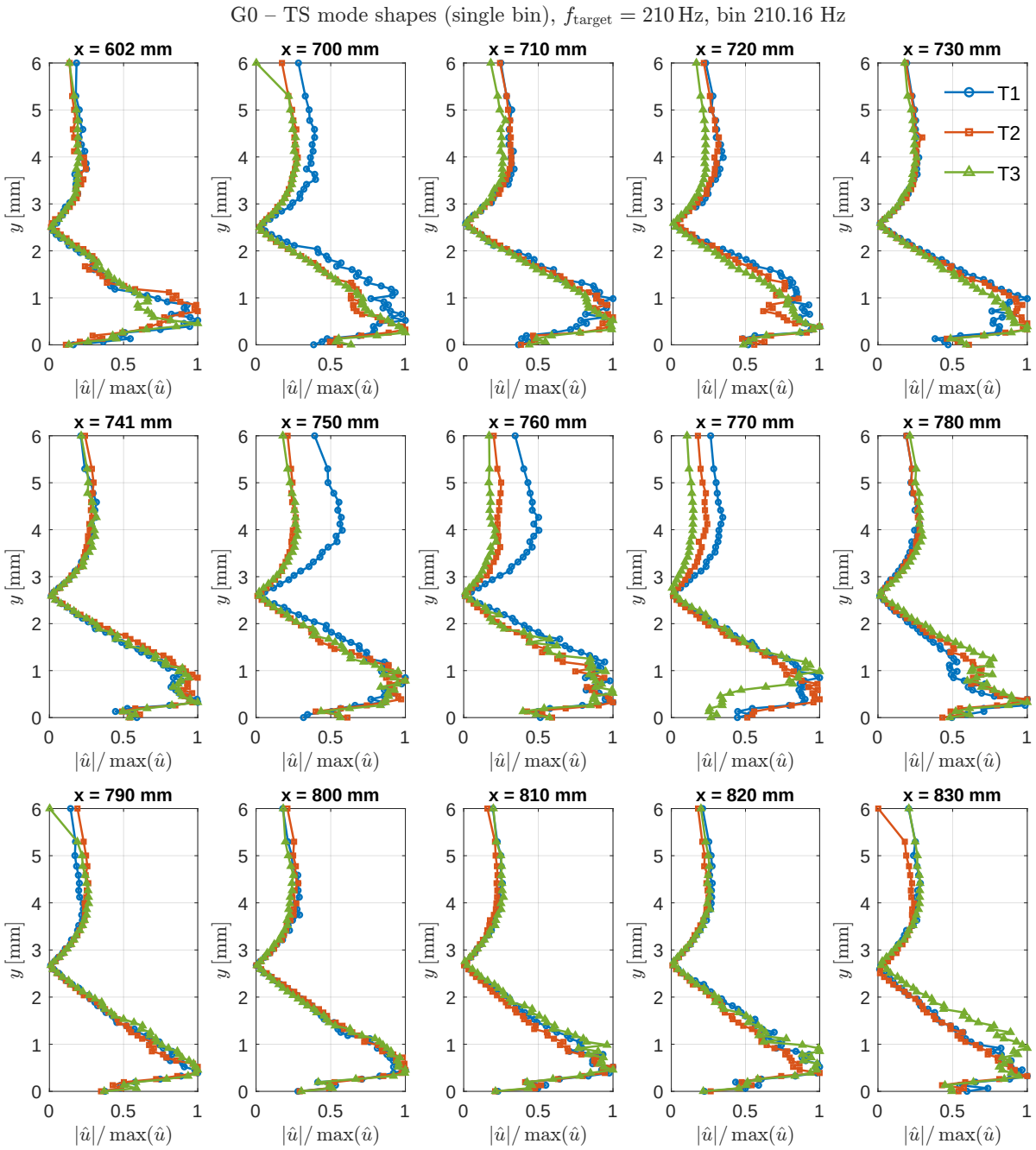

Figure 3.12: Wall-Normal profiles of the fundamental TS frequency, $f_c = 210$ (Closest frequency bin=210.16 Hz), at different streamwise measurement locations for the clean case

significant wall-normal velocity contributions and where the f_c bin can represent a forced response of the separated shear layer rather than a wall-attached TS eigenfunction. Accordingly, the downstream profiles are interpreted as the wall-normal structure of the 210 Hz response in the separated/reattaching flow rather than as TS mode shapes. In all stations downstream of the BFS ($x \geq 795$ mm), a two-lobed structure remains discernible at larger wall-normal positions; however, the profiles are disrupted by a pronounced local minimum around $y \approx 1.2$ mm, i.e. approximately the SERB step height at the first station, but closer to the wall in downstream stations. This feature is consistent with the separated shear layer forming above the recirculation region, such that the extracted f_c amplitude is reduced near the shear-layer core while remaining elevated above and below it, as also suggested by the FFT spectrograms discussed in section 3.1. The same qualitative wall-normal features (two-lobed structure and the local minimum near $y \approx 1.2$ mm) are observed for all forcing cases.

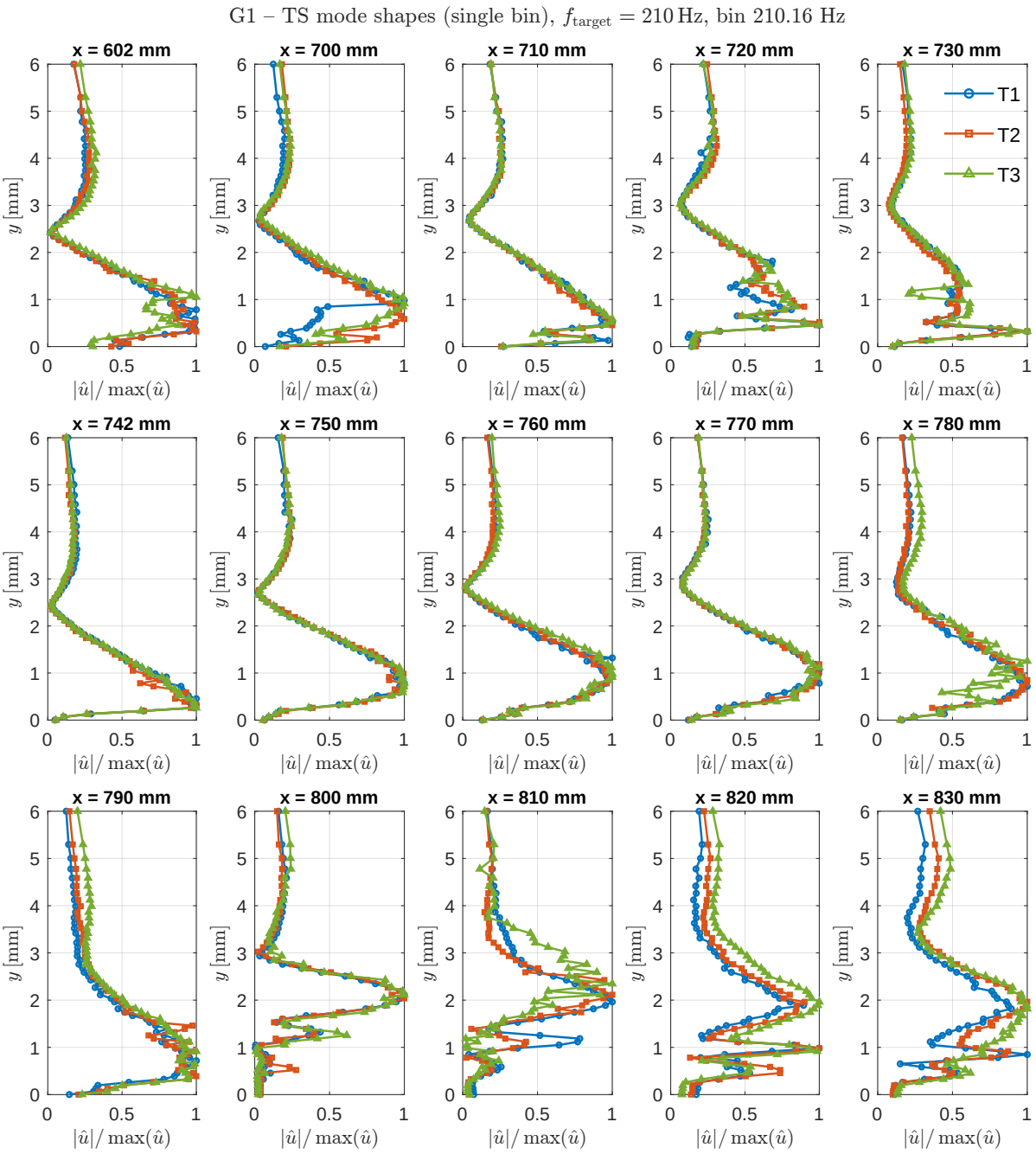

Figure 3.13: Wall-Normal profiles of the fundamental TS frequency, $f_c = 210$ Hz, at different streamwise measurement locations, SERB FFS located at x=740 mm, SERB BFS located at x=795 mm

3.3. TS Wave Growth / N-Factor

This section examines the streamwise growth of the forced disturbance for both the clean plate in subsection 3.3.1 and SERB cases in subsection 3.3.2. By extracting the amplitude of the forced fundamental across the wall-normal hot-wire sweeps, both amplitude-based and energy-based measures of disturbance growth can be compared as a function of streamwise location and forcing amplitude. The figures in this section show the growth of the triggered frequency fundamental, f_c = 210 Hz, in terms of amplitude, as well as amplitude-based and energy-based N-factors.

3.3.1. Clean Case

After the disturbance amplitudes $A(y, f_c; x)$ at each streamwise station, x, and height, y, for a target frequency, f_c=210 Hz are obtained in section 3.2, the peak-amplitude envelope for each x-station is determined by

$$A_{env} = max_y A(y, f_c; x) \tag{3.2}$$

Figure 3.14 plots this peak amplitude for each HW sweep, normalised by external velocity measured at that sweep location. This should be noted when comparing with subsequent N-factor figures, which only show growth of the fundamental relative to the most upstream HW measurement location.

As mentioned in subsection 2.1.4 the amplitude readout of microphone 1 was monitored and maintained approximately constant across all forcing cases. However, microphone 1 was located at x= 430 mm, upstream of the first HW sweep at x= 602 mm (refer Table 2.5), resulting in differing initial amplitudes for each forcing case at the most upstream HW sweep location, x= 602 mm station, as seen in figure 3.14. Figure 3.14 clearly marks the amplitude spike for T3 at the x = 770 mm station as an outlier when compared to the T2 spike at x = 770 mm, based on the initial amplitudes recorded at x= 602 mm. The value will also be confirmed below as an outlier based on the synced microphone recordings at this location.

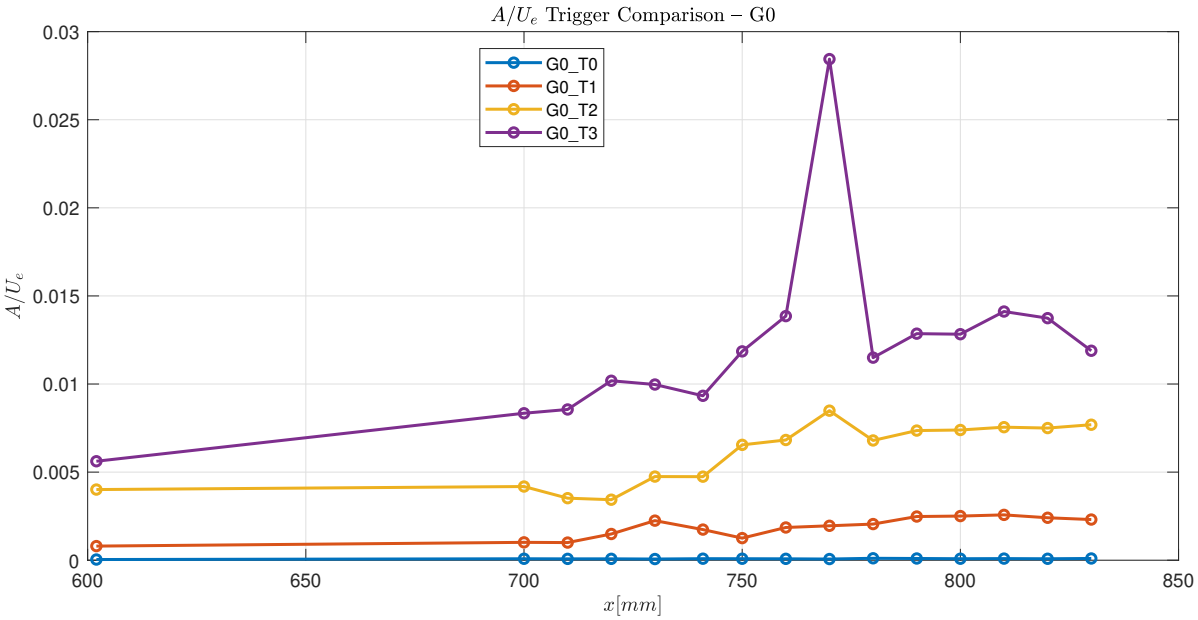

Figure 3.14: Amplitude of the fundamental frequency, $f_c = 210\ Hz$, at each measurement location, for the clean case. Lines between experimental points are only drawn to indicate the data trend.

Taking the peak amplitude of the first HW x-station, x_0= 602 mm, to be $A_0 = A_{env}(x_0)$, the amplitude-based N-factor is then

$$N(x) = \ln\left(\frac{A_{env}(x)}{A_0}\right) \tag{3.3}$$

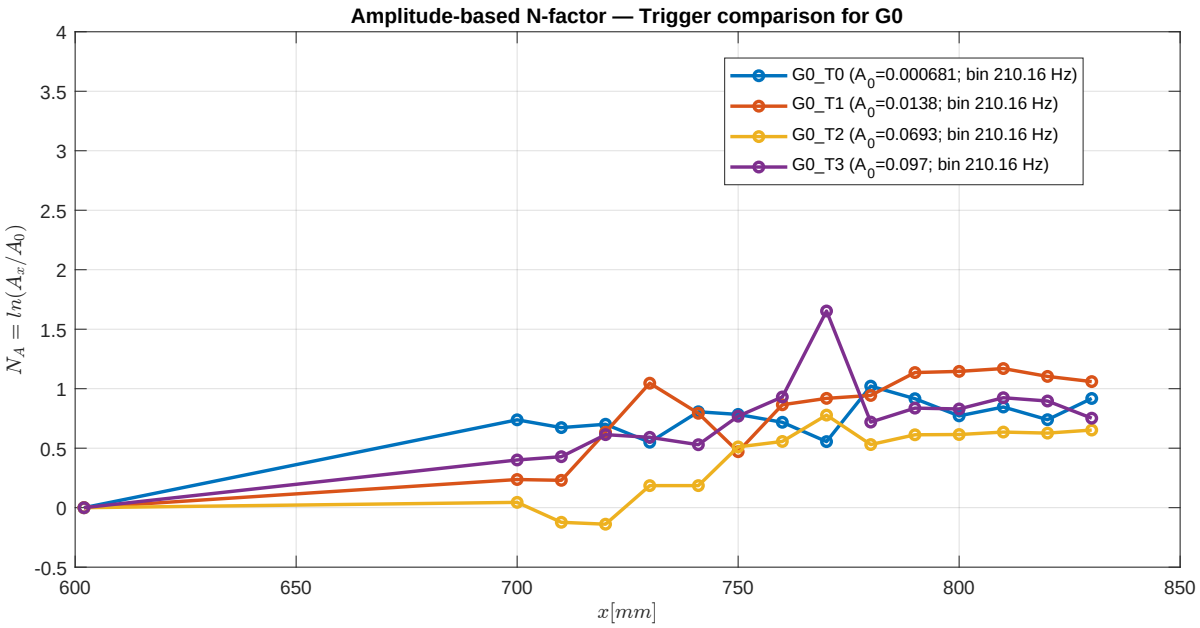

Figure 3.15: Amplitude base N-factor of the fundamental frequency, $f_c = 210\ Hz$, for different trigger cases, for the clean case. Lines between experimental points are only drawn to indicate the data trend.

Using the amplitude-based N-factor is the standard approach, but is prone to mistakes or noise in picking a single peak from a jagged mode shape from Figure 3.12. Given a per-height disturbance amplitude at the target tone f_c, an alternative approach would be to use the disturbance kinetic energy, which involves squared fluctuations. The disturbance kinetic energy is obtained by the wall-normal integral of the squared TS amplitude across the height of the HW sweep.

$$E(x) = \int_0^{y_{\max}} [A(y, f_c; x)]^2 dy \tag{3.4}$$

Or normalising with external velocity,

$$E^{(U_e)}(x) = \int_0^{y_{\max}} \left(\frac{A(y, f_c; x)}{U_e(x)} \right)^2 dy. \tag{3.5}$$

Taking the disturbance kinetic energy of the first HW station, x_0= 602 mm, to be $E_0 = E(x_0)$, the energy-based N-factor is then

$$N_E(x) = \ln \left(\frac{E(x)}{E_0} \right) \tag{3.6}$$

Resulting in the curves present in Figure 3.16.

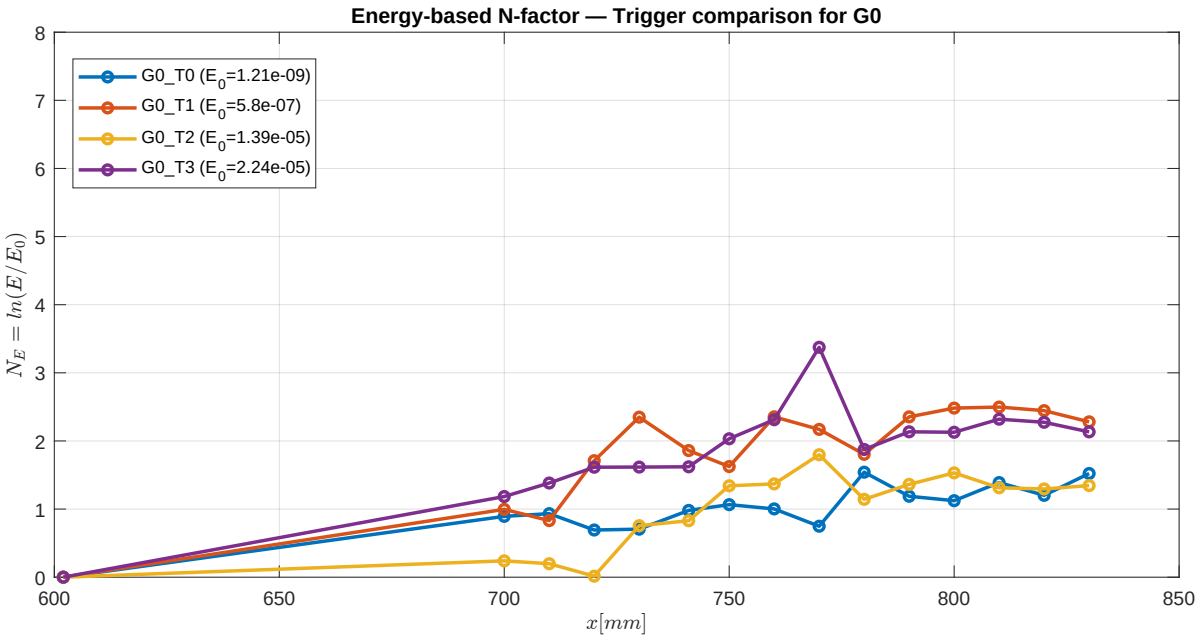

Figure 3.16: Energy base N-factor of the fundamental frequency, $f_c = 210\ Hz$, for different trigger cases, for the clean case. Lines between experimental points are only drawn to indicate the data trend.

Although the general trends observed for individual trigger cases for the amplitude-based N-factor curves (Figure 3.15), are similar to the energy-based N-factor curves (Figure 3.16), the difference between these approaches is apparent when comparing the relative slopes and offsets between trigger cases for the HW sweep locations upstream of the $x = 740$ sweep location,

For the clean case in Figure 3.15, the curves of the triggered (T1,T2,T3) and untriggered case (T0) show classic monotonic TS wave growth expected for a Blasius BL. The T1 and T2 cases show normal TS growth from $x = 600$ mm to 830 mm with no anomalous behaviour. The spike in amplitude at the $x = 770\ mm$ station for the highest trigger amplitude, T3, was observed in Figure 3.14, Figure 3.15 and also in Figure 3.16, meaning it is an actual feature of the measured signal, not an artefact of the mode-shape peak selection process. As noted above, this point is likely the outlier, as downstream of this point, the T3 amplitude returns to the expected stable plateau, consistent with the mild nonlinear saturation expected for large-amplitude TS waves on a clean plate.

To confirm this hypothesis, one can examine the simultaneous microphone measurements captured during each HW measurement for every HW sweep. Since the mics are surface-mounted, variations are not expected in the measured values of the microphones corresponding to each point in the vertical y location of a HW sweep. Additionally, the measurements of a specific fixed surface microphone, at a specific forced amplitude (T0 to T3), is not expected to change with streamwise x location of the HW. Thus, any large variation in measured microphone amplitude between HW sweeps would indicate external influence on the measurements at these locations, such as variations in actuator performance.

Figure 3.17 shows the peak amplitude of the trigger frequency ($f_c = 210Hz$) from the FFT of the signal recorded by upstream microphones, with each dot representing the measured microphone amplitude, and the location of each dot corresponding to the location of the HW probe. In Figure 3.17, Mics 3, 4, and 5 all show a spatially uniform increase in amplitude for the T3 case, at the HW sweep location, $x = 770\ mm$. Only 3 mics are represented in this figure, but the same observation was made for the majority of the surface-mounted mics.

After accounting for EMI interference (in subsection 2.6.1), with tunnel flow conditions remaining constant accross all measurements, such a spike observed in both microphones and HW measurements, as detailed above, would indicate a transient actuator fluctuation rather than the growth of boundary-layer instability for this $x = 770\ mm$ HW sweep.

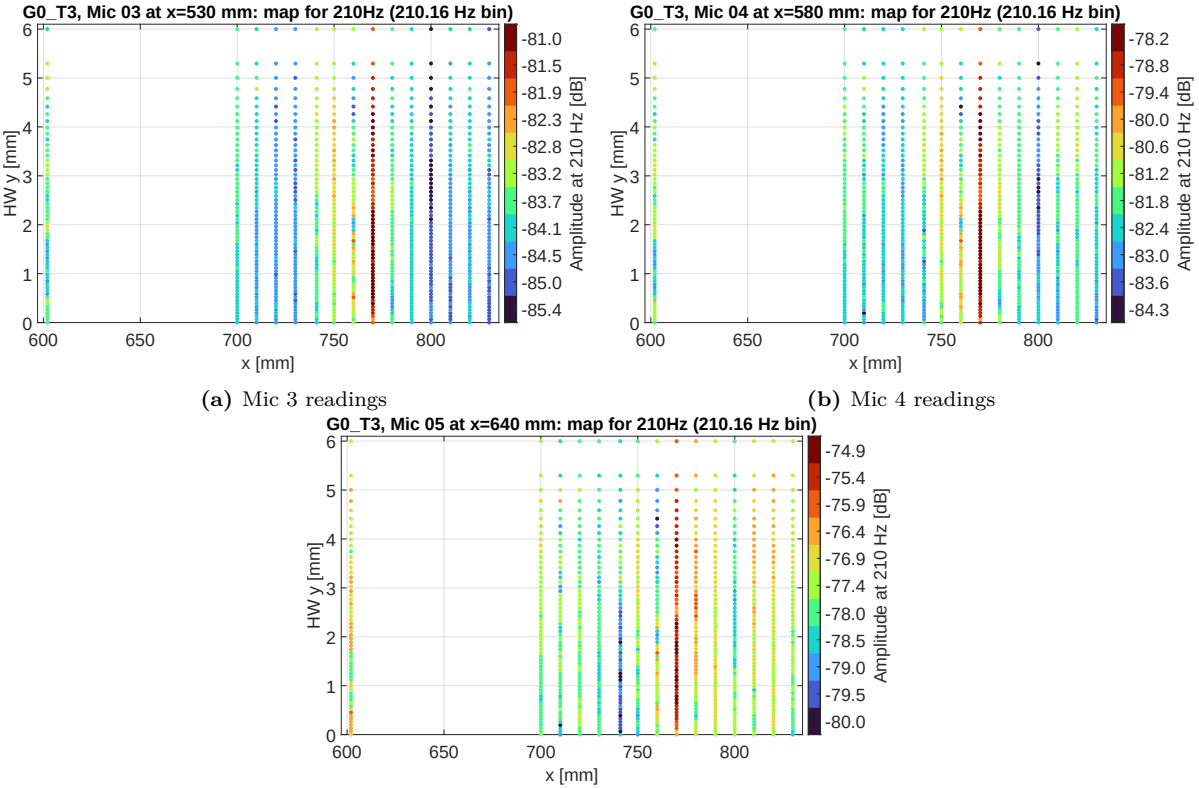

(a) Mic 3 readings

(b) Mic 4 readings

(c) Mic 5 readings

Figure 3.17: Peak amplitude map recorded by the mics for the triggered frequency of 210Hz, corresponding to each measurement location in the HW sweep for the clean case (G0) with maximum forcing (T3)

3.3.2. Bump Case

Similar processesing and plotting routines to subsection 3.3.1 are followed to plot the growth curves in this section with Figure 3.18 showing the amplitude for each HW sweep, Figure 3.19 showing the amplitude-based N-factor, and Figure 3.20 showing the energy-based N-factor.

Like the clean case in subsection 3.3.1, the microphone amplitudes were inspected to understand the origin of the spikes observed at the $x = 700$ mm and $x = 810$ mm HW stations. The microphone maps in Figure A.1, Figure A.2, and Figure A.3, correspond to the simultaneous microphone measuremnts at T1, T2, and T3, respectively. These figures show that, during the HW sweeps at these two locations, all microphones consistently recorded a higher amplitude at the forced frequency ($f_c = 210$ Hz), indicating a momentarily stronger forcing amplitude for these HW sweeps similar to subsection 3.3.1.

Importantly, neither of these spikes can be linked to the flow physics of the bump. The bump does not influence the BL 40mm upstream of the FFS at $x = 700$ mm, and the behaviour at $x = 810$ mm does not match any BFS-related instability signature. If this spike was physical, the measured increase in N-factor would not suddenly dissapear at the next x station, $x = 820$ mm. In addition, the same amplitude rise appears in all three triggered cases (T1–T3), which were recorded sequentially. These observations strongly suggest that the spikes are caused by a temporary change in the plasma actuator output, rather than by any instability growth or geometric effect. These points should therefore be treated as actuator-induced artefacts and not included in the physical interpretation of the N-factor curves. Apart from these two x stations, all remaining features in the amplitude and energy N-factor curves are physically consistent with the expected flow physics around sharp-edged rectangular bumps, and are discussed below.

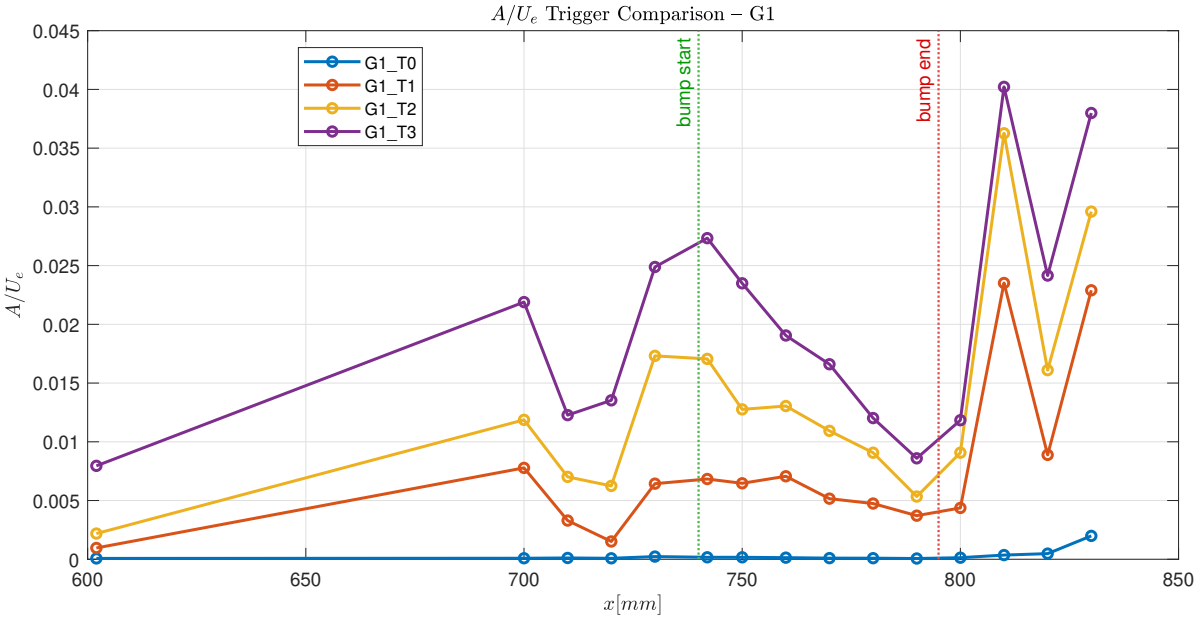

Figure 3.18: Amplitude of the fundamental frequency, $f_c = 210\ Hz$, at each measurement location, with the bump. Lines between experimental points are only drawn to indicate the data trend.

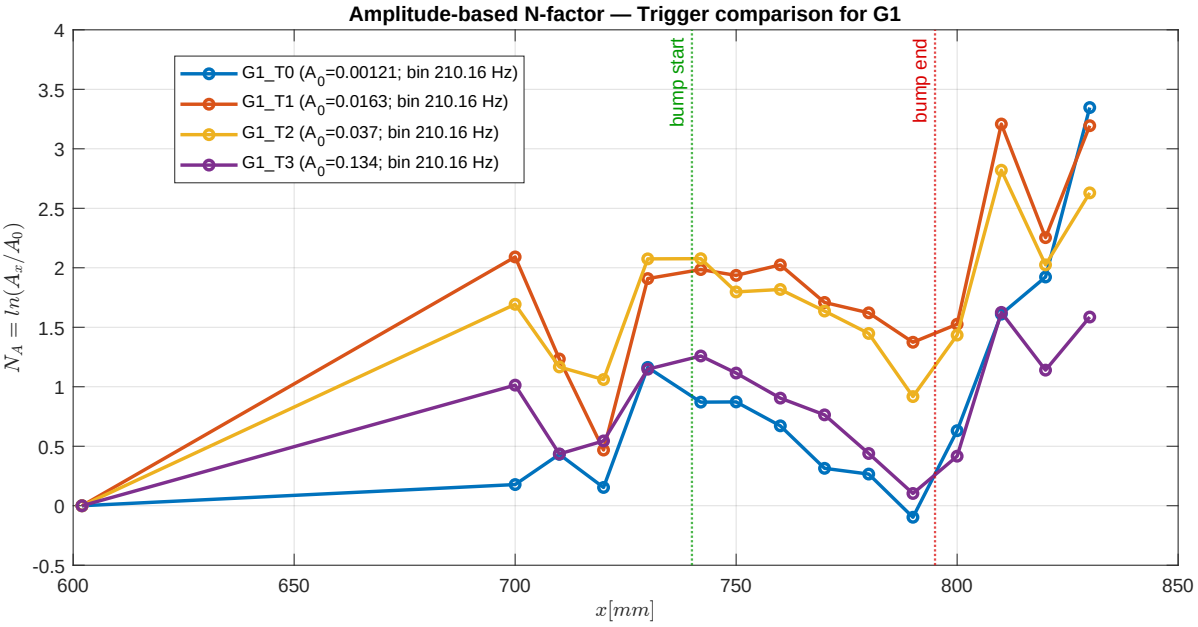

Figure 3.19: Amplitude base N-factor of the fundamental frequency, $f_c = 210\ Hz$, for different trigger cases, for the bump case. Lines between experimental points are only drawn to indicate the data trend.

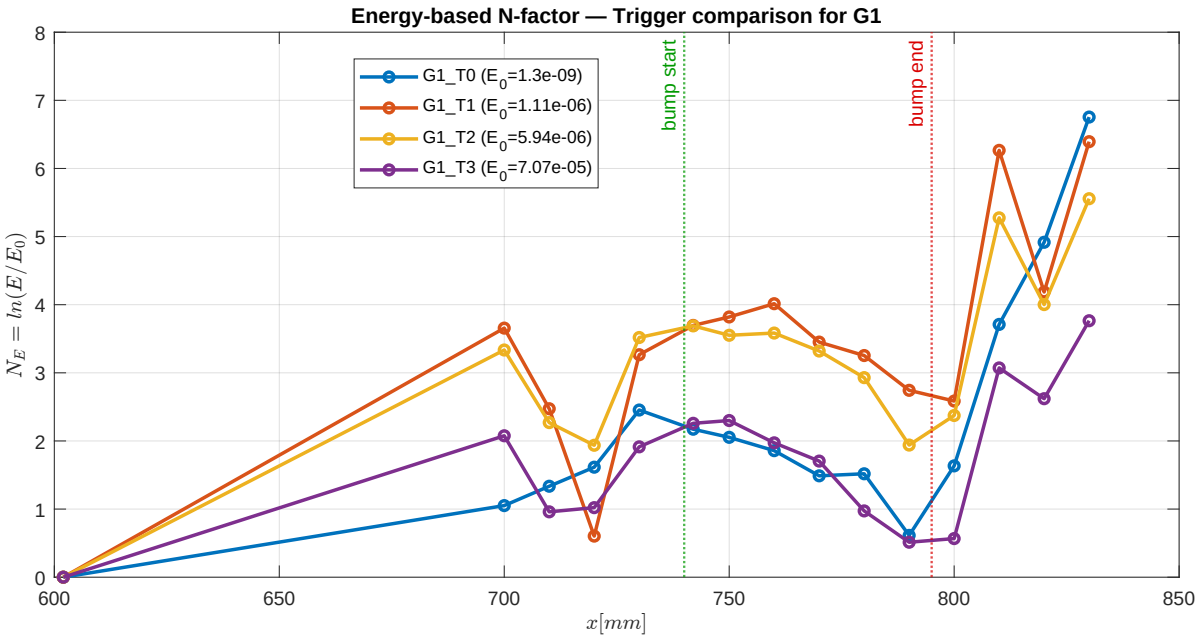

Figure 3.20: Energy base N-factor of the fundamental frequency, $f_c = 210\ Hz$, for different trigger cases, with the bump. Lines between experimental points are only drawn to indicate the data trend.

The growth curves for the bump case (G1), reveal three distinct behaviours in the 3 regions of the SERB:

1. Upstream of the SERB's FFS($x < 740$ mm): Apart from the unphysical spikes, all triggered cases exhibit a smooth rise in both the amplitude-based and energy-based N-factors similar to the clean case, with an increase in N-factor in the x station right in front of the FFS, which was also seen by Barahona et al. (2025). This is consistent with existing literature (Crouch & Kosorygin, 2020; Wang & Gaster, 2005) which report that a surface protrusion induces an upstream pressure adjustment that slightly distorts the base flow and modifies the local TS eigenfunction over an influence distance of order $\mathcal{O}(\delta^*)$.

   Inspection of the amplitude evolution in Figure 3.18 further reveals that in the higher forcing cases (T2 and especially T3), the second and third harmonics are already measurable ahead of the FFS, whereas in T1 the fundamental disturbance remains clearly dominant. The increase in harmonic content scales with forcing amplitude, indicating that nonlinear distortion begins earlier for higher forcing amplitudes.

2. Over the SERB's raised surface (740 mm to 795 mm, between the FFS and the BFS): Just after the FFS, the baseflow is distorted, and over the flat upper surface of the bump, there is a gradual decrease in amplitude and N-factor. This is consistent with Wang and Gaster (2005), who showed the thickening of the BL leading to a region of reduced TS amplification extending downstream of the step with some upstream influence of the separation bubble caused by the BFS noted by Hildebrand et al. (2020).

   It is interesting to note from Figure 3.19 that the N-factor curve of the T3 case lies below those of the T1 and T2 cases, more closely matching the slope and values for the untriggered T0 case, likely due to normalisation by a greater initial amplitude A_0. More importantly, the energy-based N-factor (Figure 3.20) does not show a disproportionate reduction of total disturbance energy for T3. All trigger cases show a comparable decrease in N-factor over the raised surface.This comparison indicates that the plateau effect is a base-flow modification acting similarly across forcing amplitudes, rather than a selective stabilisation of the highest forcing case.

   Further insight is obtained by examining the absolute disturbance amplitudes and harmonic content (Figure 3.18). In the highest forcing case (T3), the second and third harmonics attain amplitudes much closer to that of the fundamental over the plateau region, whereas in the T1 case

the fundamental remains clearly dominant upstream of the BFS. This elevated harmonic content in T3 suggests earlier onset of weak nonlinear distortion and redistribution of disturbance energy among harmonics. The initial fundamental amplitude A_0 in T3 is nearly an order of magnitude larger than in T1, indicating that the disturbance enters a weakly nonlinear regime much earlier in the streamwise direction, which generates higher harmonics and reduce the purely exponential growth of the fundamental. The reduced fundamental N-factor observed over the plateau for T3, therefore, likely reflects nonlinear redistribution of energy into higher harmonics and partial saturation effects, rather than genuine stabilisation of the instability mechanism.

3. Downstream of the SERB's BFS ($x > 795$ mm): Ignoring the outlier at $x = 810\ mm$, after the BFS, all cases exhibit a pronounced increase in TS amplitude, reflecting the strong amplification associated with the separated shear layer formed behind the step. This behaviour is consistent with classical BFS studies (Armaly et al., 1983; Hasan, 1992; Hildebrand et al., 2020; Teng & Piomelli, 2022), which show that the inflectional velocity profile within the separated shear layer significantly increases local disturbance growth rates.

   While the amplitude-based N-factor curves indicate that the untriggered case (T0) exhibits the largest relative growth downstream of the BFS, but using a substantially smaller initial amplitude A_0, confirmed by Figure 3.18.

   The strong amplification observed in all cases, and the rapid growth of the harmonics, indicate that the separated shear layer behind the BFS acts as a convective amplifier of incoming disturbances. The larger proportional amplification observed in the T0 case suggests that disturbances entering the BFS region from a near-linear regime may experience greater relative growth, whereas the higher forcing cases, having already entered a weakly nonlinear state upstream, exhibit reduced relative amplification of the fundamental frequency.

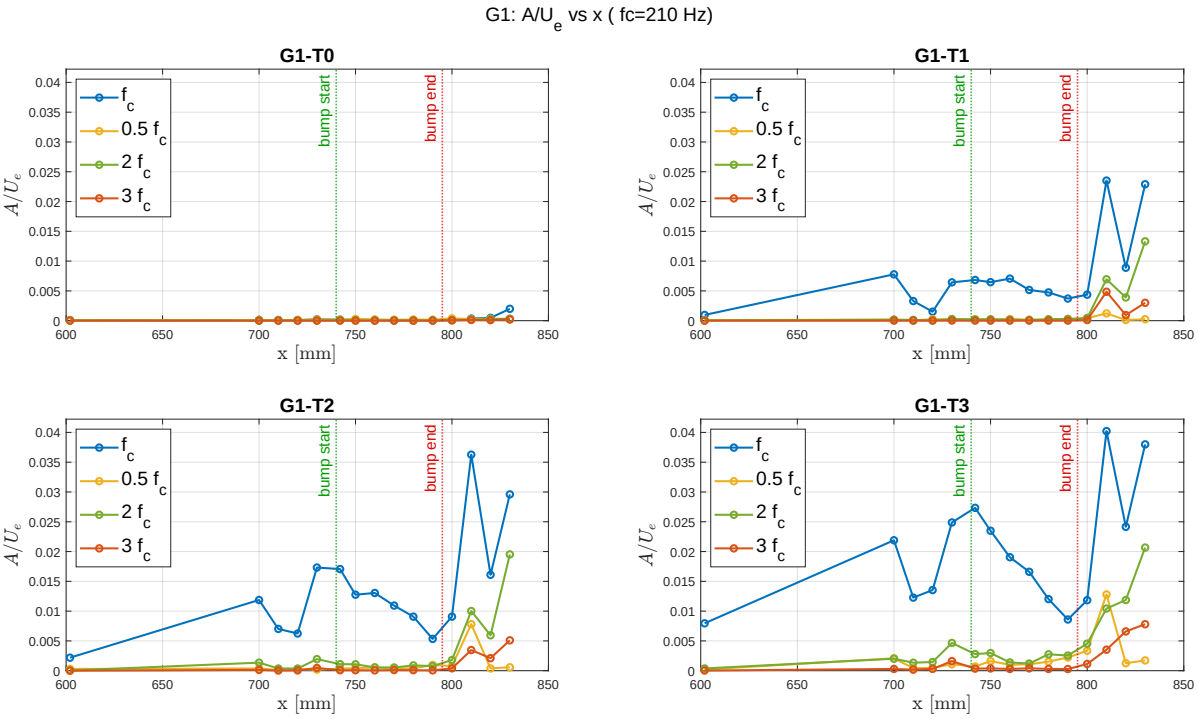

Figure 3.21: Amplitude of the fundamental, $f_c = 210\ Hz$, harmonics $2f_c$, $3f_c$ and subharmonic $0.5f_c$, for the the bump (G1) case. Lines between experimental points are only drawn to indicate the data trend.

4

Conclusions and Recommendations

4.1. Conclusions

The following conclusions can be made to answer the research questions laid out in section 1.5

How does the boundary-layer response induced by the SERB depend on the amplitude of the incoming TS wave?

The results demonstrate that the SERB-induced response is strongly region-dependent. In the attached-flow regions upstream of and over the bump, the disturbance field remains predominantly TS-wave dominated. Increasing the forcing amplitude mainly scales the disturbance magnitude, while the instability mechanism and spectral structure remain largely unchanged. In contrast, downstream of the BFS, the forced TS disturbance interacts with the separated shear layer, leading to enhanced harmonic content, KH-type high-frequency activity, and progressive broadband spectral redistribution at higher forcing amplitudes. The SERB therefore does not act as a uniform amplifier of TS waves. Instead, it imposes a sequence of local amplification, reshaping, reduced relative growth over the bump plateau, and strong post-BFS re-amplification, with the manifestation of these mechanisms depending on the amplitude of the incoming disturbance.

4.1.1. Effect of incoming TS-wave amplitude on harmonic content

The measurements indicate that, for the clean case, the disturbance field is dominated by the forced fundamental at $f_c = 210$ Hz across all forcing amplitudes, with higher harmonics present but remaining secondary and not showing independent downstream amplification. In the bump case, the disturbance upstream of and over the SERB likewise remains predominantly narrow-band and centred on the fundamental frequency, with no clear broadband increase observed in these attached regions. In contrast, downstream of the BFS, the spectra show enhanced harmonic content together with a broader spectral distribution. The relative contribution of higher harmonics and broadband components increases with forcing amplitude in this separated-flow region. These results demonstrate that the effect of incoming TS-wave amplitude on harmonic content is weak in the attached boundary-layer regions but becomes clearly evident downstream of the BFS.

4.1.2. Wall-normal profiles at the forcing frequency

The extracted wall-normal profiles at $f_c = 210$ Hz show that, for the clean case and for the bump case upstream of the BFS, the disturbance retains a predominantly two-lobed structure consistent with a TS-wave-type response in an attached boundary layer, with greater variability over the bump surface between the FFS and BFS, as compared with the upstream stations. Downstream of the BFS, the wall-normal structure deviates from this simpler form and consistently exhibits a local minimum around $y \approx 1.2$ mm, coinciding with the expected location of the separated shear layer. In this region, the measured f_c response reflects the wall-normal structure of the disturbance within a separated/reattaching flow rather than that of an attached TS-wave eigenfunction.

4.1.3. Effect of incoming TS-wave amplitude on disturbance growth

For both the clean and bump cases, occasional local amplitude spikes that deviate from the surrounding growth trend were traced to transient variations in plasma-actuator output during specific hot-wire sweeps, rather than to changes in the boundary-layer instability mechanism. This underscores the importance of independent forcing monitoring in plasma-actuated experiments, particularly when consistent disturbance amplitude must be maintained over extended measurement campaigns.

Excluding these actuator-induced artefacts, the clean case exhibits a monotonic downstream increase in both amplitude-based and energy-based N-factor curves for the forced disturbances, while the extracted wall-normal profiles retain a TS-wave-like structure. This indicates that disturbance growth on the clean plate remains dominated by the forced fundamental mode.

For the bump case, all forcing levels exhibit the same regional behaviour: an increase in disturbance level upstream of the FFS, a reduction or flattening of growth over the raised surface, and a renewed increase downstream of the BFS. This regional pattern is consistent across both amplitude- and energy-based N-factor representations, confirming that the SERB modifies the spatial distribution of disturbance growth. The influence of forcing amplitude on the growth curves is most pronounced downstream of the BFS.

4.2. Recommendations

The present study was designed primarily to characterise the forced TS wave at $f_c = 210$ Hz and its harmonics, and to compare its evolution between the clean and bump cases. The experimental choices made were therefore appropriate for resolving the narrow-band disturbance dynamics of interest. At the same time, the results also highlight several areas in which additional measurements and further analysis would improve the interpretation of the flow physics, particularly in the separated region behind the BFS.

- **Extended time-resolved measurements in the post-BFS region:** Longer acquisition times would improve characterisation of low-frequency separated-flow dynamics (e.g. reattachment motion or shear-layer unsteadiness) and clarify the relationship between the forced narrow-band response and slower recirculation-region behaviour.
- **Planar PIV in the separated-flow region:** Planar PIV downstream of the BFS would provide direct visualisation of the separated shear layer and reattachment dynamics, enabling more direct correlation between the KH-type spectral signatures observed in the hot-wire data and the underlying flow structures.
- **Spanwise-resolved measurements:** Additional spanwise measurements would determine whether the post-BFS flow remains predominantly two-dimensional or develops significant three-dimensional structure as forcing amplitude increases.
- **Improved forcing monitoring and amplitude tracking:** Continuous or independently calibrated monitoring of plasma-actuator output would reduce uncertainty in disturbance-amplitude consistency and assist in interpreting forcing-dependent offsets in the N-factor curves. Future analyses could also compare absolute disturbance amplitudes alongside N-factors and track combined harmonic energy to clarify amplitude-dependent effects.

Bibliography

Armaly, B. F., Durst, F., Pereira, J. C. F., & Schönung, B. (1983). Experimental and theoretical investigation of backward-facing step flow. *Journal of Fluid Mechanics*, *127*, 473–496. https://doi.org/10.1017/S0022112083002839

Arnal, D., & Archambaud, J. P. (2008). Laminar-Turbulent Transition Control: NLF, LFC, HLFC.

Baines, P. G., Majumdar, S. J., & Mitsudera, H. (1996). The mechanics of the Tollmien-Schlichting wave. *Journal of Fluid Mechanics*, *312*, 107–124. https://doi.org/10.1017/S0022112096001930

Barahona, M. (2022). *Experimental Study on Tollmien-Schlichting Waves over Forward-Facing Steps* [Doctoral dissertation].

Barahona, M., Rius-Vidales, A. F., Tocci, F., Hein, S., & Kotsonis, M. (2025). The effect of a forward-facing step on Tollmien–Schlichting waves. *Journal of Fluid Mechanics*, *1023*, A38. https://doi.org/10.1017/jfm.2025.10768

Bearman, P. W. (1984). Hot-Wire Anemometry. *Journal of Fluid Mechanics*, *138*, 433–434. https://doi.org/10.1017/S0022112084210203

Benard, N., & Moreau, E. (2014). Electrical and mechanical characteristics of surface AC dielectric barrier discharge plasma actuators applied to airflow control. *Experiments in Fluids*, *55*(11), 1846. https://doi.org/10.1007/s00348-014-1846-x

Bendat, J., & Piersol, A. (2010). *Random Data: Analysis and Measurement Procedures, Fourth Edition* (1st edition). John Wiley & Sons.

Bippes, H. (1999). Basic experiments on transition in three-dimensional boundary layers dominated by crossflow instability. *Progress in Aerospace Sciences*, *35*(4), 363–412. https://doi.org/10.1016/S0376-0421(99)00002-0

Biswas, G., Breuer, M., & Durst, F. (2004). Backward-Facing Step Flows for Various Expansion Ratios at Low and Moderate Reynolds Numbers. *Journal of Fluids Engineering*, *126*(3), 362–374. https://doi.org/10.1115/1.1760532

Boiko, A. V., Dovgal, A. V., Grek, G. R., & Kozlov, V. V. (2012). *Physics of Transitional Shear Flows: Instability and Laminar–Turbulent Transition in Incompressible Near-Wall Shear Layers* (Vol. 98). Springer Netherlands. https://doi.org/10.1007/978-94-007-2498-3

Bruun, H. H. (1995). *Hot wire anemometry: Principles and signal analysis* [Section: xxiii, 507 pages : illustrations ; 25 cm.]. Oxford University Press.

Cooley, J. W., & Tukey, J. W. (1965). An Algorithm for the Machine Calculation of Complex Fourier Series. *Mathematics of Computation*, *19*(90), 297–301. https://doi.org/10.1090/S0025-5718-1965-0178586-1

Corke, T. C., Enloe, C. L., & Wilkinson, S. P. (2010). Dielectric Barrier Discharge Plasma Actuators for Flow Control. *Annual Review of Fluid Mechanics*, *42*(1), 505–529. https://doi.org/10.1146/annurev-fluid-121108-145550

Costantini, M., Risius, S., & Klein, C. (2022). Step-induced transition in compressible high Reynolds number flow. *Flow*, *2*, E33. https://doi.org/10.1017/flo.2022.21

Crouch, J. D., & Kosorygin, V. S. (2020). Surface Step Effects on Boundary-Layer Transition Dominated by Tollmien–Schlichting Instability. *AIAA Journal*, *58*(7), 2943–2950. https://doi.org/10.2514/1.J058518

Dos Santos, P., Himeno, F., Mathias, M., & Medeiros, M. (2025). Physical aspects of Tollmien–Schlichting wave acoustic receptivity due to sharp-edged rectangular bumps and gaps investigated via subsonic high-fidelity simulations. *Journal of Fluid Mechanics*, *1009*, A59. https://doi.org/10.1017/jfm.2025.206

Duchmann, A., Reeh, A., Quadros, R., Kriegseis, J., & Tropea, C. (2010). Linear Stability Analysis for Manipulated Boundary-Layer Flows using Plasma Actuators [Series Title: IUTAM Bookseries]. In *Seventh IUTAM Symposium on Laminar-Turbulent Transition* (pp. 153–158, Vol. 18). Springer Netherlands. https://doi.org/10.1007/978-90-481-3723-7_23

Edelmann, C. (2014). Influence of Forward-Facing Steps on Laminar-Turbulent Transition.

Ehrenstein, U., & Gallaire, F. (2009). Global Low-Frequency Oscillations in a Separating Boundary-Layer Flow [Series Title: IUTAM Bookseries]. In G. Gladwell, R. Moreau, M. Braza, & K. Hourigan (Eds.), *IUTAM Symposium on Unsteady Separated Flows and their Control* (pp. 123–133, Vol. 14). Springer Netherlands. https://doi.org/10.1007/978-1-4020-9898-7_10

Forte, M., Jolibois, J., Pons, J., Moreau, E., Touchard, G., & Cazalens, M. (2007). Optimization of a dielectric barrier discharge actuator by stationary and non-stationary measurements of the induced flow velocity: Application to airflow control. *Experiments in Fluids*, *43*(6), 917–928. https://doi.org/10.1007/s00348-007-0362-7

Franco Sumariva, J. A., Hein, S., & Valero, E. (2020). On the influence of two-dimensional hump roughness on laminar–turbulent transition. *Physics of Fluids*, *32*(3), 034102. https://doi.org/10.1063/1.5131577

Gallaire, F., Marquillie, M., & Ehrenstein, U. (2007). Three-dimensional transverse instabilities in detached boundary layers. *Journal of Fluid Mechanics*, *571*, 221–233. https://doi.org/10.1017/S0022112006002898

Gao, B., Park, D. H., & Park, S. O. (2011). Stability analysis of a boundary layer over a hump using parabolized stability equations. *Fluid Dynamics Research*, *43*(5), 055503. https://doi.org/10.1088/0169-5983/43/5/055503

Garcia Villasol, S. (2025). *Experimental Design and Implementation of a DRL-based Tollmien-Schlichting Wave Controller* [Doctoral dissertation, Universidad Carlos III de Madrid].

Gössling, S. (2020). Risks, resilience, air transport 2020 RG. *Journal of Air Transport Management*, *89*. https://doi.org/10.1016/j.jairtraman.2020.101933

Hansen, H. (2010). LAMINAR FLOW TECHNOLOGY – THE AIRBUS VIEW.

Hasan, M. A. Z. (1992). The flow over a backward-facing step under controlled perturbation: Laminar separation. *Journal of Fluid Mechanics*, *238*, 73–96. https://doi.org/10.1017/S0022112092001642

Hildebrand, N., Choudhari, M. M., & Paredes, P. (2020). Predicting Boundary-Layer Transition over Backward-Facing Steps via Linear Stability Analysis. *AIAA Journal*, *58*(9), 3728–3734. https://doi.org/10.2514/1.J059713

Hildebrand, N., Mysore, P. V., Choudhari, M. M., Venkatachari, B. S., & Paredes, P. (2022). Transition Prediction of Boundary Layers in the Presence of Backward-Facing Steps. *AIAA Journal*, *60*(7), 4149–4161. https://doi.org/10.2514/1.J061296

Hildebrand, N., Paredes, P., & Choudhari, M. M. (2025). Effect of a forward-facing step on the disturbance amplification in a flat-plate boundary layer. *Physical Review Fluids*, *10*(4), 043901. https://doi.org/10.1103/PhysRevFluids.10.043901

Joslin, R. D. (2025). AIRCRAFT LAMINAR FLOW CONTROL.

Kotsonis, M. (2015). Diagnostics for characterisation of plasma actuators. *Measurement Science and Technology*, *26*(9), 092001. https://doi.org/10.1088/0957-0233/26/9/092001

Kotsonis, M., Shukla, R. K., & Pröbsting, S. (2015). Control of Natural Tollmien-Schlichting Waves using Dielectric Barrier Discharge Plasma Actuators. *International Journal of Flow Control*, *7*(1-2), 37–54. https://doi.org/10.1260/1756-8250.7.1-2.37

Kotsonis, M., Veldhuis, L., & Bijl, H. (2010). Plasma Assisted Aerodynamics for Transition Delay [Series Title: IUTAM Bookseries]. In *Seventh IUTAM Symposium on Laminar-Turbulent Transition* (pp. 219–224, Vol. 18). Springer Netherlands. https://doi.org/10.1007/978-90-481-3723-7_34

Krein, A., & Williams, G. (2012). *Flightpath 2050 :Europe's vision for aviation : Maintaining global leadership and serving society's needs.* IOS Press. Retrieved November 15, 2025, from https://data.europa.eu/doi/10.2777/50266

Kriegseis, J., Grundmann, S., & Tropea, C. (2011). Power consumption, discharge capacitance and light emission as measures for thrust production of dielectric barrier discharge plasma actuators. *Journal of Applied Physics*, *110*(1), 013305. https://doi.org/10.1063/1.3603030

Kriegseis, J., Simon, B., & Grundmann, S. (2016). Towards In-Flight Applications? A Review on Dielectric Barrier Discharge-Based Boundary-Layer Control. *Applied Mechanics Reviews*, *68*(2), 020802. https://doi.org/10.1115/1.4033570

Lin, N., Reed, H. L., & Saric, W. S. (1992). Effect of leading-edge geometry on boundary-layer receptivity to freestream sound. In *Instability, Transition, and Turbulence* (pp. 421–440). Springer.

Mack, L. M. (1984). Boundary-Layer Linear Stability Theory.

Marquillie, M., & Ehrenstein, U. (2003). On the onset of nonlinear oscillations in a separating boundary-layer flow. *Journal of Fluid Mechanics*, *490*, 169–188. https://doi.org/10.1017/S0022112003005287

Merino-Martínez, R., Rubio Carpio, A., Lima Pereira, L. T., Van Herk, S., Avallone, F., Ragni, D., & Kotsonis, M. (2020). Aeroacoustic design and characterization of the 3D-printed, open-jet, anechoic wind tunnel of Delft University of Technology. *Applied Acoustics*, *170*, 107504. https://doi.org/10.1016/j.apacoust.2020.107504

Morais, L. (2023). Influence of a hump on crossflow instabilities and transition.

Moreau, E. (2007). Airflow control by non-thermal plasma actuators. *Journal of Physics D: Applied Physics*, *40*(3), 605–636. https://doi.org/10.1088/0022-3727/40/3/S01

Oppenheim, A. V., & Schafer, R. W. (2014). *Discrete-time signal processing* (Third edition, Pearson New international edition). Pearson.

Park, D., & Park, S. O. (2013). Linear and non-linear stability analysis of incompressible boundary layer over a two-dimensional hump. *Computers & Fluids*, *73*, 80–96. https://doi.org/10.1016/j.compfluid.2012.12.007

Perraud, J., & Séraudie, A. (2000). EFFECTS OF STEPS AND GAPS ON 2D AND 3D TRANSITION. *European Congress on Computational Methods in Applied Sciences and Engineering*.

Perraud, J., Arnal, D., & Kuehn, W. (2014). Laminar-turbulent transition prediction in the presence of surface imperfections. *Int. J. of Engineering Systems Modelling and Simulation*, *6*, 162–170. https://doi.org/10.1504/IJESMS.2014.063129

Perraud, J., D, A., A, S., & D, T. (2004, October). *Laminar-turbulent transition on aerodynamic surfaces with imperfections*. https://doi.org/10.13140/RG.2.1.3532.1364

Placidi, M., Gaster, M., & Atkin, C. J. (2020). Acoustic excitation of Tollmien–Schlichting waves due to localised surface roughness. *Journal of Fluid Mechanics*, *895*, R5. https://doi.org/10.1017/jfm.2020.349

Reshotko, E. (2008). Transition Issues for Atmospheric Entry. *Journal of Spacecraft and Rockets*, *45*(2), 161–164. https://doi.org/10.2514/1.29777

Risius, S., & Costantini, M. (2025). Influence of backward-facing steps on laminar-turbulent transition in two-dimensional boundary layers at subsonic Mach numbers. *Experiments in Fluids*, *66*(5), 88. https://doi.org/10.1007/s00348-025-03994-2

Rius-Vidales, A. F., Morais, L., Westerbeek, S., Casacuberta, J., Soyler, M., & Kotsonis, M. (2025). Delay of swept-wing transition using a surface hump. *Journal of Fluid Mechanics*.

Schlichting, H. (1950). Amplitude distribution and energy balance of small disturbances in plate flow. *National Advisory Committee for Aeronautics*, *1265*.

Schlichting, H., & Gersten, K. (2017). *Boundary-Layer Theory*. Springer Berlin Heidelberg. https://doi.org/10.1007/978-3-662-52919-5

Schrauf, G. (2005). Status and perspectives of laminar flow. *The Aeronautical Journal*, *109*(1102), 639–644. https://doi.org/10.1017/S000192400000097X

Schubauer, G., & Skramstad, H. (1947). Laminar boundary-layer oscillations and transition on a flat plate. *Journal of Research of the National Bureau of Standards*, *38*(2), 251. https://doi.org/10.6028/jres.038.013

Schultz, M. P., & Flack, K. A. (2007). The rough-wall turbulent boundary layer from the hydraulically smooth to the fully rough regime. *Journal of Fluid Mechanics*, *580*, 381–405. https://doi.org/10.1017/S0022112007005502

Teng, M. (2023). Effects of surface imperfections on the transitional boundary layer. *Physics of Fluids*, *35*(8), 084119. https://doi.org/10.1063/5.0163366

Teng, M., & Piomelli, U. (2022). Instability and Transition of a Boundary Layer over a Backward-Facing Step. *Fluids*, *7*(1), 35. https://doi.org/10.3390/fluids7010035

Tollmien, W. (1929). Über die Entstehung der Turbulenz. *Nachrichten von der Gesellschaft der Wissenschaften zu Göttingen, Mathematisch-Physikalische Klasse*.

Tropea, C., Yarin, A. L., & Foss, J. F. (2007). *Springer handbook of experimental fluid mechanics*. Springer.

Van Ingen, J. (2008). The eN Method for Transition Prediction. Historical Review of Work at TU Delft. *38th Fluid Dynamics Conference and Exhibit*. https://doi.org/10.2514/6.2008-3830

Wang, Y. X., & Gaster, M. (2005). Effect of surface steps on boundary layer transition. *Experiments in Fluids*, *39*(4), 679–686. https://doi.org/10.1007/s00348-005-1011-7

Welch, P. (1967). The use of fast Fourier transform for the estimation of power spectra: A method based on time averaging over short, modified periodograms. *IEEE Transactions on Audio and Electroacoustics*, *15*(2), 70–73. https://doi.org/10.1109/TAU.1967.1161901

Westerbeek, S., Franco Sumariva, J. A., Michelis, T., Hein, S., & Kotsonis, M. (2023). Linear and Nonlinear Stability Analysis of a Three-Dimensional Boundary Layer over a Hump. *AIAA SCITECH 2023 Forum*. https://doi.org/10.2514/6.2023-0678

White, E. B., & Ergin, F. G. (2004). Using laminar-flow velocity profiles to locate the wall behind roughness elements. *Experiments in Fluids*, *36*(5), 805–812. https://doi.org/10.1007/s00348-003-0766-y

White, F. M., & Majdalani, J. (2022). *Viscous fluid flow* (Fourth edition. International student edition) [OCLC: 1231955676]. McGraw-Hill.

Wong, P. W. C., Maina, M., & Lawson, S. (2021). HYBRID LAMINAR FLOW CONTROL (HLFC) RESEARCH AT AIRCRAFT RESEARCH ASSOCIATION (ARA), PAST, PRESENT AND FUTURE. https://www.icas.org/icas_archive/ICAS2020/data/papers/ICAS2020_0236_paper.pdf

Worner, A., Rist, U., & Wagner, S. (2003). Humps/Steps Influence on Stability Characteristics of Two-Dimensional Laminar Boundary Layer. *AIAA Journal*, *41*(2), 192–197. https://doi.org/10.2514/2.1960

A

Additional Figures

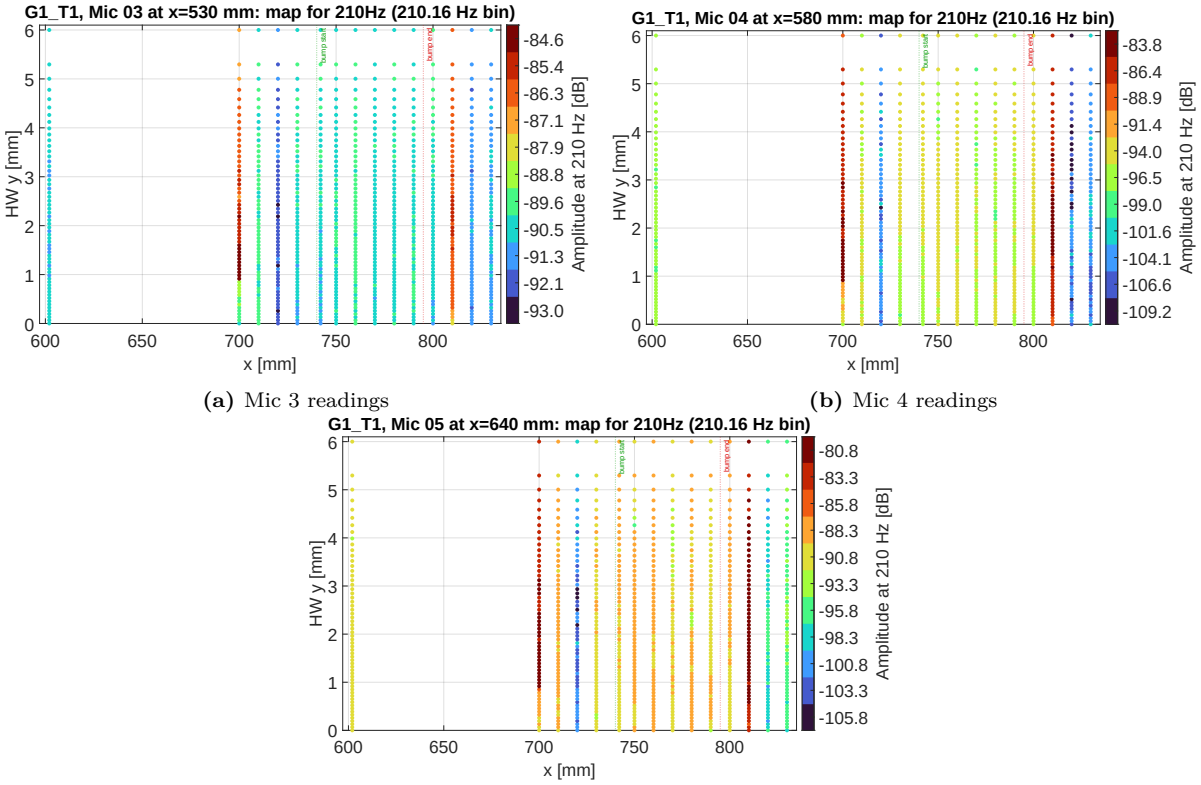

(a) Mic 3 readings

(b) Mic 4 readings

(c) Mic 5 readings

Figure A.1: Peak amplitude maps recorded by the surface microphones at the triggered frequency ($f_c = 210$ Hz) corresponding to each measurement location in the HW sweep for the bump case (G1) with low forcing (T1)

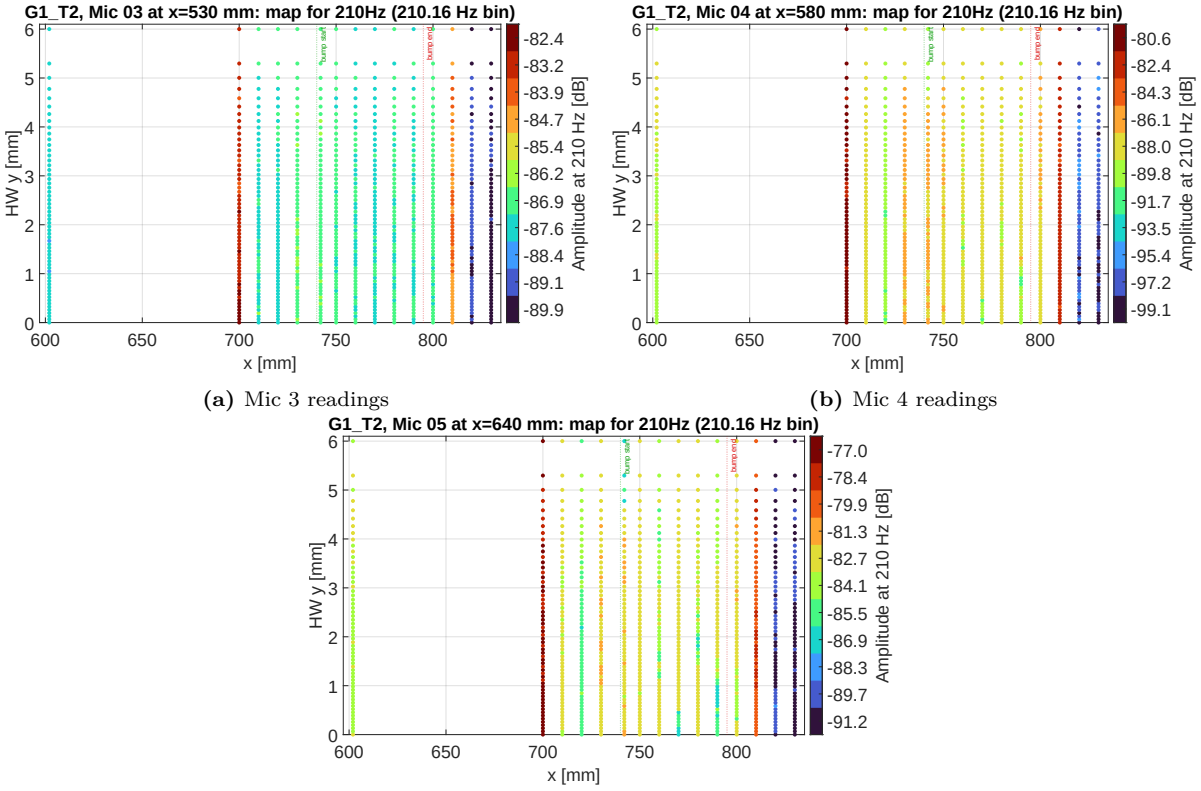

(a) Mic 3 readings

(b) Mic 4 readings

(c) Mic 5 readings

Figure A.2: Peak amplitude maps recorded by the surface microphones at the triggered frequency ($f_c = 210$ Hz) corresponding to each measurement location in the HW sweep for the bump case (G1) with medium forcing (T2).

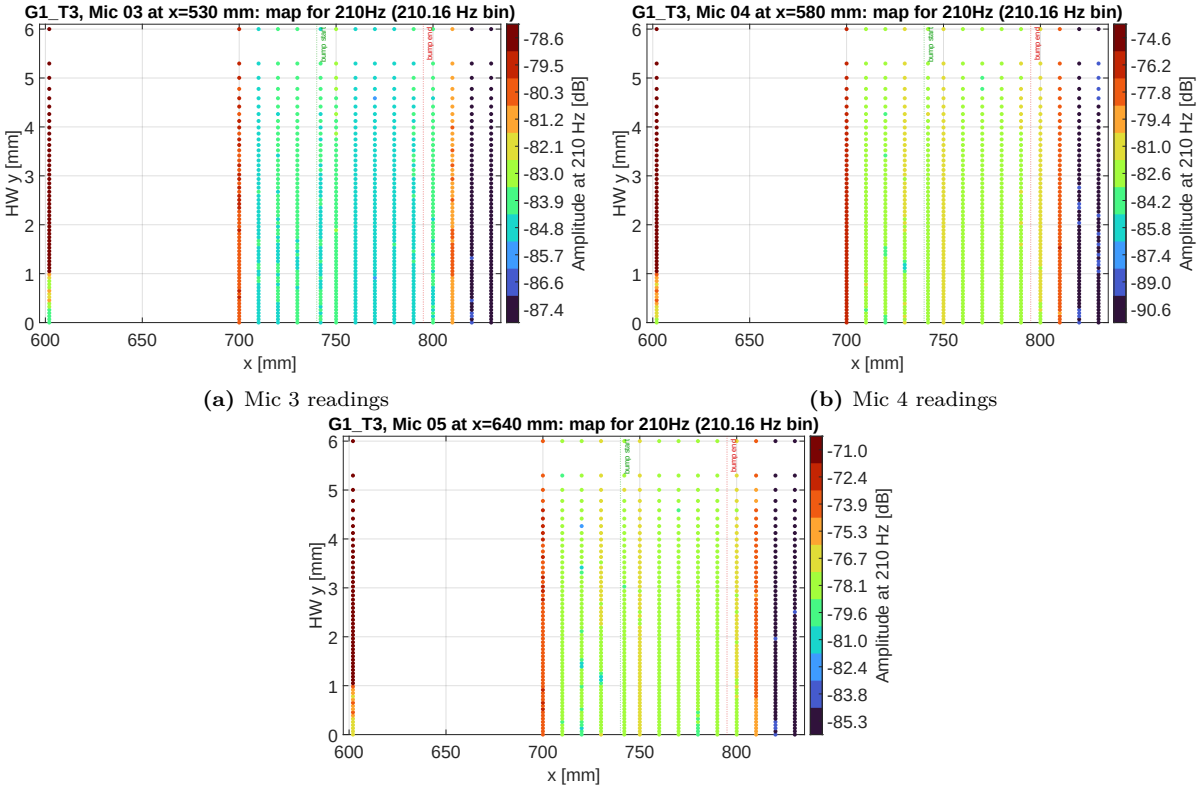

(a) Mic 3 readings

(b) Mic 4 readings

(c) Mic 5 readings

Figure A.3: Peak amplitude maps recorded by the surface microphones at the triggered frequency ($f_c = 210$ Hz) corresponding to each measurement location in the HW sweep for the bump case (G1) with the highest forcing (T3).